**Title**
High Pressure Behavior of Nanomaterials



**Author**
Lutker, Katie M.

**Publication Date**
2013

Peer reviewed|Thesis/dissertation

# High Pressure Behavior of Nanomaterials

by

Katie M. Lutker

A dissertation submitted in partial satisfaction of the

requirements for the degree of

Doctor of Philosophy

in

Chemistry

in the

Graduate Division

of the

University of California, Berkeley

Committee in charge:

Professor A. Paul Alivisatos, Chair
Professor Peidong Yang
Professor Peter Yu

Fall 2013

# High Pressure Behavior of Nanomaterials



by

Katie M. Lutker

# Abstract

## High Pressure Behavior of Nanomaterials

by

Katie M. Lutker

Doctor of Philosophy in Chemistry

University of California, Berkeley

Professor A. Paul Alivisatos, Chair

The investigation of the properties of matter under high pressure is becoming increasing important to many scientific fields, including chemistry, physics, and biology. From a fundamental standpoint, the application of high pressure allows one to investigate the effect of volume on the properties of a material. It also allows for the examination of the conversion of one phase of matter to another, whether through the crystallization of a material under high pressure, or the transformation of a solid from one crystal structure to another. This dissertation explores the properties of nanoscale materials under high pressure.

The size dependence for solid-solid phase transitions in II-VI nanocrystals under high pressure has been previously investigated. Nanoparticles represent an important size regime where the surface atoms make up a significant percentage of the total atoms in the crystal. This leads to the surface playing a larger role in the thermodynamics of the phase transition in these nanocrystals.

The first part of this dissertation examines the effect of small changes in the structure of the nanomaterial on its high pressure behavior. By changing the surface of cadmium selenide nanocrystals through the introduction of a zinc sulfide shell, it was determined that the phase transition could be tuned for shell thicknesses below the critical thickness. In addition to structural phase transitions in this core/shell system, the optical properties under high pressure were also investigated. The fluorescence of the core/shell particles splits into multiple peaks due to a breaking of the crystal symmetry and spin exchange in the excitons under pressure.

This theme was continued through the investigation of bismuth selenide nanoribbons with and without copper intercalated into the lattice. Bismuth selenide has been found to be a topological insulator, while copper bismuth selenide is a superconductor. The phase transition from the layered rhombohedral structure to the monoclinic phase in bismuth selenide nanomaterials could be pushed to higher pressures through the intercalation of copper in the van der Waals gap between the crystal layers.

The dissertation continues by exploring the mechanism of the wurtzite to rocksalt phase transition in cadmium sulfide nanocrystals on ultrafast timescales. A shock wave was initiated through the sample using a laser and the phase transition was probed using an ultrafast X-ray probe pulse. This allowed for the collection of the necessary structural data from the diffraction patterns at different time delays. A *h*-MgO type intermediate was found to be present under lower shock stresses, but it was not observed at higher shock stresses. This indicates that multiple phase transition pathways are simultaneously occurring in the sample.

Steps towards achieving the ability to image the fluorescence of single semiconductor nanoparticles under high pressure are discussed. At a single particle level new phenomena have been observed due to the inherent heterogeneity of the sample and a lack of averaging over multiple events. There are many hurdles that must be overcome before such experiments can be achieved.

The last part of the dissertation discusses the use of the high pressure behavior of these semiconductor nanocrystals to sense forces in a biological sample. The spectral shift of tetrapod nanocrystals was used to quantify the force exerted on a substrate by beating HL-1 cardiomyocytes. This was performed through the use of an acousto-optic tunable filter to provide the measurements with spectral, temporal, and spatial resolution.

Through the investigation of the fundamental properties of nanomaterials under high pressure, a better understanding of these materials, including their thermodynamics, was obtained. As a result, new applications of these materials to fields such as force sensing are discussed and implemented.

*To my parents and my husband.*

# Table of Contents

# List of Figures

**Chapter 6**



**Chapter 7**



**Chapter 8**



**Appendix A**

**Appendix B**

# List of Tables

# Acknowledgements

I am grateful to a great number of people here at Berkeley and beyond for their support throughout my time at UC Berkeley. I have been extremely blessed to have been surrounded and supported by such a wonderful group of people.

First, I must thank my adviser, Professor Paul Alivisatos, for not only allowing me to be a part of his research group, but teaching me the importance of making connections between different scientific ideas and to always look deeper at my data. He also gave me the freedom to make my own mistakes and to learn from them. The knowledge and skills I have learned under his mentorship will stay with me as I embark on my next endeavor.

I would like to thank Kristie Koski and Noelle Kamp, both senior members of the Alivisatos group, for teaching me everything they knew about diamond anvil cells before they graduated. Charina Choi taught me how to do nanoparticle synthesis. Both Kristie and Charina were also great collaborators on the projects we performed together.

The other members of the Alivisatos group, both past and present, also deserve my gratitude. I have always been able to rely on Andrew Olson for great feedback and help with my projects. I must also thank the two undergraduate students with whom I have worked with for several years now: Phuong Tran and Allison Wustrow. They have been instrumental in helping me perform my research and doing the projects that I did not have time to do myself. I also would like to thank Mark Polking, Jennifer Dionne, Trevor Ewers, Sassan Sheikholeslami, Young-wook Jun, Alexandra Courtis, Jessica Smith, Brandon Beberwyck, Karthish Manthiram, Max Merkle, David Grauer, Kemi Oba, Tina Ding, Vivian Ferry, and Somin Lee for their help through the years and for many laughs and great times.

I would also like to thank my many collaborators. At the ALS I worked with Bin Chen, Jason Knight, and Simon Clark at beamline 12.2.2. In addition, Joshua Wittenberg (a former Alivisatos group member) and the entire Lindenberg group at Stanford, with whom I worked with at the XPP beamline at the LCLS. I am also grateful to several extremely gifted theorists, Michael Grünwald, Eran Rabani, and Phillip Geissler, for performing the simulation on core/shell nanoparticles under high pressure.

Rita Tidwell and Karen Sharp must be thanked for making sure that the lab always had what it needed, when it was needed. James Wang was essential in keeping the lab running smoothly and fixing anything and everything in the lab.

I must also thank my undergraduate advisor, Professor Adam Matzger at the University of Michigan, for putting me on this path. Without his encouragement and advice, I would not have considered graduate school as a path that was open to me.

I am also grateful to my family without whom this journey would not have been possible. I know you do not understand the majority of what I say, but thank you for always listening and being there (even with the 3 hour time difference). A special thanks to my Dad for his advice in designing the various parts that I wanted to make and making sure that I used the correct terminology when it came to hardware and tools.

Last, but certainly not least, I would like to thank my husband, Joe. He has stayed with me through thick and thin, even while I was studying for my qualifying exam. Since he also worked on the D-level, he was always right down the hall when I needed him (or needed to borrow something from the Graves group). I am extremely blessed to have him in my life.

# Chapter 1
# Introduction

## 1.1 Introduction

When considering phase transitions, scientists are used to looking at the phase diagram in terms of pressure and temperature. There is a size dependence for phase transitions, but rarely is size considered when looking at phase transitions. The size of matter varies over many orders of magnitude from individual atoms at angstrom length scales to the bulk matter that is observed on a daily basis (micrometers to kilometers in size) (Figure 1.1). Nanocrystals, being only nanometers in size, consist of hundreds to thousands of atoms.[1] The properties of nanocrystals differ greatly from a bulk crystal of the same material. This size regime is unique in that it can no longer be assumed that the surface of the material does not impact in thermodynamic calculations, as it is for bulk matter. The number of surface atoms now makes up a significant quantity of the total atoms in a single nanocrystal. Thus the surface term must be included in any thermodynamic calculation.

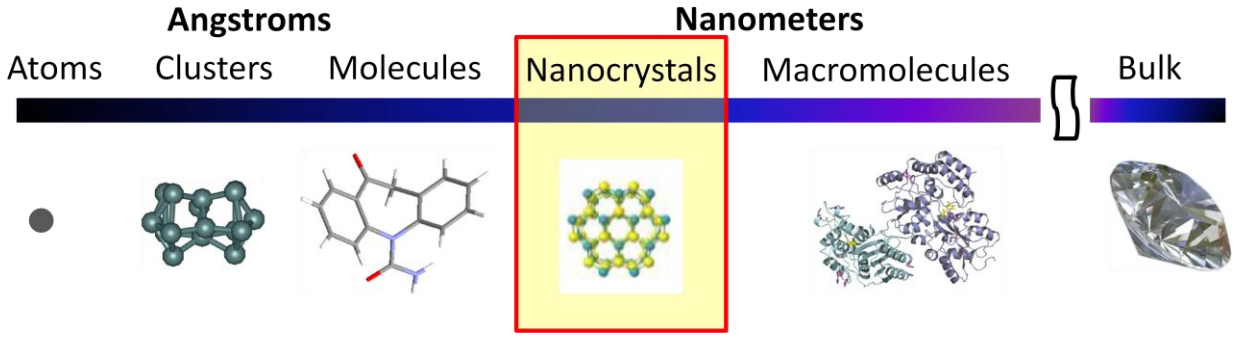


**Figure 1.1:** Size regimes of matter from single atoms to bulk matter.

There has been an abundance of experiments performed with the goal of understanding various aspects of semiconductor nanocrystals and their applications.[1-5] Fundamentally, the investigation of phase transitions at the nanoscale has provided several important insights. Semiconductor nanocrystals have been shown to exhibit different behavior upon undergoing a

phase transition when compared to the bulk material. The presence of a thermodynamically significant surface in the material has a drastic effect on the conditions under which a phase transition occurs, as evidenced by the fact that the melting point of small nanocrystals can be less than 50% of that of the bulk material.[11] For high pressure structural phase transitions in II-VI semiconductors it has been found that, unlike bulk single crystals, nanocrystals convert from one crystal structure to the next without fracturing into multiple domains.[7] This is useful when examining the mechanism and driving forces involved in these phase transitions. In addition to a change in the thermodynamic phase transition pressure, previous investigations of high pressure structural phase transitions in nanocrystals have also shown that the transition seems to be under kinetic control.[7] It has been proposed that as the size of the system gets smaller, it reaches a point where a true solid-solid phase transition ceases to occur and should be considered more along the lines of a molecular isomerization.[6-7]

## 1.2 Nanoparticles

The properties of nanocrystals are highly dependent on size. At small sizes, the number of surface atoms becomes a high percentage of the total number of atoms in the crystallite. This means that the surface begins to play a significant role in the properties of the material.[6-7,11] In addition, quantum size effects dominate the electronic and optical properties of the nanocrystals.[1,3] For semiconductors, the combination of these effects yields the ability to tune the optical and electronic properties of the system by solely changing the size of the nanocrystal.[1,3]

In thermodynamic calculations, the surface is typically ignored for simplicity. In bulk materials, the contribution of the surface is negligible, but it cannot be ignored for nanoparticles. The surface atoms of a nanoparticle make up a significant number of the total number of atoms in the system. In thermodynamics, the surface comes into play through the surface area and surface tension terms. This can be expressed by rewriting the energy equation as:

$$U=TS-PV+\mu N-\gamma A \tag{1.1}$$

where U is the energy, T is the temperature, S is the entropy, P is the pressure, V is the volume, μ is the chemical potential, N is the number of atoms or molecules, γ is the surface tension, and A is the surface area of the system. The surface term can manifest itself in the form of size dependent melting points and phase transitions.[6,7,9,11]

In semiconductors, the band structure of the material is greatly affected by quantum size effects.[1] As a particle gets smaller, the density of states transitions from the continuous limit for bulk (3-dimensional) matter to quantized levels for systems that are completely confined (0-dimensional) matter (Figure 1.2).[1,2] This leads to the ability to tune the optical and electrical properties by using the particle size as the variable instead of the material. More simply put, as the size of the quantum mechanical box changes, the energy levels available change, as approximately defined by:

$$E_n = \frac{\hbar^2 \pi^2 n^2}{2mL^2}, \tag{1.2}$$

where ħ is the reduced Planck's constant, n is the energy level, m is the mass, and L is the length of the box or, in this case, the size of the particle. These effects can be experimentally observed through a change in the band gap of a material as the particle size decreases below the Bohr exciton radius (Figure 1.3).[1]

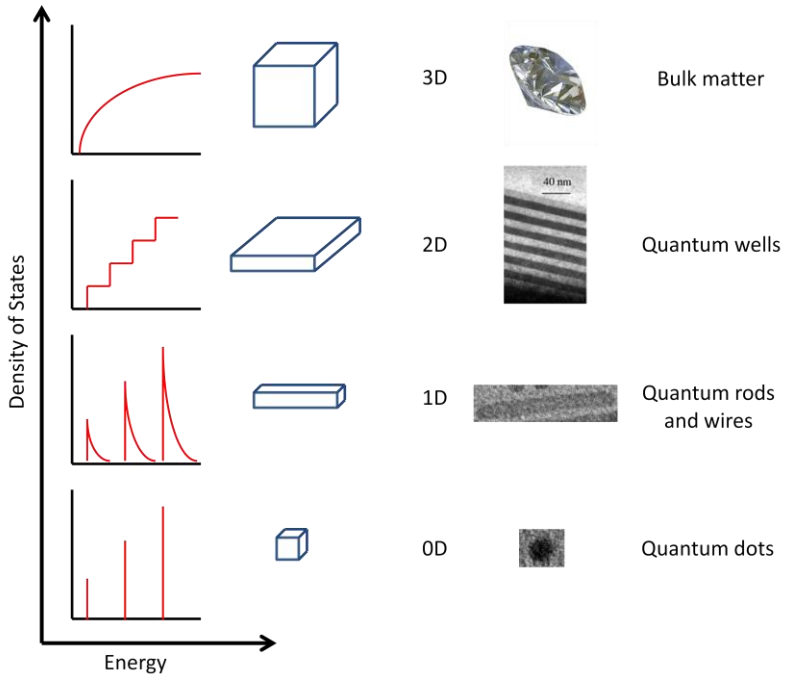


**Figure 1.2:** Density of states as theoretically defined for various sizes and geometries of matter. Figure adapted from Reference 1. The image of a quantum well is from Reference 12.

**Figure 1.3:** Photograph of the fluorescence from cadmium selenide nanocrystals of different sizes. Particles shown here were synthesized by Jennifer Dionne and the author.

Despite nanoparticles having discrete bands, it is still useful to think of their properties in terms of band theory. This is extremely convenient for interpreting the optical spectra of nanoparticles. For instance, it is well known that the wurtzite and zinc blende phases of cadmium selenide nanoparticles exhibit an excitonic feature in their absorption spectra and strong fluorescence.[13-14] In contrast, cadmium selenide nanoparticles in the rocksalt crystal structure have a featureless absorption spectrum and do not fluoresce.[13-14] For bulk cadmium selenide, the 4-coordinate phases are direct gap semiconductors, while the rocksalt phase is an indirect gap semiconductor (Figure 1.4).[15-17] In a direct gap semiconductor, fluorescence is an allowed, k=0 process. The indirect band gap semiconductor requires a change in the wavevector, k, for fluorescence to occur. This requires both a phonon and a photon. Fluorescence in an indirect gap semiconductor is considered a forbidden process. This same behavior is observed for cadmium selenide nanoparticles in the wurtzite, zinc blende, and rocksalt phases.

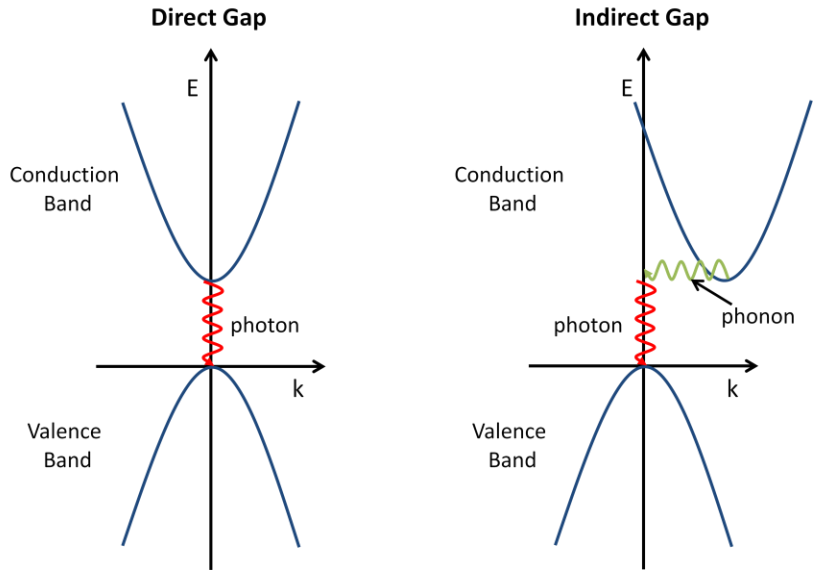


**Figure 1.4:** Schematic of the band structure of direct and indirect gap semiconductors.

Because of the optical tunability of their optical properties and their bright fluorescence, nanoparticles have been sought out for many applications. Common uses include biological labelling,[4] solar cells,[5] and light emitting diodes.[18] Recently, the ability to create nanoparticle heterostructures with controllable geometries has opened to door to exciting new opportunities.[19-25]

## 1.3 High Pressure Behavior of Nanoparticles

The behavior of materials under high pressure has been increasingly studied since the advent of the diamond anvil cell in the middle of the 20$^{th}$ century.[26-27] Placing a material in a high pressure environment is the easiest way to examine the effects of the volume on the thermodynamics of the system. The elastic and plastic properties of various materials have been

investigated in addition to the structural and magnetic phase transitions that occur under high pressure. Absorption, fluorescence, Raman spectroscopy and X-ray diffraction have been popular techniques for the characterization of various materials under high pressure.[28-29] Recent advances have also allowed for high pressure experiment to be performed with under high temperature conditions.[30] For bulk semiconductors especially, the phase transitions under high pressure have been characterized both optically and structurally.[15-17,31]

As previously mentioned, the surface atoms make up a significant number of the total atoms in the crystal for nanoparticles. Thermodynamically, this is accounted for by added the surface term to the free energy equation (Equation 1.1). The inclusion of this term makes the phase transition conditions of a system size dependent. The consequences of this will be discussed in Section 1.3.1 for cadmium selenide nanocrystals

The band structure of a semiconductor also changes under pressure, not only due to the phase transitions, but also due to the change in the volume of the unit cell of the material. This behavior is fairly well understood and will be discussed briefly in Section 1.3.2.

### *1.3.1 Thermodynamics and Kinetic Effects*

The solid-solid phase transition in cadmium selenide (CdSe) nanocrystals has been previously investigated in detail.[6-8,13-14,32-34] This makes it an excellent case study for the behavior of nanoparticles under high pressure. During this transition, cadmium selenide goes from a 4-coordinate tetrahedrally coordinated wurtzite crystal structure to the 6-coordinate octahedrally coordinated rocksalt structure, with the application of pressure (Figure 1.5). For CdSe nanocrystals the phase transition occurs at significantly higher pressures than in the bulk. For instance, a particle with a 1 nm radius undergoes the wurtzite to rocksalt transformation at 4.9 GPa, whereas a particle with a radius of 2.1 nm has a transition at 3.6 GPa.[6] In comparison, the transition for bulk CdSe occurs between approximately 2.0-3.0 GPa.[15-17] These phase transition pressures were determined by averaging the upstroke and the downstroke pressures. This process assumes a symmetric contribution of the under- and over-pressing to the driving force, which, although a reasonable estimate, is not accurate for this phase transition.[33] It does, however, provide a reasonable estimate of the thermodynamic values.

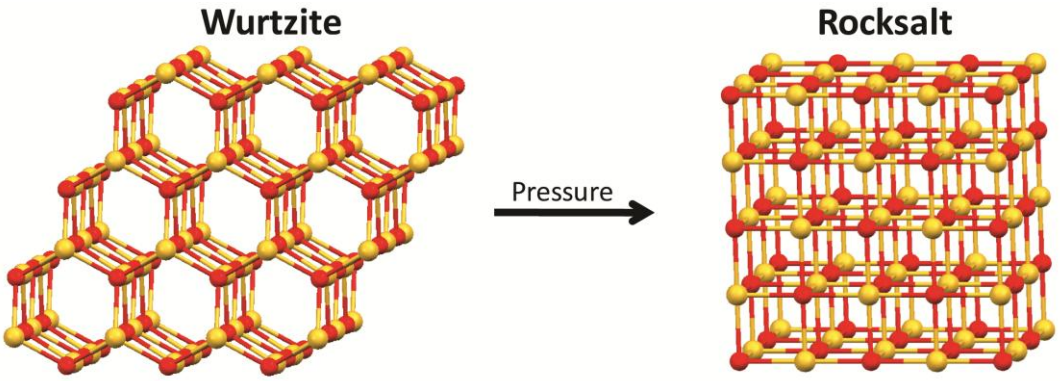


**Figure 1.5:** Crystal structures of wurtzite and rocksalt.

By using the relationship in Equation 1.1, the conditions for a phase transition in a nanocrystal system can be found. This is found by first establishing that $\mu_{wz}=\mu_{RS}$ at the phase transition pressure.[7] Then the thermodynamic equation defining the phase transition becomes:

$$P_T(V_{WZ} - V_{RS}) + U_{WZ}(P_T) - U_{RS}(P_T) = \gamma_{Rs}A_{RS} - \gamma_{WZ}A_{Wz}, \quad (1.3)$$

where $P_T$ is the phase transition pressure.[7] The size dependence of the thermodynamic phase transition pressures is attributed to the surface term of Equation 1.1.[7] One must be careful about how to define the surface tension term, $\gamma$. There is evidence that the surface tension for a system such as cadmium selenide nanocrystals can be modeled as:

$$\gamma = c_1 + \frac{c_2}{r(\text{Å})^2}, \quad (1.4)$$

where $c_1$ is the bulk surface energy of a low index surface, $c_2$ is the change in the surface energy due to curvature of the particle, and r is the radius in Angstroms of the particles.[4,7]

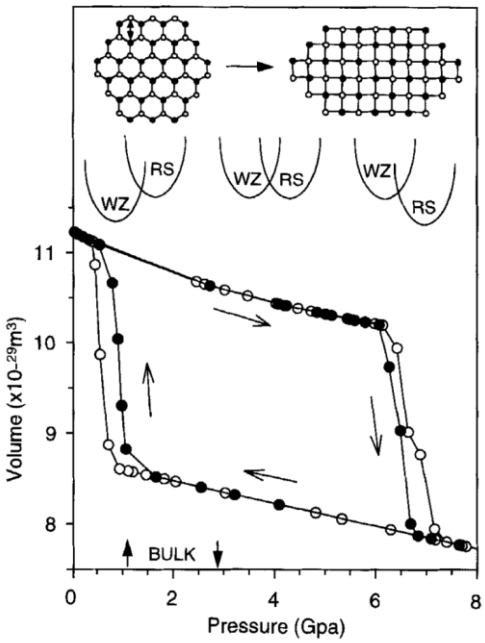


**Figure 1.6:** Hysteresis curve for two sizes of CdSe nanocrystals. The corresponding energy barriers for the different regions of the hysteresis are shown above the curve. (Figure from Reference 35).

The nanocrystalline CdSe solid-solid phase transition also has a hysteresis that is approximately three times that of the bulk transition (Figure 1.6).[35] The hysteresis curve is constructed by plotting the volume of the unit cell versus the pressure. It is thought that this increased hysteresis width is due to the lack of defects present in nanocrystals.[7] The energy to create and support a defect inside such a small volume is significant, and in many systems the defect is self purified out of the crystal during growth.[36] Solid-solid phase transitions usually

nucleate at defects in the lattice,[37] but without the defects the barrier to nucleation of the rock-salt phase is greater, leading to the need to overpressure the system to induce a phase transition in nanocrystals.[35] The interfacial energy between the rocksalt nucleus and the surrounding structure must be surpassed in order for the new phase to propagate.[7,35] This energy barrier in part defines the width of the hysteresis curve.

It should also be noted that upon return to the low pressure phase, CdSe does not form phase-pure wurtzite crystals. Instead, stacking faults are introduced, making the crystals a mixture of the wurtzite and zinc blende phases. Thermodynamically speaking, this is not unexpected as the energy difference between the two structures is small.[6]

### *1.3.2 Pressure Effects on the Band Structure*

As pressure is exerted on a system, the atoms in that material get closer together, shrinking the volume. As the distance between the atoms decreases, the overlap between atomic orbitals increases. Simple molecular orbital theory tells us that when there is a better overlap between the atomic orbitals, the resultant molecular orbitals split to a greater extent. The band gap of a material can be shifted a significant amount solely by the application of pressure. In addition, the bands usually broaden under high pressure. The change in the band gap of a material under pressure can be equivalent to completely changing the material or alloying.[38] Under hydrostatic pressure, this corresponds to a blue shift of the absorption and fluorescence. Under non-hydrostatic (uniaxial) pressure the shift is not as straight forward. Uniaxial pressure breaks the symmetry of the crystal. This can result in splitting of the bands relative to the original symmetry.[38] The effect of hydrostatic pressure on many semiconductors has been well characterized, but the effects non-hydrostatic pressure have proven more difficult to reproducibly characterize for a variety of factors.[38]

## 1.4 Motivation

While the high pressure behavior of simple systems such as CdSe nanocrystals has been thoroughly studied and is generally well understood, little has been done to investigate more complicated systems. For instance, the effect of an epitaxial shell grown onto a nanocrystal is not known. The lattice mismatch at the interface of the two materials could exert a pressure on the core, changing the pressure at which the phase transition occurs. Disrupting a layered structure could also change the pressure of a phase transition in these materials. It is unknown how small changes to the material such as these affect the behavior of the material under high pressure. From the study of these materials information about the behavior of complex materials under high pressure and the mechanism of the phase transition can be elucidated. In addition, the more detailed dynamics of the phase transition on a single nanoparticle level are not known and can provide additional insight into the mechanism of the phase transition.

## 1.5 Dissertation Outline

The objective of this work was to determine how small changes in structure can tune the properties of nanomaterials under high pressure. These studies were performed in a hydrostatic or quasi-hydrostatic environment inside a diamond anvil cell. Effort was taken in trying to elucidate trends induced by changing the structures of materials in a controlled manner. In addition, steps towards exposing the mechanism of the wurtzite to rock salt structural phase transitions were taken through the use of ultrafast pump probe techniques. Chapter 2 of this dissertation discusses the experimental techniques used to generate high pressure, including diamond anvil cells and shock waves. In addition, a brief introduction to the colloidal synthesis of nanoparticles is given. The effect of a zinc sulfide shell of known thicknesses grown on cadmium selenide nanocrystals is then discussed in Chapter 3. Chapter 4 focuses on the effect of intercalating copper between the layers of bismuth selenide nanoribbons on the phase transition of this material. A better understanding of the mechanism of the wurtzite to rocksalt structural phase transition was gained through the shock compression of cadmium sulfide and is presented in Chapter 5. Progress towards single particle fluorescence imaging inside a diamond anvil cell is discussed in Chapter 6. One possible application of the high pressure properties of nanocrystals for use as a biological force detection is explored in Chapter 7. Future prospects for investigating the behavior of phase transitions in nanoparticles are presented in Chapter 8.

# Chapter 2
# Experimental Techniques

## 2.1 Abstract

This chapter introduces the reader to techniques for high pressure generation and the synthesis of semiconductor nanocrystals. A brief discussion of diamond anvil cells and shock waves is provided. A general discussion of the reaction procedure used for semiconductor nanocrystals is supplied. A detailed description of the syntheses performed for the work in this dissertation can be found in each chapter.

## 2.2 Introduction

The application of high pressure to a sample is becoming increasingly important in a multitude of fields, including chemistry, physics and biology. High pressure experimentation allows for scientists to investigate, in a reversible manner, the effects of changing the volume of a material. Under high pressure, various phenomena have been observed, including structural, electronic, and magnetic phase transitions. Depending on the pressures that need to be achieved for a particular experiment, the pressure conditions to be used, and the geometric requirements of the monitoring technique, various methods to achieve high pressure exist. Two of these methods, diamond anvil cells and shock waves, are discussed below.

In addition to the high pressure techniques used throughout this dissertation, a general discussion of the synthesis of semiconductor nanocrystals is presented in Section 4.

## 2.3 High Pressure Techniques

Pressure is a fundamental variable in thermodynamics. Changing the pressure that is exerted on a system changes the energy of that system. As a result, it is an extremely important variable to consider when looking at the thermodynamics of a material. An important consideration when performing experiments under high pressure is the nature of the pressure:

hydrostatic or non-hydrostatic pressure (Figure 2.1). Hydrostatic, or isotropic, pressure is when the same pressure is exerted on the sample from all directions. Non-hydrostatic, or anisotropic, pressure occurs when at least one part of the sample experiences more or less pressure than other parts of the sample. If the pressure is directed only in one direction, the non-hydrostatic pressure is called a uniaxial pressure. In the case of non-hydrostatic, the sample will more than likely change its shape, while a hydrostatic pressure changes the size but not the shape.

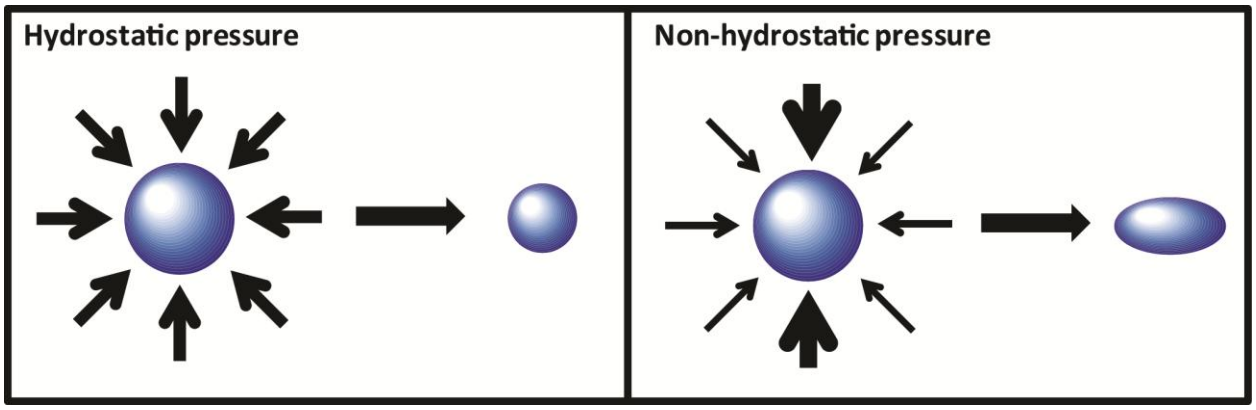


**Figure 2.1:** Hydrostatic pressure exerts an isotropic force on the sample yielding no shape change. Non-hydrostatic pressure exerts an anisotropic force on the sample and yields a shape change.

The nature of the pressure can be controlled through the high pressure experimental method chosen. Diamond anvil cells can be used to exert a hydrostatic or non-hydrostatic pressure, as determined by the nature of the pressure transmitting medium chosen. Shock waves typically produce an anisotropic, transient pressure.

### *2.3.1 Diamond Anvil Cells*

Diamond anvil cells (DACs) are a commonly used tool for exerting a static pressure on a sample up to about 100-150 GPa. A DAC typically consists of two opposing diamonds with flat culets that press on the gasketed sample between them (Figure 2.2).[29] As the backing plates on which the diamonds are adhered are pushed closer and closer together, a pressure is exerted on the sample located between the diamonds. Type I or type II diamonds can be used, with type II diamonds being significantly more expensive, but possessing fewer defects within the crystal lattice. Diamonds should be chosen for the characterization method to be employed. For instance, Raman spectroscopy requires diamonds with low fluorescence, a property that can be found in both type I and type II diamonds.[29] Diamonds in the experiments discussed in this dissertation were about 0.25 carat and brilliant cut.

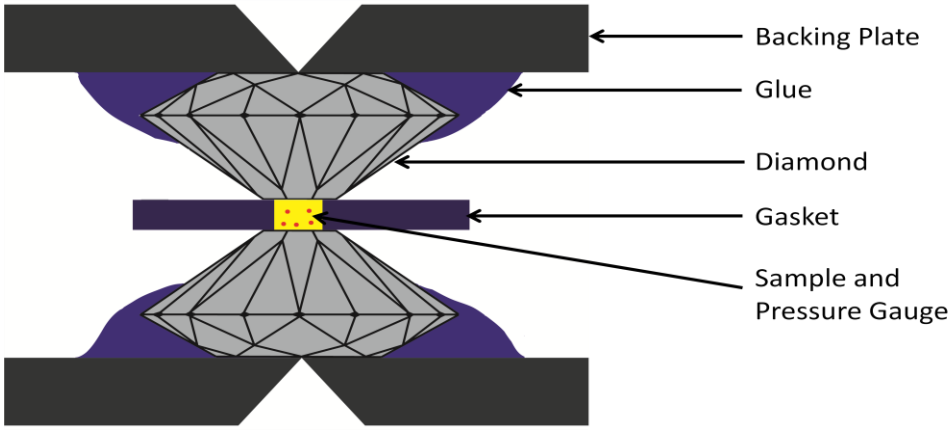


**Figure 2.2:** Schematic of a typical diamond anvil cell.

Diamond anvil cells come in a variety of shapes and sizes.[29,39-40] Each type of cell has its advantages and disadvantages depending on the application to which it will be applied. Several types of diamond anvil cells are shown in Figure 2.3. A symmetric diamond anvil cell is well suited for achieving high pressures and its large aperture on each side of the cell makes it ideal for use in X-ray diffraction experiments.[40] The Diacell membrane piston-cylinder cells are also capable of achieving high pressures, with the pressure being controlled through the use of screws or the inflation of a membrane that pushes down on the cylinder.[41] The Diacell cells are convenient when the cell cannot be moved between measurements to adjust the pressure. A Merrill-Bassett DAC is a compact device ideally suited for experiments where working distance is a concern.[42] It is not capable of reaching extremely high pressures, but its small size makes it a convenient addition to the high pressure toolbox.

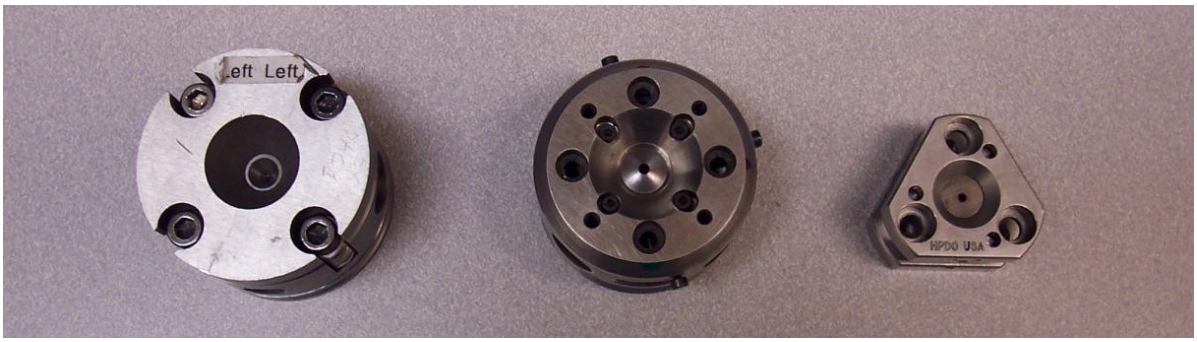


**Figure 2.3:** Photograph of a symmetric diamond anvil cell (left), a Diacell piston cylinder/membrane cell (center), and a Merrill-Bassett diamond anvil cell (right).

Besides the diamonds, the gasket is the part of the cell that most greatly influences the ability of the DAC to achieve high pressures. The gasket between the diamonds serves as a sample chamber and an easy method for keeping the diamonds from coming into contact with one another. The gasket provides the lateral support for the diamonds; thicker gaskets provide

more support. Unfortunately, this comes with the caveat that a thicker gasket requires more force, which increases the risk of breaking the diamonds. Thus a balance must be found between the pressure to be achieved and the amount of support necessary to avoid breakage.[29] The gasket can also determine what geometry the sample can be observed from. For an axial geometry (probing and collecting through the diamonds), metal gaskets, including stainless steel, spring steel, and rhenium are typically used.[28-29] Typically the harder metals are used for experiments that are to reach higher pressures. In a radial geometry (probing and collecting between the diamonds), beryllium and boron epoxy gaskets can be used.[43] Because of its toxicity, the use of beryllium is usually avoided. A gasket also supports the sample material under pressure, which increases the maximum pressure that is achievable.[28-29] A gasket is usually pre-indented with the diamonds before the hole is drilled. This prevents the flow of the metal as the pressure is increased from filling in the sample hole and helps the mechanical stability of the gasket. The gasket can be drilled through the use of a mechanical drill, an electrostatic drill, or a laser miller. The drilling method used should yield a uniform hole free of burrs on the edge. A schematic of a pre-indented and drilled gasket is shown in Figure 2.4.

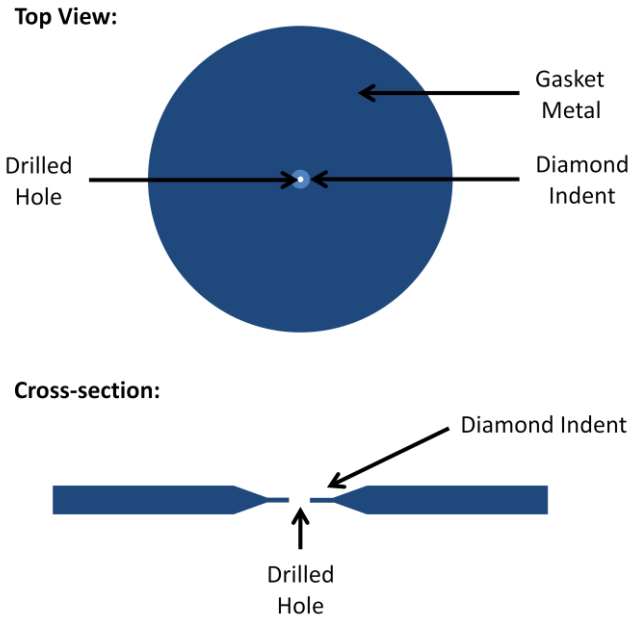


**Figure 2.4:** Schematic view of a gasket used as the sample chamber in a diamond anvil cell.

The medium that surrounds the sample in the gasket chamber is also extremely important. The medium can be a gas, solid, or a liquid. Pressure transmitting media that are liquids under ambient conditions are the easiest to load. An important consideration when choosing a pressure transmitting medium is whether or not it has been shown to exert hydrostatic pressure on the sample in the chamber. In addition, for nanoparticles, it is important that the particles are soluble in the medium for ease of loading and in order to avoid coupling between particles. A complete list of pressure transmitting media can be found elsewhere,[28] but those relevant to the studies shown here are ethylcyclohexane and a 1:1 mixture of pentane-isopentane, both of which are hydrostatic or quasi-hydrostatic below about 10 GPa.[28]

In addition to the sample and the pressure transmitting medium, the pressure calibrant must also be included in the sample chamber. Various manometers have been calibrated for use at the pressures commonly found in DACs, but by far the most commonly used is ruby ($\alpha$-$Al_2O_3$ doped with $Cr^{3+}$). The fluorescence of the ruby R1 and R2 is known to shift at a rate of 0.365 nm/GPa.[44] This is an easily measured quantity. The splitting and broadening of these peaks with increasing pressure can also be used to help determine the nature of the pressure inside the DAC (hydrostatic versus non-hydrostatic). When excited with a blue or a green laser, an electron in the ground state of the ruby is excited to the Y ($^4T_1$) or U ($^4T_2$) band. It then nonradiatively decays to the $E_2$ level, which is split into 2 levels due to the crystal field. Next, it radiatively decays to emit the R1 and R2 lines in the ruby fluorescence spectrum (Figure 2.5).[44] Other optical sensors include $Sm^{2+}$ doped $SrB_4O_7$, BaFCl, and SrFCl and $Eu^{3+}$ doped LaOCl and $Y_3Al_5O_{12}$.[28] These have a range of sensitivities and can in some cases also be used to determine temperature.[28]

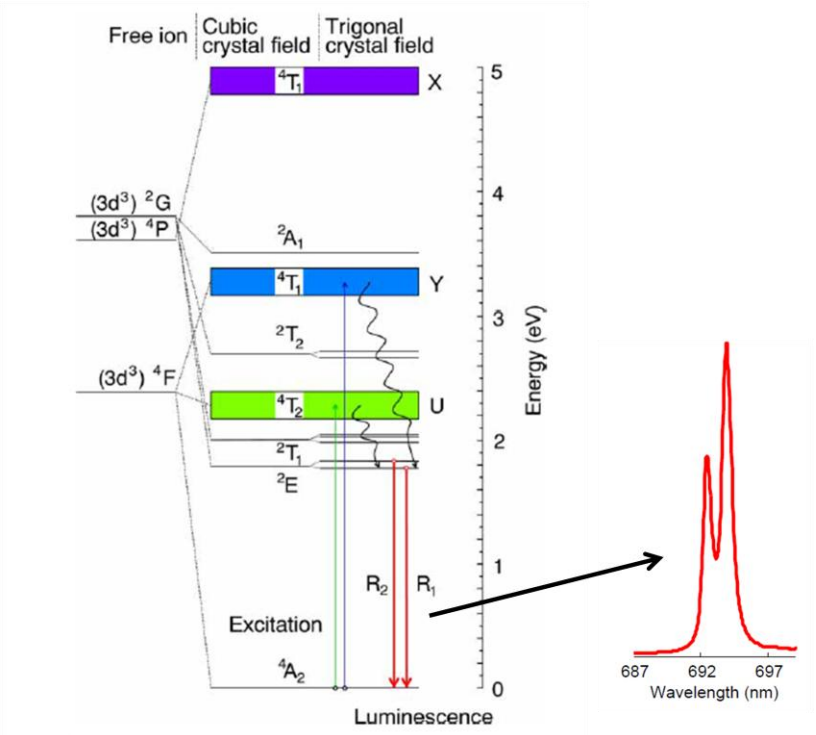


**Figure 2.5:** Schematic of the electronic levels present in ruby and the R1 and R2 ruby fluorescence spectrum. (Figure adapted from Reference 44)

In addition to optical manometers, diffraction standards with known equations of states can be used in a DAC. Commonly used diffraction calibrants are NaCl, $CaF_2$ (fluorite), $SiO_2$ (quartz), CsCl, Al, Au, Pd, Pt, and Ag.[28,45] For some of the experiments in this work, the X-ray diffraction pattern of a small piece of gold included in the sample chamber was used to determine the pressure in the DAC. The equation of state for gold was used to determine the pressure from the unit cell volume.[46] An example is shown in Figure 2.6.

A detailed description of the procedures used to maintain and operate a DAC, including, alignment and loading procedures, is given in Appendix A.

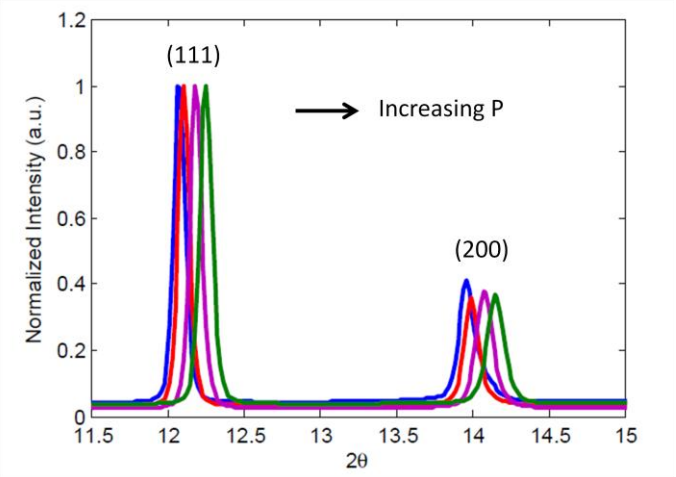


**Figure 2.6:** X-ray diffraction patterns of Au with increasing pressure. Synchrotron radiation at a wavelength of 0.4959 nm was used.

Common methods of monitoring a sample optically in a DAC include absorption and fluorescence. In order to achieve these, several challenges had to be considered in order to accommodate the DAC in the optical path. A diagram of the microscope that was built to address these challenges is given in Figure 2.7. The microscope centers around a Zeiss Axiovert inverted microscope. A Lexel 95 $Ar^+$ ion laser with a 5 W tube was used as an excitation source. Typically, the sample was illuminated with the 488 nm line of the laser. The laser power was controlled using neutral density filters. Because of the size of a DAC, a long working distance objective must be used. A Zeiss 50× objective with a working distance of 9 mm or a Nikon 20× objective with a working distance of 23 mm were used to focus within the DAC in an epiluminescence geometry. To illuminate the sample, a small beam size, typically 5-10 μm, was necessary to fit within the gasket hole. In general, such a small beam size can be achieved by using a larger beam size into the back of the objective. The Zeiss Axiovert microscope has a built in lens in the back of the microscope for use with a halogen lamp. This lens focuses the laser beam that is directed through the back port to a small point, yielding a large spot size at the focal point of the objective. Instead of removing the lens, an additional lens was incorporated into the beam path to adjust the beam such that it was collimated upon reaching the back of the objective. In this way, a small beam size at the sample could easily be achieved. The emitted light from the sample in the DAC was then be directed out of the side port of the microscope and through the slits of an Princeton Instruments Acton SpectroPro 300i spectrometer. The light was dispersed using a 300 blaze/mm grating for the sample emission and a 1200 blaze/mm grating for the ruby emission. The signal was then collected using a Princeton Instruments Spec-10 liquid nitrogen cooled CCD. The absorption of the sample within the DAC was collected in a similar way through the use of a 12V, 100W halogen lamp mounted above the DAC. The signal collected by the CCD in this case was corrected for the lamp profile in post-collection data analysis. A setup such as this could easily be modified for Raman spectroscopy.

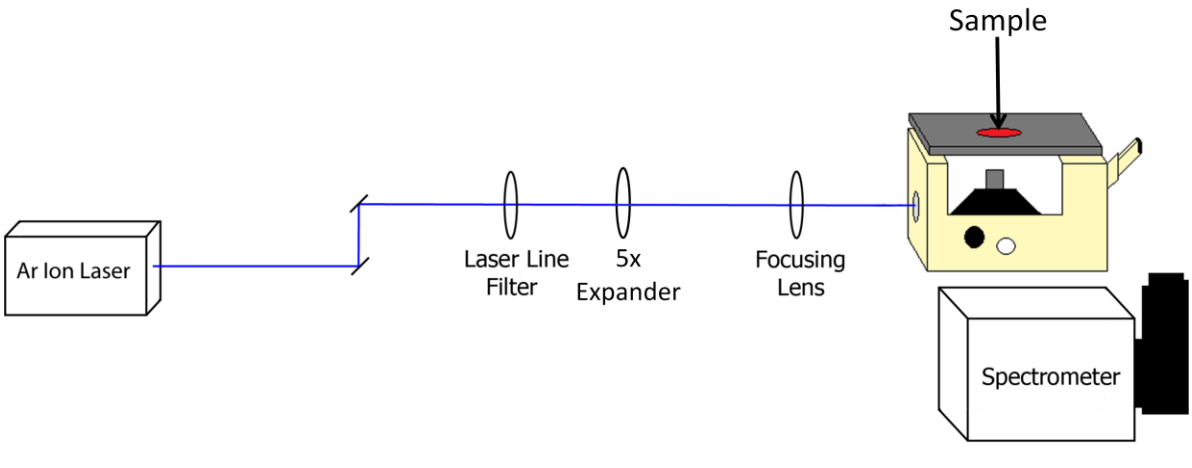


**Figure 2.7:** A schematic of the absorption and fluorescence microscope used to monitor samples within the diamond anvil cell.

In addition to optical measurements, it is useful to perform X-ray diffraction experiments in a DAC in order to help determine the structural changes that occur in a sample while it is under pressure. The diamonds, being single crystals themselves, will also diffract the X-rays used to probe the sample. In addition, depending on the X-ray wavelength used, the diamonds may also absorb some of the light. Because a high X-ray flux is needed to monitor samples within the DAC, experiments requiring X-rays are typically performed at a synchrotron. At Lawrence Berkeley National Lab, beamline 12.2.2 of the Advanced Light Source is specifically set up to address the challenges of high pressure X-ray diffraction.[47] X-ray diffraction patterns can be achieved using an axial or radial geometry. In the axial geometry, the beam is directed into the DAC through one of the diamonds and the diffraction pattern is collected in a transmitted geometry through the other diamond (Figure 2.8). The Bruker image plate data was then be integrated in Fit2D to create the X-ray diffraction pattern.

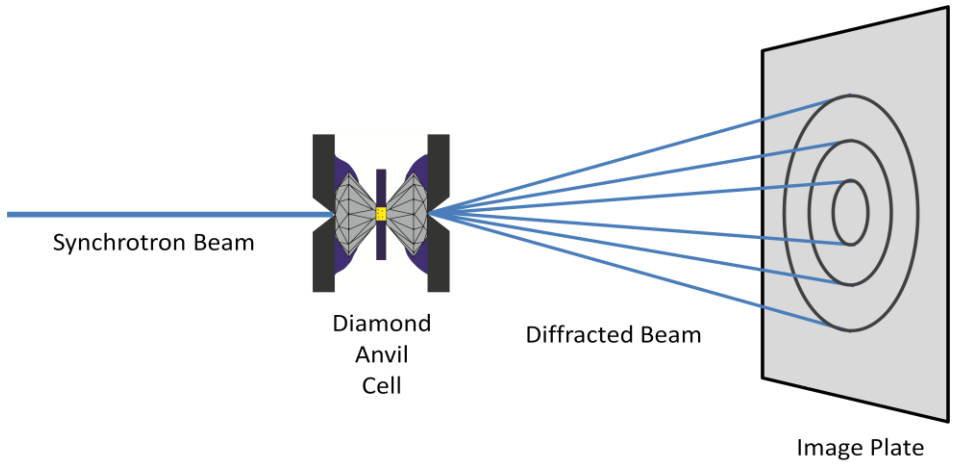


**Figure 2.8:** A diagram of a synchrotron X-ray diffraction experiment performed in a diamond anvil cell.

### *2.3.2 Shock Waves*

The generation of shock waves has provided a method by which scientists can probe dynamic, uniaxial compression in materials. Before considering the method by which shock waves were generated, it is important to first briefly discuss the theory behind shock waves as it tends to significantly differ from that which is normally discussed for static pressure experiments performed in a DAC.

Shock waves are typically defined as a plane moving in 1-dimension through a material that causes a sudden, almost instantaneous change in the thermodynamic parameters, including pressure, temperature, and volume. Unlike an acoustic wave, which does not cause an overall change in the average density of a material (it only causes small local changes), a shock wave can cause a significant change in the density as it traverses the material (Figure 2.9). When a shock wave transverses through a material, a large number of defects can be created during the shock and are left behind once the material has return to ambient conditions. A shock wave is also supersonic, meaning that it travels faster that the speed of sound that is supported by the material ahead of the shock front.

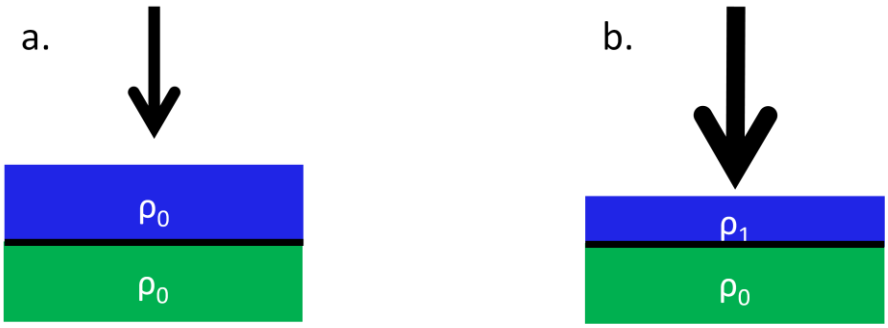


**Figure 2.9:** a.) A sound wave traversing a material. The density is the same before and after the acoustic wave (black line). b.) A shock wave traversing a material. The density behind the shock front (black line) can be significantly higher than the density in front of the shock.

A shock wave can be described through the use of its jump equations. These equations define the conservation of mass, momentum, and energy that the shock wave must adhere to due to thermodynamics. These equations relate the properties of the material behind the shock front (state 2) to those of the material in front of the shock (state 1):

$$\text{Mass Conservation: } \rho_1(U_2-u_1)=\rho_2(U_2-u_2) \quad (2.1)$$

$$\text{Momentum Conservation: } P_2-P_1=\rho_1(U_2-u_1)(u_2-u_1) \quad (2.2)$$

$$\text{Energy Conservation: } E_2-E_1=(P_2+P_1)(v_1-v_2)/2, \quad (2.3)$$

where, ρ is the density (g/cm$^3$), U is the shock velocity (cm/μs), u is the particle velocity (cm/μs), v is the specific volume (cm$^3$/g, 1/ρ), P is the pressure (Mbar), and E is the internal energy (Mbar-cm$^3$/g).[48-49] The shock velocity, U, and the particle velocity, u, are different parameters. The shock velocity is defined as the distance that the wave has travelled divided by the time it took to travel that distance. The particle velocity, on the other hand, is the speed at which the particles in the material are moving as the shock front traverses the material. The shock velocity is faster than the particle velocity, as the electromagnetic forces between the atoms in the material push against the surrounding atoms with a force increasing with decreasing distance, thus allowing the shock front to travel faster than the atom movement.[48]

The conservation or jump equations (Equations 2.1- 2.3) can be plotted in the form of a Hugoniot curve (Figure 2.10).[49] Unlike an isoentrope (green line in Figure 2.10), one cannot simply go from one point to the next continuously on a Hugoniot curve. Each point on a Hugoniot curve is constructed from drawing a line from the initial state of the material ($P_0$,$V_0$) to the final state of the material ($P_1$, $V_1$), called the Rayleigh line (blue dashed line in Figure 2.10). Each point must be determined independently, thus making the Hugoniot a representation of final shocked states. Because the process is irreversible, the Hugoniot is constructed from a series of shock experiments starting from the same initial conditions.

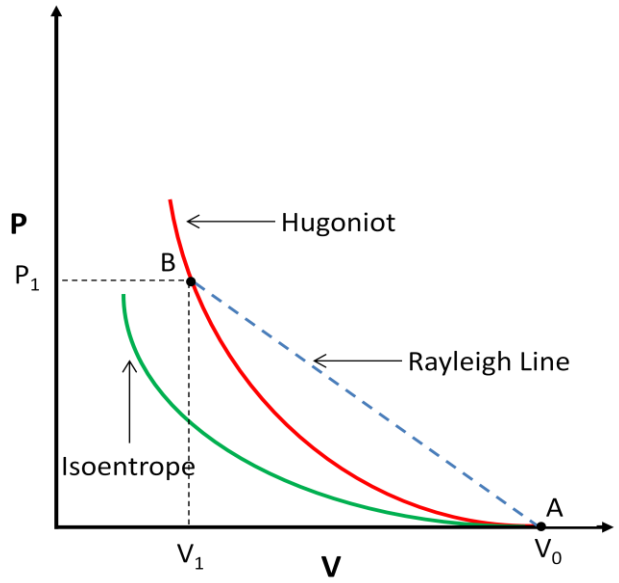


**Figure 2.10:** Schematic showing the P-V Hugoniot, a Rayleigh line, and an isoentrope for a material.

As shown above, there is a pressure change in the material due to the shock wave. This stress can be divided into two components: the mean pressure and the shearing stress. The isotropic mean pressure, $\bar{p}$, is defined as:

$$\bar{p} = \frac{(p_x+p_y+p_z)}{3} = \frac{(p_x+2p_y)}{3}, \tag{2.4}$$

where $p_i$ are components of the pressure tensor and the shock wave is travelling in the x-direction.[50] The shearing stress, $\tau$, is defined as:[50]

$$\tau = \frac{(p_x - p_y)}{2}. \tag{2.5}$$

This gives the total pressure measured in a shock wave as:[50]

$$p_x = \frac{(p_x + 2p_y)}{3} + \frac{2(p_x - p_y)}{3} = \bar{p} + \frac{4\tau}{3}. \tag{2.6}$$

In this case $\tau$ is defined as the shear stress on planes with normals 45° to the x-direction. The value of $\bar{p}$ can be equated to the hydrostatic pressure of static pressure techniques, such as diamond anvil cells.[50]

In addition to a pressure increase, the shock wave also causes a change in the temperature of the sample.[49] This temperature rise corresponds to:[49]

$$T_1 = T_0 e^{\Gamma \Delta V} + \int_{V_0}^{V_1} \frac{f(V) e^{\Gamma \Delta V}}{C_V} dV, \tag{2.7}$$

where

$$f(V) = \left[\frac{1}{2}(V_0 - V_1)\frac{dP}{dV} + \frac{1}{2}P\right]. \tag{2.8}$$

In Equations 2.7 and 2.8 $\Delta V = 1 - V_1/V_0$, $\Gamma$ is the Grüneisen coefficient, $C_V$ is the constant volume heat capacity, and P is the pressure.

Shock waves can be generated by a number of different methods. Recently, a relatively simple method using an ultrafast laser to rapidly ablate a thin layer of aluminum thereby launching a shock wave through the material following the aluminum in the sample stack (Figure 2.11).[51] The sample can then be probed from the other side of the stack using a number of spectroscopic methods. In the case of an X-ray probe, such as a femtosecond pulse from the free-electron laser at the Linac Coherent Light Source (LCLS) at the SLAC National Accelerator Laboratory at Stanford University, the probe beam can be aligned in-line with the pump beam since the material before the sample in the stack is fairly transparent to the X-ray beam (with the exception of the aluminum, see below). The buffer layer serves the purpose of allowing the shock front to steepen before it reaches the sample layer.[52]

The pressure reached by the shock wave travelling through the sample can be determined by a number of methods. A pressure sensitive dye, such as Rhodamine-640, can be included in the sample as a calibration standard.[53-54] Another option for measuring the shock pressure is to use the equation of state for the aluminum layer. This can only be used in experiments involving a X-ray probe.

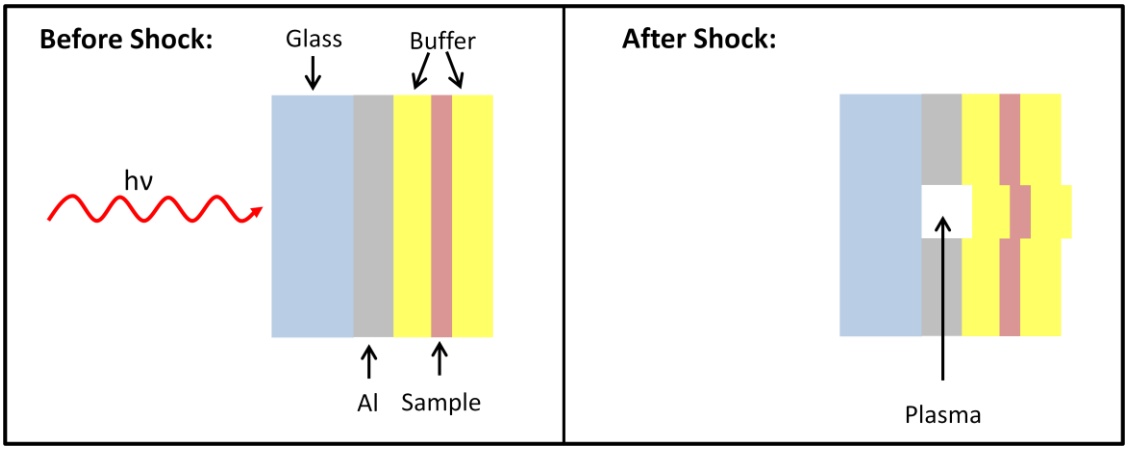


**Figure 2.11:** An example of the sample stack used to create a shock wave by laser ablation.

### *2.3.3 High Pressure Diffraction Pattern Analysis*

Diffraction patterns for the static and dynamic pressures generated in this dissertation were analyzed using two different methods. Rietveld refinement is a convenient procedure by which the structural composition and lattice parameters can be extracted from diffraction data in a quantitative way.[55] Rietveld refinement uses a least squares method to refine a theoretical pattern to match that of an experimental pattern.[56] Multiple theoretical patterns can be input into the analysis in the case of a mixture of phases. The method is unique in that it is able to handle overlapping diffraction peaks in a reliable manner. The refined lattice parameters, percent composition, and particle size (from the Scherrer equation) can be found by using Rietveld refinement.[55,57] A computer program entitled Materials Analysis Using Diffraction (MAUD) has been developed for performing Rietveld refinement on diffraction patterns.[58] MAUD was extremely useful for the analysis of high pressure diffraction patterns.

For some samples, the background induced from the surrounding medium was too significant, thus a simple fitting method in Fityk[59] or OriginPro 8 was used instead of Rietveld refinement.

### *2.3.4 Relevant Parameters Extracted from High Pressure Experiments*

In addition to the structural phase of the material, high pressure experiments can provide insight into the properties of the material under investigation. For instance, when the optical properties of a semiconductor material under high pressure are investigated, the pressure dependence of the bandgap can be measured. Such an experiment provides details on whether the bandgap shifts linearly or sub-linearly with pressure. The optical properties of the materials can also give insight into the structure of the material. For instance, II-VI semiconductors in the wurtzite or zinc blende structures are direct gap semiconductors exhibiting excitonic structure in their absorption and fluorescence.[15-17] The same semiconductors in their high pressure rock salt phase are indirect gap semiconductors, meaning that the absorption spectrum is featureless and

the fluorescence is forbidden (it now requires a change in the k-vector in addition to the change in energy).[15-17]

From the X-ray diffraction patterns, the volume of the unit cell can be monitored with changes in pressure. This can provide the bulk modulus of the material. The bulk modulus defines the resistance of the materials to uniform compression, such as that in a diamond anvil cell. It is usually represented by the variable B or K and can be calculated through the use of the equation:

$$B = -V\frac{dP}{dV}, \tag{2.9}$$

where P is the pressure and V is the volume.

Since both optical and X-ray diffraction measurements give information about the structural phase of the material, data from both can be used to construct a hysteresis curve. A hysteresis curve essentially maps out the phase of the material versus the pressure. The phase can be represented by the volume of the unit cell, the presence or absence of an absorption or fluorescence feature, or any other parameter that changes when the phase transition occurs. A hysteresis curve is constructed by plotting the chosen property against the pressure for both the upstroke and the downstroke of the pressure sequence. From the resulting loop, information about the thermodynamics and the kinetics can be obtained.

## 2.4 Nanoparticle Synthesis

The colloidal synthesis of semiconductor nanoparticles has become a standard procedure in many laboratories. The colloidal nature of these particles provides for solubility in a variety of solvents. This allows for the particles to be incorporated into polymer, reacted with other components in solution, or to be deposited as a solid. This method allows for the facile synthesis of multi-component nanostructures through the addition of new reagents and for the control of the shape of the nanostructure. Nanocrystals shaped as dots, rods, tetrapods, and hyper-branched structures are now regularly synthesized in a reliable manner.[2,21-22] The composition of these structures can be controlled such that different components of the structure can be made of different materials, allowing for tuning of the optical, catalytic, and mechanical properties of the resulting nanomaterial.[21-22]

A general synthetic scheme will be discussed in this chapter. The specifics for the synthesis of each material used for the work in this dissertation will be discussed in the respective chapter.

The typical synthetic setup for semiconductor nanoparticles is shown in Figure 2.12. Nanoparticles were synthesized using standard air free techniques on a Schlenk line. In a standard reaction, the cation precursor (metal salt or oxide) and the chosen ligand system were loaded into a 3-neck round-bottom flask equipped with a thermocouple adapter, condenser, septum, and magnetic stir bar. The system was purged with argon or nitrogen before being

heated. The temperature was controlled by a heating mantle and measured by a thermocouple. The system was rid of oxygen, water, and other low boiling point impurities by placing the it under vacuum for 1-2 hours. The reaction system was then backfilled with argon and heated to the temperature desired for injection. The anion solution was rapidly injected into the cation solution. For nanoparticles with a narrow size dispersion, the injection was performed as quickly as possible using a large gauge needle. The resulting nanoparticle solution was cooled down to room temperature. Cleaning of the particles was realized by the addition of an anti-solvent until the solution was opaque, followed by centrifugation to yield a pellet of nanoparticles. This pellet was then dissolved in a solvent (typically hexane or toluene), precipitated again with anti-solvent (acetone or methanol), and centrifuged. The process was repeated until a clear solution of nanoparticles was achieved.

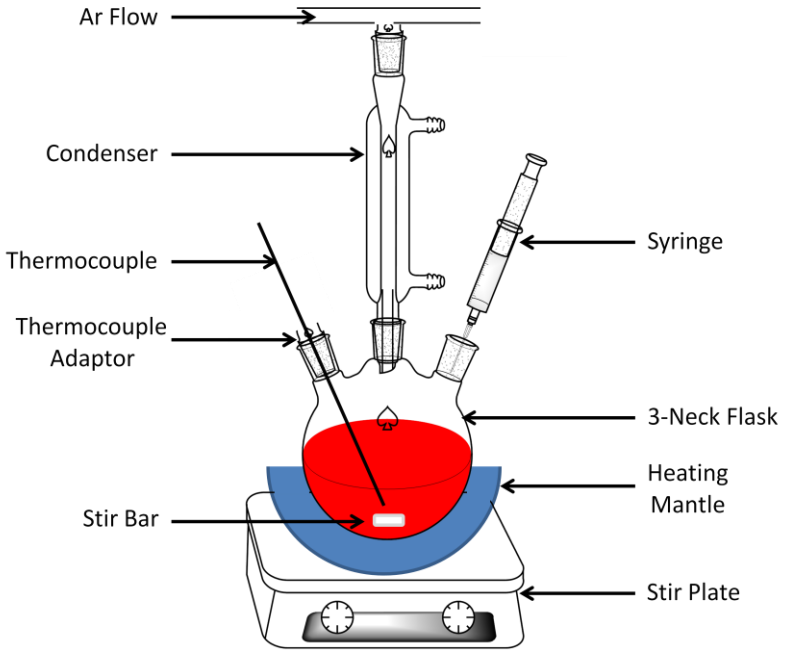


**Figure 2.12:** Schematic showing the typical reaction setup for colloidal semiconductor nanoparticles.

## 2.4 Conclusion

Methods for the generation of high pressure and the synthesis of semiconductor nanocrystals have been discussed in general in this chapter. The specifics of each experiment and synthesis are related in full in their respective chapters.

# Chapter 3

# Structural Phase Transitions and Fluorescence Splitting in Core/Shell Nanocrystals

## 3.1 Abstract

High pressure solid-solid phase transitions are strongly dependent on the size of the nanocrystal. The size dependence of the wurtzite to rocksalt phase transition has been extensively investigated for core-only CdSe nanocrystals, yet relatively fewer studies have examined the same phase transition in more complex nanocrystals heterostructures. CdSe/ZnS core/shell nanocrystals, a prototypical quantum dot system, were synthesized using a successive ion layer absorption and reaction procedure in order to control the shell thickness. In order to investigate the high pressure phase transition, the resulting particles were placed into a diamond anvil and probed using X-ray diffraction, optical absorbance, and fluorescence. The phase transition hysteresis loops were determined to be dependent on the thickness of the zinc sulfide shell, indicating changes in both the kinetics and the thermodynamics of the transformation. It was also found that the mismatch defects are present in the shell for thicknesses greater than one monolayer, and that fluorescence of the core/shell particles splits into multiple peaks under pressure due to the presence of the shell. This study highlights the importance of small structural changes in regard to the high pressure behavior of nanomaterials, and provides insight into how the forces exerted by the shell influence the core structurally.

## 3.2 Introduction

Phase transitions are formally defined for systems in which the number of atoms is very large, and the structural phase diagram is typically considered in terms of pressure and temperature. Yet there is a size dependence for phase transitions in small systems. The evolution of the phase diagram as a function of the size in the nanometer size regime is a topic of much current interest. In nanocrystals, which consist of hundreds to thousands of atoms, the surface of the material contributes significantly to the thermodynamics of the system. The surface energy contribution to the energy is different in each phase, and leads to a size

dependence of the phase transition. The most well known and dramatic effect of size on a phase transition occurs for melting, where the melting temperature of small nanocrystals can be less than 50% of that of the bulk material.[11] Melting is a particularly simple case in which to investigate the nanoscale size dependence, because nucleation is facile. Typically there is very little hysteresis in this transition for systems comprised of hundreds of atoms or more, and an abrupt change from solid to liquid and back can typically be observed.

The pressure induced structural transformation in cadmium selenide (CdSe) nanocrystals has become a model system for studying the size dependence of solid-solid phase transitions.[6-8,13-14,32-35] During this transition, cadmium selenide transforms from a tetrahedrally coordinated wurtzite or zinc blende crystal structure to the octahedrally coordinated rocksalt structure, accompanied by a decrease in volume on the order of 20%.[33] The nanocrystalline CdSe solid-solid phase transition also exhibits a hysteresis that is approximately three times that of the bulk transition.[7] This increased hysteresis width is due to the lack of defects present in nanocrystals, indicating that the transition is under kinetic control, due to a larger barrier for the nucleation of the new phase.[7] It has been proposed that as the size of the system is reduced, it reaches a point where a true solid-solid phase transition ceases to occur and it should be considered more along the lines of a molecular isomerization.[7]

The mid-point of the hysteresis loop of the structural transformation provides a measure of the thermodynamic transition point. For CdSe nanocrystals, the phase transition occurs at significantly higher pressures than for the bulk material. For instance, a particle with a 2 nm diameter undergoes the wurtzite to rock salt transformation at 4.9 GPa; whereas, a particle with a diameter of 4.2 nm has a transition at 3.6 GPa.[6] In comparison, the bulk transition occurs between 2.0-3.0 GPa.[16-17] Furthermore, the upstroke phase transition pressure for 2 nm CdSe particles is about 9 GPa, while it is only about 7 GPa for 4.2 nm CdSe nanoparticles.[6] The fact the upstroke phase transition is significantly higher than the thermodynamics phase transition pressure is indicative of the presence of a large energy barrier that must be overcome in order for the phase transition to occur.

Simulations of nanocrystals under high pressure have previously shown that the nucleation of the new phase occurs on the surface, followed by its propagation across the entire nanocrystal.[60-61] Typically a single nucleation front can move across a nanocrystal before a second nucleation event can occur, so that the nanocrystal behaves as a single domain, analogous to a single domain nanoscale magnet. Given this, it can be easily imagined that altering the surface in some fashion will change the conditions under which the phase transition occurs. Advances in the synthesis of colloidal nanocrystals have yielded a facile method for the creation of more complex nanostructures where the surface can be modified through the addition of an inorganic shells with differing lattice mismatches and moduli around the outside of the core particle.[19-20] The properties of such a core/shell particle can be compared to those of a quantum well, as both consist of layered structures whose properties are dependent of the lattice mismatch between the chosen materials and the layer thickness.

High pressure quantum well experiments point to the ability to tune the phase transition behavior through layer thickness and composition. Such behavior has been previously observed in AlAs/GaAs[62-64] and CdTe/ZnTe[65-67] quantum wells, where not only was there a change in the

phase transition conditions, but the kinetics of the phase transition also differed with changes in layer thickness. For AlAs/GaAs, Weinstein fit the phase transition behavior to an equation based on the layer thickness and the lattice mismatch.[62-64] This relation works for the AlAs/GaAs system, but is not universally applicable.

Previous high pressure experiments on CdSe/ZnS core/shell experiments have found that the phase transition in these particles occurs at a higher upstroke pressure relative to pure CdSe nanoparticles of a similar size.[67-68] These experiments did not include an investigation of the thermodynamic phase transition conditions. In addition, it was found that the addition of the ZnS shell changes the kinetics of the reverse transition relative to uncapped particles.[69] To our knowledge, no study of the effect of the shell thickness on the phase transition has been performed. Simulations suggest that there should be a shell thickness dependence for this phase transition and indicate the possibility of the formation of new stable biphasic structures.[70]

In the present work, the dependence of the wurtzite to rocksalt phase transition on the shell thickness was determined. High pressure X-ray diffraction and optical measurements were carried out in a diamond anvil cell to provide insight into the structure and electronic properties of the material. Similar to the results from quantum wells, the phase transition pressure was found to depend on the shell thickness when few defects were present at the interface between the materials. The variation of the structural and electronic properties with shell thickness was highly non-monotonic, revealing a complex interplay of structural and electronic phenomena. Even for thin shells, the shell material was found to exert an anisotropic force on the nanocrystals. Further, there was strong evidence that a pure ZnS shell breaks up into domains on the nanocrystal surface at very thin layers between one and two monolayers, confirming the need for a transition layer of CdS when thicker shells are grown. The work demonstrates that the phase transition conditions can be modified through a small change in the structure of the quantum dot.

## 3.3 Experimental

### *3.3.1 Synthesis*

CdSe nanocrystals were prepared using a literature procedure.[71] Core/shell particles were synthesized using a successive ion layer absorption and reaction (SILAR) procedure similar to those presented in References 72 and 73.

**Reagents:** Cadmium oxide (CdO, 99.99%), stearic acid (98%), and 1-octadecene (ODE, 90%) were purchased from Alfa Aesar. Octadecylamine (ODA, 97%), selenium powder (99.99%, -100 mesh), zinc oxide (ZnO, 99.9% powder, < 5 μm), oleic acid (90%), ethylcyclohexane (99%), methanol, acetone, hexane, and toluene were purchased from Sigma-Aldrich. Trioctylphosphine oxide (TOPO, 90%) and tributylphosphine (TBP, 99%) were purchased from STREM. Sulfur powder (sublimed) was purchased from Fisher. NOTE: TBP is slightly pyrophoric and should be handled accordingly.

**Cadmium Selenide Cores:** In a small vial, 158 mg of Se powder and 0.472 g TBP were combined and stirred at room temperature under argon until the mixture went clear and colorless. In a 25 mL three-neck roundbottom flask equipped with a condenser, thermocouple adapter, magnetic stir bar, and septum, 25 mg of CdO, 227 mg of stearic acid, and 2.53 mL of ODE were combined. Under flowing argon, the mixture was heated to 200 °C. When the solution turned clear and colorless, the reaction mixture was cooled down to room temperature. ODA (1.5 g) and 0.5 g of TOPO were added to the reaction and the reaction was heated to 280 °C under argon. The TBP:Se precursor was then quickly injected into the mixture quickly using a 16-gauge needle. The reaction was grown for 30 seconds to yield nanoparticles about 3.5 nm in diameter. Size control could be achieved by varying the growth time after the injection. The reaction mixture was cooled rapidly to room temperature, where about 7 mL of hexane was added and the entire solution was transferred to a glovebox. The resulting nanoparticles were cleaned first by layering the reaction mixture with methanol and removing the resulting colorless or white layer several times. Subsequent cleaning was performed through the addition of acetone until the colored solution was cloudy followed by centrifugation. The resulting pellet was dissolved in hexane or toluene and the precipitation procedure was repeated until a clear, colored solution in hexane was achieved. The solution concentration of the CdSe nanocrystals was determined using the equations from Reference 74.

**$Zn(oleate)_2$ Precursor:** In a 50 mL three neck roundbottom flask equipped with a condenser, thermocouple adapter, magnetic stir bar, and septum, 203 mg of ZnO, 6.91 mL of oleic acid, and 18 mL of ODE were combined. The mixture was heated to 250 °C under flowing argon. When all of the ZnO had dissolved, the precursor solution was cooled to 70 °C and transferred to a purged Schlenk flask, before cooling to room temperature. Injections for the SILAR reaction (see below) were performed with the zinc precursor solution at 80 °C to prevent the solidification of the zinc oleate.

**Sulfur precursor:** In a 50 mL three neck roundbottom flask equipped with a condenser, thermocouple adapter, magnetic stir bar, and septum, 64 mg of sulfur and 20 mL of ODE were combined. The mixture was heated to 170 °C under flowing argon until the sulfur was completely dissolved. The solution was then cooled to room temperature and transferred to a purged vial for future use. Injections for the SILAR reaction (see below) were performed with the sulfur precursor at room temperature.

**Shell Deposition:** The amount of each precursor needed for each layer was calculated according to the method described in the literature.[23] In a 50 mL three neck roundbottom flask equipped with a condenser, thermocouple adapter, magnetic stir bar, and septum, 3 mL of ODE and 1 g of ODA were combined. The mixture was heated to 100 °C under vacuum for 1 hour. After 1 hour, the reaction flask was backfilled with argon and $1.83\times10^{-7}$ moles of CdSe nanocrystals in hexane were injected. The solution was then heated to 120 °C under vacuum for 45 minutes to remove the hexane. The reaction flask was then backfilled with argon and heated to 190 °C. Enough of the zinc precursor for a single monolayer was then added over several minutes in a dropwise manner. The reaction was then allowed to stir for 20 minutes before the same amount of sulfur was added dropwise and the particles were again allowed to react again for 20 minutes. Subsequent injections could be done at 210 °C. Temperatures higher than these yielded some alloying, as indicated by a blue shift in the absorption. The procedure was repeated until the

desired shell thickness was reached. Once the desired shell thickness was achieved, the reaction mixture was cooled down to room temperature and the solution was transferred to a glovebox. The cleaning procedure was similar to that of the CdSe cores discussed above. Once the nanoparticles were isolated they were dissolved in hexane or ethylcyclohexane. This synthesis yields a small amount of self-nucleated ZnS particles that are difficult to separate from the core/shell particles.

**Characterization:** Particles were characterized using transmission electron microscopy in addition to absorption and fluorescence. Absorption was collected on a Agilent 8453 UV-vis, while fluorescence was performed on a Horiba Fluorolog. A FEI Tecnai $G^2$ S-Twin transmission electron microscope operating at 200 kV using a $LaB_6$ filament was used to image the nanocrystals.

## *3.3.2 High Pressure Experiments*

### 3.3.2.1 Diamond Anvil Cell

High pressure experiments were performed using a symmetric diamond anvil cell (DAC) from Princeton. Pressure was generated using diamonds with a 300 μm culet size. Spring steel gaskets were pre-indented to ~80 μm in thickness and drilled using an Oxford laser miller or an electrostatic drilling machine. Several grains of annealed ruby[44] or a small piece of gold foil[46] was placed in the gasket hole using a small needle prior to the sample for the purpose of measuring the pressure inside the DAC. The sample dissolved in ethylcylcohexane was then added and the DAC was sealed. Samples used for X-ray diffraction were necessarily of a higher concentration than those used for the optical experiments.

### 3.3.2.2 High Pressure X-Ray Diffraction Experiments

High pressure X-ray diffraction measurements were performed on beamline 12.2.2 at the Advanced Light Source at Lawrence Berkeley National Lab. The data was collected using an energy of 25 keV (0.4959 Å). Typical acquisition times for the nanoparticle sample ranged from 10-20 minutes per pressure, while those of the gold pressure calibrant were 1-2 minutes. The beam size for samples ranged from 20-40 μm by 20-40 μm. For the gold calibrant, the beam size was 10 μm by 10 μm. Data was collected in a transmission geometry using a MAR345 image plate. The detector distance and tilt were calibrated with a $LaB_6$ (NIST) standard. The resulting two-dimensional XRD images were integrated to one-dimensional powder patterns using FIT2D.[75]

### 3.3.2.3 High Pressure Absorption and Fluorescence Experiments

High pressure optical experiments were performed using a Zeiss Axiovert inverted microscope that was configured to perform absorbance and fluorescence spectroscopy. The microscope was equipped with a Lexel 95 $Ar^+$ laser, which was set to emit the 488 nm line for the sample and ruby excitation. The beamsize of the laser was about 5-10 μm. Absorption spectra were collected by using a 12V, 100W halogen lamp mounted above the DAC. A Nikon 20× objective with a working distance of 23 mm was used to focus inside the DAC. The light

transmitted (absorption) or emitted (fluorescence) by the sample was directed through a Acton SpectroPro 2300i spectrometer and collected on a Princeton Instruments Spec-10 liquid nitrogen cooled CCD.

### *3.3.3 Data Analysis*

The XRD peaks were fit to Pearson VII functions in Fityk.[76] The optical data was fit to Gaussians using OriginPro 8.0.

## 3.4 Results

The transmission electron micrographs of the synthesized particles are shown in Figure 3.1. As expected, the particle size distribution widens with increased shell thickness and the particle shape becomes less spherical due to defects introduced by the lattice mismatch. Analysis of the TEM images indicates that each successive injection caused the particles to grow by approximately a monolayer (ML) of ZnS. The shell thicknesses used in this study were 0.4 nm (~1 ML), 0.6 nm (~2 ML), and 1.1 nm (~3 ML). For all samples, the CdSe core size was kept consistent, while the shell thickness was changed.

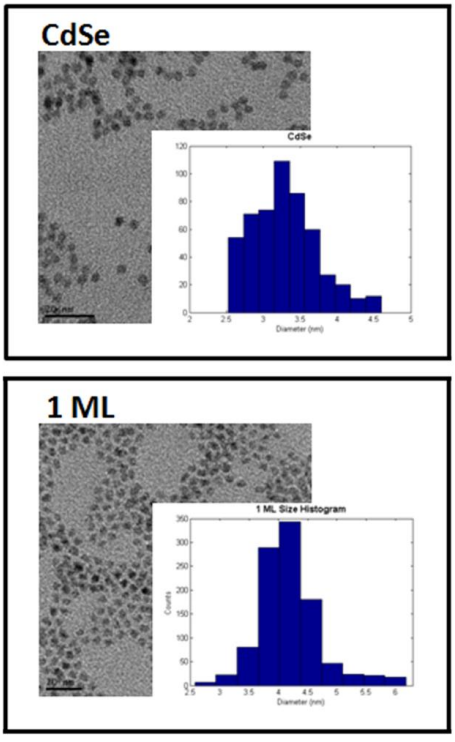


**Figure 3.1:** Examples of TEM micrographs for CdSe and CdSe/ZnS core/shell nanoparticles.

High pressure powder X-ray diffraction shows a clear transition from a 4-coordinate phase to a 6-coordinate rocksalt phase under pressure (Figure 3.2). Under ambient conditions, the diffraction pattern shows that the particles are a mixture of the wurtzite phase and the zinc blende phase due to the inclusion of stacking faults in the structure. As the pressure is increased, the intensity of lower angle wurtzite/zinc blende peaks (wurtzite (100), (002), and (101) and zinc blende (111)) decreases as the sample undergoes the phase transition. Simultaneously, the (200) peak intensity of the rocksalt phase increases. The majority of the scattering intensity in these powder patterns is due to the CdSe core, as the scattering coefficients for CdSe are significantly greater than those for ZnS. This means that we are unable to determine the crystalline phase of the ZnS before and after the phase transition in the CdSe occurs. The upstroke phase transition pressure of the CdSe is dependent on the thickness of the ZnS shell. The upstroke phase transition in the bare CdSe particles occurs at 6.1 GPa. Compared to a CdSe particle of the same size as the core, the phase transition for particles with a 1 ML shell is complete by 5.2 GPa, about 1 GPa below the bare CdSe particles. Nanocrystals with a 2 ML shell transform to the rocksalt phase at an upstroke pressure between that of the bare CdSe and the 1 ML shell. The two phases coexist briefly due to particle size heterogeneity and the different nucleation kinetics that exist on a particle by particle basis. The X-ray diffraction patterns for particles with even thicker shells were difficult to interpret because of the overlap of the CdSe peaks with the peaks from the thicker ZnS shell and a larger number of self-nucleated ZnS particles.

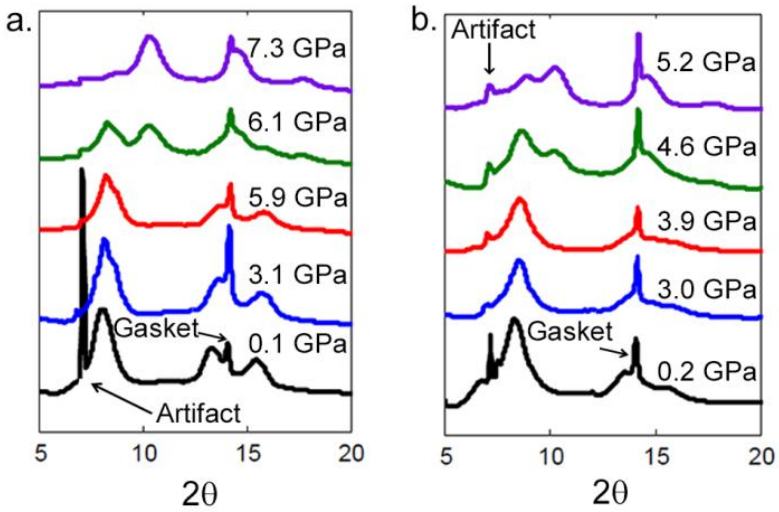


**Figure 3.2:** Selected XRD patterns for a.) CdSe nanoparticles and b.) CdSe/ZnS core/shell nanoparticles with one monolayer of ZnS.

From the XRD patterns, the unit cell volume at each pressure can be calculated, yielding hysteresis curves for each material (Figure 3.3). The stacking faults present in the low pressure phase cause shifting and broadening of the XRD peaks, leading to a higher error when calculating the volume of the structure. For the 2 ML sample, the pressure within the diamond anvil cell jumped upon the release of pressure jumped from 4 GPa to 2 GPa. From the optical experiments, the first appearance of the wurtzite/ zinc blende phase was observed at 2 GPa, indicating that the sample remained in the rocksalt phase at pressures above 2 GPa during the

downstroke. From this it can be assumed that the shape of the hysteresis curve for the 2 ML sample is similar to those of the bare CdSe and the 1 ML samples.

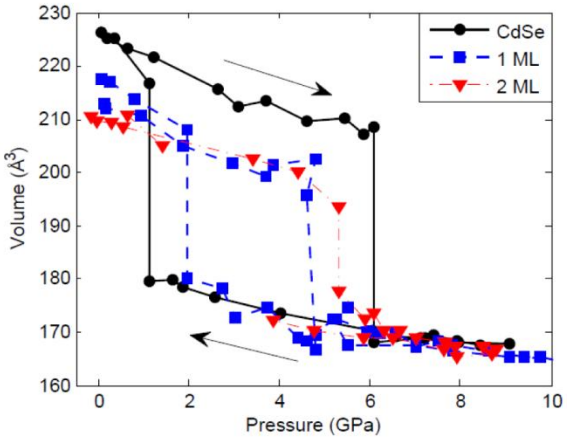


**Figure 3.3:** Pressure-volume hysteresis curves for the wurtzite/zinc blende phase to the rocksalt phase under high pressure for the CdSe control and the core/shell samples with one and two monolayers of ZnS.

In addition to the structural information obtained from the XRD data, optical data was also collected in the form of absorption and fluorescence spectra. The absorption patterns of all the samples show the expected blue shift with increasing pressure, with the eventual disappearance of the exciton due to the transition to the rocksalt phase, which has an indirect band gap. The fluorescence spectra of the bare CdSe particles under pressure also exhibit an overall blue shift with pressure in addition to some peak broadening. In contrast, the fluorescence spectra of the core/shell particles shows significant peak splitting with increased pressure (Figure 3.4). The fluorescence eventually disappears, indicating the transition to the high pressure indirect structure.

## 3.5 Discussion

Unlike previous studies investigating the phase transitions in CdSe/ZnS core/shell nanocrystals, this study shows a direct comparison to CdSe with no shell under identical conditions. This allows for differences in the pressure environment due to the hydrostaticity or non-hydrostaticity of the pressure transmitting medium to be removed from the analysis. Ethylcylcohexane is a quasi-hydrostatic pressure transmitting medium commonly used in diamond anvil cell experiments.[10] Because it is quasi-hydrostatic, some shear may be present in the diamond anvil cell.

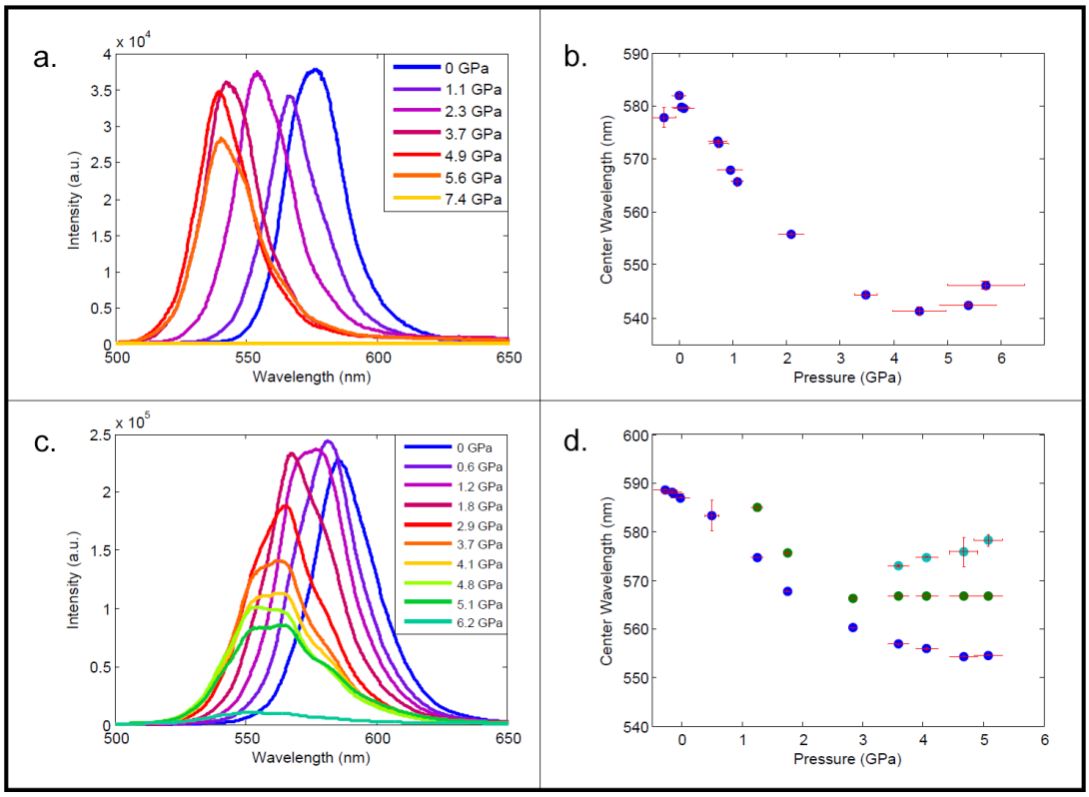


**Figure 3.4:** The fluorescence spectra of CdSe nanoparticles (a) and CdSe/ZnS nanoparticles with one monolayer of ZnS (c) with increasing pressure are shown. The corresponding peak positions for the CdSe nanoparticles (b) and the CdSe/ZnS core/shell nanoparticles (d) describe the observed peak splitting with increasing pressure.

From the hysteresis curve, it is obvious that the initial unit cell volume for nanoparticles with a ZnS shell is smaller than the bare CdSe nanoparticles. The ZnS shell has smaller lattice parameters than that of the CdSe core, causing it to compress the CdSe core. Previous simulations have indicated that this compression should be less than 1 GPa for a single monolayer of ZnS and about 1.5 GPa for a shell with a thickness on the order of two monolayers of ZnS.[70] Using the bulk modulus of CdSe nanoparticles in the wurtzite phase,[7] we calculated that the pressure felt by the core with one monolayer of ZnS was about 2 GPa. When taking into account the error introduced into the measurement due to the presence of stacking faults and the diffraction from a small number of pure ZnS nanoparticles, this is within error of the calculated pressure.

The upstroke phase transition pressure is clearly dependent on the shell thickness. The decrease in the phase transition pressure and the width of the hysteresis loop for the core/shell particles with one monolayer of ZnS can be attributed to a change in the nanoparticle surface. Previous simulations have indicated that during this phase transition the nucleation of the new phase occurs on the surface, meaning that the phase transition conditions could be altered if the surface was significantly changed.[60-61] The first monolayer of ZnS could restructure the surface such that nucleation of the new phase is easier. Once mismatch defects are induced due to a

shell thickness greater than the critical thickness, the structure may relax back to a structure resembling that of the bare core, causing the phase transition pressure to rise again. The upstroke phase transition in the particles with a shell thickness of two monolayers is greater than the observed conditions for a pure CdSe particle of a size similar to that of the core plus the shell, but about the same as a pure CdSe nanoparticle of the same size of just the core. In addition to the surface restructuring due to the addition of the ZnS shell, the shell also introduces a biaxial strain at the surface due to the lattice mismatch. This strain changes the pressure environment that the core experiences from quasihydrostatic to anisotropic, thus introducing a stronger shear into the system. The shear can also lower the observed phase transition pressure of the core/shell particles relative to bare CdSe particles.

The restructuring of the surface and the introduction of mismatch defects into the lattice of the core/shell nanocrystal provide sites for the nucleation of the new phase. This lowers the activation energy necessary to transition from one phase to the next, causing a reduction in the upstroke phase transition pressure and an increase in the downstroke phase transition pressure. This results in the shrinking of the width of the hysteresis curve when a ZnS shell is included in the nanostructure.

The thermodynamic phase transition pressure, as measured from the middle of the hysteresis curve, also shifts with the shell thickness. The initial decrease in the thermodynamic phase transition pressure can be attributed to the expitaxial nature of the first monolayer. The lattice mismatch between the CdSe core and the ZnS shell should result in a pressure being exerted on the core by the shell. This has been previously modeled by Grunwald et al.[70] The phase transition pressure in this case would then be the external pressure exerted in the diamond anvil cell plus the pressure exerted by the ZnS shell. For greater shell thicknesses, defects are introduced at the interface due to the shell thickness being greater than the critical thickness for the epitaxial growth of ZnS on CdSe. These mismatch defects relax the structure, reducing the pressure exerted on the core by shell. As a result, the phase transition to occur at a pressure closer to that of the bare core for shells thicker than 1 ML.

The optical properties of these core/shell semiconductor nanocrystals also differ from those of bare CdSe nanocrystals. The fluorescence of the bare CdSe remains approximately a single Gaussian peak throughout the pressure upstroke, with a small deviation before the phase transition. In contrast, the fluorescence of particles with a ZnS shell, regardless of shell thickness, split into multiple Gaussians peaks. Because the same splitting is not seen in the particles without a shell, it cannot be attributed solely to the pressure environment within the diamond anvil cell. Instead, the splitting of the fluorescence peak must be due, in part, to the presence of the shell. The lattice mismatch between the core and the shell creates a biaxial strain that changes the pressure environment that is felt by the core. This biaxial strain, in combination with the quasi-hydrostatic pressure environment, cause at least some of the nanoparticles to be compressed in an anisotropic manner.

Under uniaxial pressure, the symmetry of the crystal structure of the nanoparticles is broken. It was previously found for bulk II-VI semiconductors that the behavior of the band structure dependence depends not only on the direction and magnitude of the applied deformation, but also the spin exchange in the excitons.[77-78] Since the splitting of the valence

band is small, within $k_BT$, it is possible to observe radiative emission to all of the levels. This explains the observed splitting in the fluorescence of the core/shell particles. The fluorescence measurement is on an ensemble level, meaning there is a random orientation of particles relative to the polarization of the incoming laser light and presumably, a large distribution in the direction of applied pressure relative to the crystal axes. This makes the consideration of polarization and the direction of the applied uniaxial pressure unnecessary for our ensemble measurements.

It is of interest to consider these results in the broader context of studies of core-shell quantum dots. The present experiment shows evidence that the strong lattice mismatch between CdSe and ZnS results in a modification of the electronic energy levels of the core for thicknesses as small as one monolayer, and the introduction of defects in the shell for surprisingly thin shells that are just above a monolayer in thickness. The widespread practice of growing a graded shell of CdS to ZnS to relieve the strain makes sense in this context, and appears to be highly desirable if the structural integrity of the core-shell interface is important. The chemical and photochemical stability of a core-shell quantum dot can be comprised if the core/shell interface is defective, as appears to occur for ultra-thin layers of ZnS grown directly on CdSe.

## 3.6 Conclusions

This study shows that the phase transition in core/shell CdSe/ZnS nanoparticles is strongly dependent on the shell thickness, and that the dependence is not monotonic even for very thin shells. In addition, the study of the optical properties of these nanoparticles under high pressure showed a splitting of the fluorescence peak that can only be explained by the shell exerting an anisotropic force on the core. Future work may focus on how the degree of lattice mismatch can be used to tune the high pressure behavior of these nanoparticles in a wider range of core and shell compositions.

# Chapter 4

# Suppression of High Pressure Phase Transitions in Two-Dimensional Layered $Bi_2Se_3$ Nanocrystals

## 4.1 Abstract

Previous high-pressure studies in the layered chalcogenide, $Bi_2Se_3$, have revealed rich and unusual physics including a structural phase transition from a rhombohedral to monoclinic structure and an electronic topological transition. As a layered material, $Bi_2Se_3$ possesses a van der Waals gap which can serve as a host for intercalant guests, further altering the electronic and structural behavior of the material. Recently, a method to intercalate high densities, up to 60 atomic percent, of zero-valent copper into $Bi_2Se_3$ nanoribbons was developed. Using X-ray diffraction, the high-pressure structural behavior of $Bi_2Se_3$ nanoribbons and copper-intercalated $Bi_2Se_3$ nanoribbons was investigated using a diamond anvil cell and a synchrotron source. The nanoribbons of $Bi_2Se_3$ undergo a structural phase transition from a rhombohedral structure ($R\bar{3}m$) to a monoclinic ($C2/m$) phase at a higher phase transition pressure that that of the bulk material. The intercalation of copper into the gaps between the layers in the nanoribbons further raises the transition pressure and alters the electron topological transition.

## 4.2 Introduction

### *4.2.1 Topological Insulators*

Topological insulators are a newer class of materials with very interesting properties. Like normal insulators, topological insulators possess a band gap between the highest occupied electronic band and the lowest unoccupied electronic band. But unlike the ordinary insulators, the surface states (or edge states in the case of 2-D materials) of topological insulators do not exhibit this gap. Instead they provide a gapless series of states connecting the conduction and

valence bands. Such materials could find applications in device physics in addition to filling a gap in our understanding of band theory.

### *4.2.2 Bismuth Selenide and Copper Bismuth Selenide*

$Bi_2Se_3$ has attracted much interest as part of a new class of three-dimensional topological insulators. [79-81] This has spurred many investigations into controlling the synthesis, properties, and chemical behavior of this material. $Bi_2Se_3$ is a layered chalcogenide. Quintuple layers of alternating Se and Bi (Se-Bi-Se-Bi-Se) sheets form the two-dimensional layers found in the rhombohedral phase. These quintuple layers are separated from one another by a van der Waals gap. Because of their layered structure, two-dimensional layered materials, such as $Bi_2Se_3$, are easy to chemically modify through the accommodation of atoms in the van der Waals gap between the layers.

Recently, the ability to intercalate high densities of zero-valent metals, including copper, gold, silver, and cobalt, into layered $Bi_2Se_3$ nanoribbons has been achieved.[82-83] By tuning the type and concentration of the intercalated species, the electronic and structural properties of the material can be altered, giving rise to superconductivity or unique electronic states.[83-86] High pressure is a key tool in further achieving novel electronic and structural states.

Previous investigation of bulk $Bi_2Se_3$ have shown that there is a pressure induced structural phase transition from the rhombohedral ($R\bar{3}m$, space group 166) layered structure to a monoclinic ($C2/m$, space group 12) structure.[87] In bulk investigations, this structural phase transition commences around 8 GPa.[88] As the dimensionality of this material is reduced, fewer and fewer layers are incorporated into the structure, allowing surface effects to begin to dominate the structural phase behavior. Such size dependent behavior of phase transition has been previously observed in other materials.[7,11,89]

In addition to the structural phase transition, literature demonstrates the presence of an electronic topological transition (ETT) in $Bi_2Se_3$ under pressure.[87,90] An ETT is a second-order isostructural transition where the shape of the Fermi surface undergoes a transition. In these layered chalcogenide materials, this type of transition likely corresponds to a pressure where the van der Waals gap has been compressed almost entirely out of the crystal, leading to some type of overlap resulting in a change in the Fermi surface. Previous calculations have shown that without taking into account the surface states, $Bi_2Se_3$ is an indirect semiconductor at ambient pressure, with a conduction band minimum at the Γ point and the valence band maximum halfway between the Γ and U points.[91] At pressures above 5 GPa, the band gap becomes direct, with the gap halfway along the Γ-U direction.[91] While this change in the band structure has not been directly linked to the ETT, it could play a role in the shape change of the Fermi surface. Because the bulk band structure of $Bi_2Se_3$ has a gap at the Fermi energy, there is no Fermi surface until the surface states are included. Some of the surface states occupy the band gap, allowing for the calculation of a Fermi surface to be possible.[79-81] Such a transition does not exhibit a discontinuity in the unit cell volume upon undergoing the transition, but does exhibit a change in the compressibility. Previous high pressure experiments on $Bi_2Se_3$ and $Bi_2Te_3$ have shown that the rhombohedral phase shows a change in the compressibility as the pressure is

increased.[87,92-95] This has been found to be a reliable indication of an ETT in these layered chalcogenides.[90]

In this work, synchrotron X-ray diffraction experiments were conducted to investigate the high-pressure behavior of $Bi_2Se_3$ nanoribbons, with a focus on the pressure-induced phase transitions. The phase transition pressure of pure $Bi_2Se_3$ nanoribbons is compared with that of copper-intercalated $Bi_2Se_3$ nanoribbons (45 atomic percent of copper). It was found that the presence of copper in the lattice increases the structural phase transition pressure and affects the electronic topological transition.

## 4.3 Experimental

### *4.3.1 Synthesis*

$Bi_2Se_3$ nanoribbons (Figure 1; top) were prepared using a vapor-liquid-solid (VLS) growth method described elsewhere.[96] A source powder of $Bi_2Se_3$ was placed in a 1' tube furnace at 550°C. The carrier gas, argon, transports the sublimed powders to a colloidal gold coated quartz growth substrate downstream. A high density of zero-valent copper was intercalated into $Bi_2Se_3$ nanoribbons (Figure 1; bottom) using the method from References 82 and 83. Briefly, $Bi_2Se_3$ nanoribbons on the quartz growth substrate were placed into a solution of 0.01 g of tetrakisacetonitrile copper(I) hexaflourophosphate in acetone just below reflux (51°C) for four hours. The final concentration of intercalated copper in these samples was 45 atomic percent as determined by energy-dispersive X-ray spectroscopy (EDX) and X-ray photoelectron spectroscopy (XPS).[82-83]

### *4.3.2 Data Collection*

High pressure X-ray diffraction measurements were performed on Beamline 12.2.2 of the Advanced Light Source at Lawrence Berkeley National Lab using an energy of 25 keV (0.4959 Å). Typical acquisition times were 1-5 minutes per pressure data point. A spot size of 10 μm × 10 μm was used. Pressures were generated in a symmetric diamond anvil cell (DAC) with 300 μm culets. Spring steel gaskets were pre-indented to ~80 μm thickness and drilled using an Oxford laser miller. A 4:1 methanol:ethanol pressure transmitting medium was used, which is hydrostatic to about 10 GPa.[28] The sample was loaded by placing several nanoribbons in the gasket hole using a needle before the pressure-transmitting medium was added and the DAC sealed. Several grains of annealed ruby were also placed in the gasket hole in order to measure the pressure inside the DAC.[44] Ruby fluorescence was excited with a 488 nm $Ar^+$ laser. The degree of hydrostaticity was determined by the line width of the ruby fluorescence.[44]

### *4.3.3 Data Analysis*

The detector distance and tilt relative to the sample were calibrated with a LaB6 (NIST) standard. Two-dimensional XRD images were integrated to one-dimensional powder patterns using FIT2D.[75] Peaks were fit to Gaussians using Mathematica. The pressure-volume data was

fit to a Birch-Murnaghan equation of state using EosFit v5.2.[97] Atomic structures were visualized using Jmol.[98]

## 4.4 Results and Discussion

$Bi_2Se_3$ nanoribbons were synthesized via the vapor-liquid-solid method (see experimental). Zerovalent copper was intercalated into the van der Waals gap of the structure for one of the nanoribbon samples. No evidence of copper precipitates or particles was observed in the TEM or the XRD. Both structures were highly crystalline, as evidenced by the TEM images and electron diffraction shown in Figure 4.1.

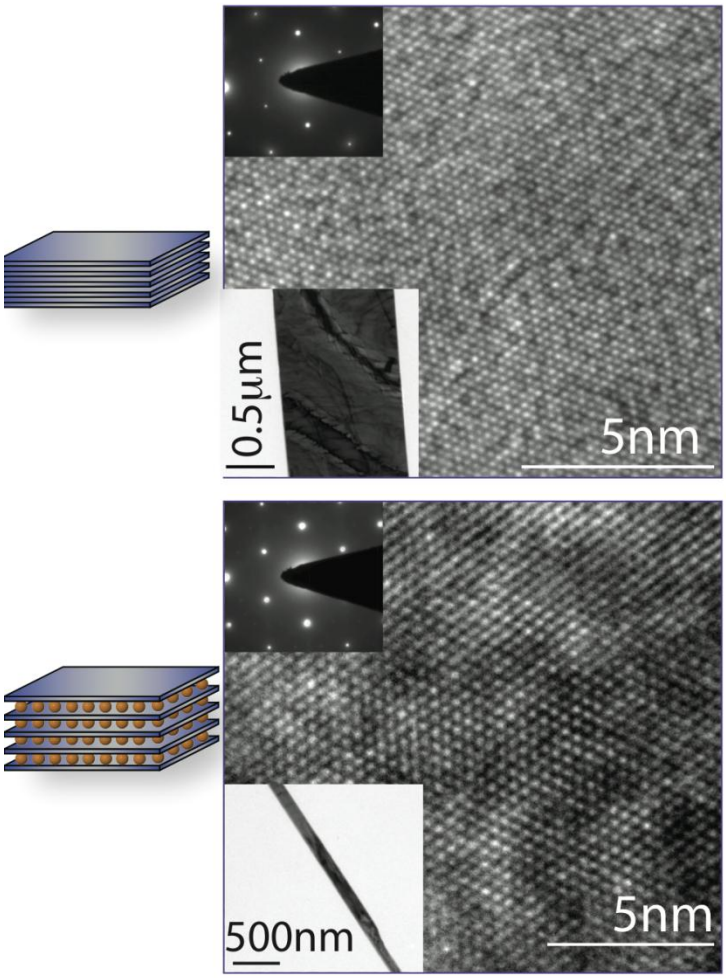


**Figure 4.1:** TEM images of nanoribbons (inset) of $Bi_2Se_3$ and copper intercalated $Bi_2Se_3$ used in this study. Electron diffraction (inset) and high resolution TEM images show these particles are highly crystalline.

High pressure X-ray diffraction of $Bi_2Se_3$ nanoribbons and copper-intercalated $Bi_2Se_3$ nanoribbons revealed markedly different phase transitions conditions (Figure 4.2; left and center). At pressures less than 10.3 GPa, the pure $Bi_2Se_3$ nanoribbons were in the rhombohedral phase (Figure 4.2). At 10.3 GPa, the nanoribbons were a mixture of the rhombohedral and monoclinic structural phases. The phase transition was complete after 12 GPa. This is significantly higher than the phase transition pressure in bulk $Bi_2Se_3$ which exhibited a phase transition that commenced at 8 GPa.[88] It is well known that crystallite size plays an important part in the phase transition pressure due to the role of surface effects.[7,89] Fewer layers are incorporated into the crystal as the crystal gets thinner. This allows the surface to begin to dominate the thermodynamics, changing the phase transition conditions.

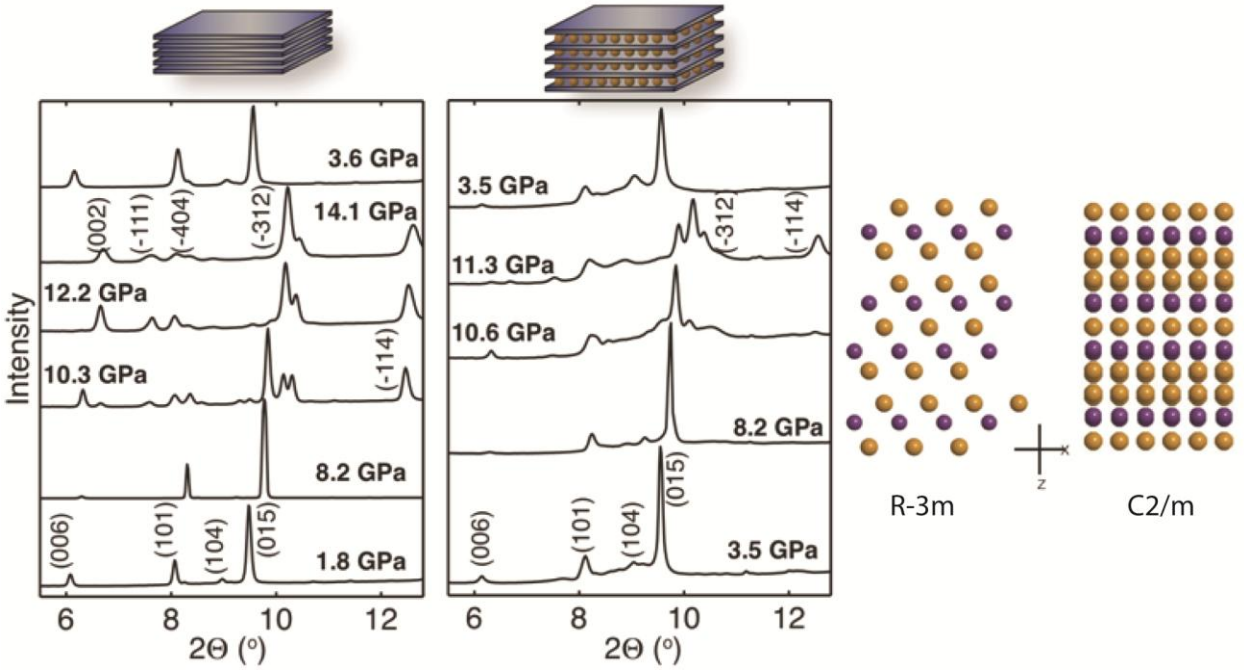


**Figure 4.2:** XRD patterns of $Bi_2Se_3$ nanoribbons (left) and nanoribbons intercalated with copper (center). $Bi_2Se_3$ undergoes a phase transition from a rhombohedral ($R\bar{3}m$) structure to a monoclinic (*C2/m*) (right). Purple atoms represent bismuth, while yellow atoms are selenium.

The structural phase transition from the rhombohedral phase to the monoclinic phase is driven by a collapse of the van der Waals gap between the layers. As the layers are forced closer together, their attraction becomes so strong that the material undergoes a phase transition. By inserting copper into the host lattice, it becomes more difficult to compress the gap due to a disruption of the van der Waals force between the quintuple layers, allowing for a higher phase transition pressure. The phase transition in the copper intercalated nanoribbons is not complete even at 12 GPa (Figure 4.2). In both samples, upon release of pressure the high pressure monoclinic phase transformed back to the ambient rhombohedral structure (Figure 4.2).

By fitting the XRD data, the lattice parameters of the low pressure rhombohedral phase were obtained. The change in the *a*-axis with pressure appears to be approximately linear, but that of the *c*-axis deviates from a line. In addition, the *c*-axis lattice parameter changes significantly more than that of the *a*-axis. The quintuple layers are stacked along the *c*-axis, allowing for significant compression of the gap between layers before the phase transition. As the gap collapses, the layers get closer together, making compression of the material along the *c*-axis more difficult, accounting for the deviation from linearity observed in Figure 4.3. In contrast, the layers are parallel to the *a*-axis. This does not allow the crystal to be compressed to the same extent along the *a*-axis as the *c*-axis due to the interatomic repulsion between nearest neighbor atoms within the layers.

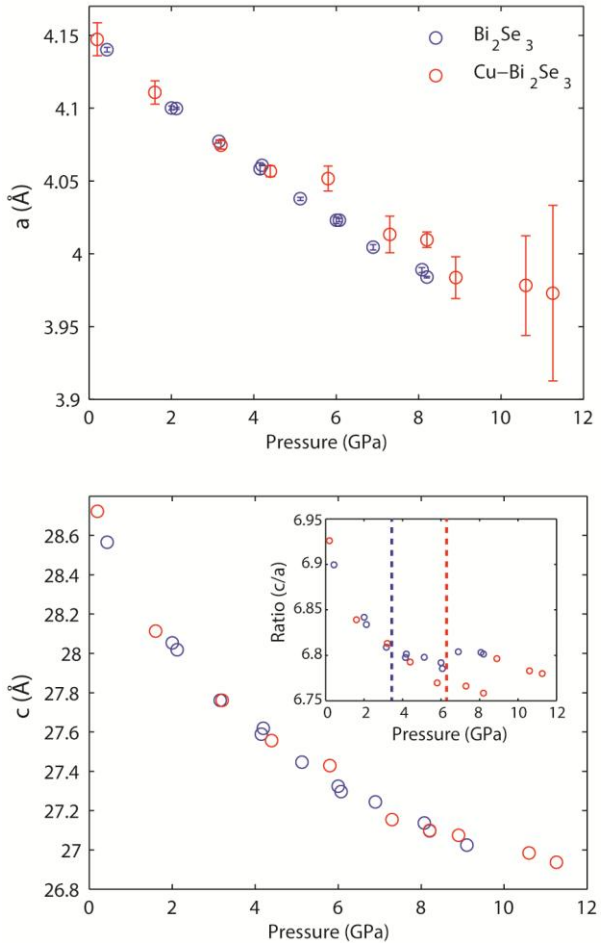


**Figure 4.3:** Lattice parameters for the *a*- and *c*-axes, as a function of pressure for $Bi_2Se_3$ (blue circles) and Cu-$Bi_2Se_3$ (red circles) are shown. The inset plot shows the c/a ratio.

A dramatic change in the slope of the c/a ratio versus pressure was also observed (Figure 4.3; inset). Such a change has been previously observed in bulk $Bi_2Se_3$ and has been found to be indicative of an ETT.[87,90] For the copper intercalated nanoribbon sample, the change in slope of

the c/a ratio is not observed until after 6 GPa, pronouncedly higher than the sample without copper, where the change in slope occurs at about 3 GPa. This is due to the copper atoms disrupting the van der Waals force between the layers. Doping the structure with copper also changes the Fermi level in the $Bi_2Se_3$, providing the potential for a change in the initial shape of the Fermi surface, which would then change in a different manner at high pressure. This changes the conditions under which the ETT occurs.

Figure 4.4 shows the change in the volume of the rhombohedral and monoclinic phases. The pressure-volume data was fit to a third-order Birch-Murnaghan equation of state.[99] For the $Bi_2Se_3$ nanoribbons, the following parameters were determined: $V_0$=142.9(4) Å$^3$, $B_0$=35(3) GPa, and $B_0'$=7. For the Cu-$Bi_2Se_3$ nanoribbons, the error of the fit was higher, yielding $V_0$=143(3) Å$^3$, $B_0$=27(16) GPa, and $B_0'$=14(10). For both these samples, the calculated bulk modulus agreed within error with that reported in Reference 90. Upon undergoing the ETT, there is no discontinuous change in the volume (Figure 4.4). This is expected, as the ETT is a second-order transition. The structural phase transition from the rhombohedral phase to the monoclinic phase exhibits a discontinuous change in volume, indicating a first order transition. These results agree with previous investigations of the phase transition in bulk $Bi_2Se_3$.[87,90]

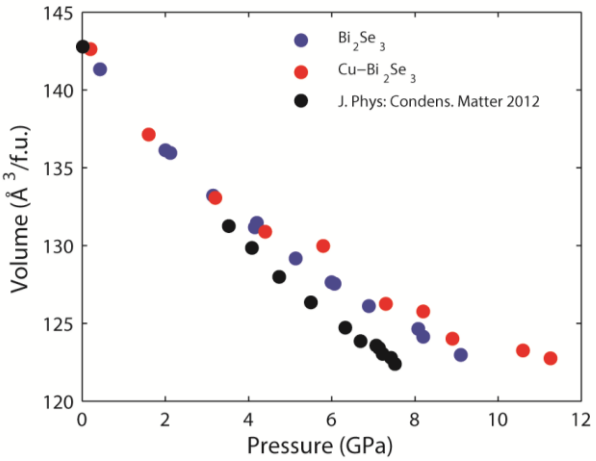


**Figure 4.4:** The volume of the unit cell with pressure.

## 4.5 Conclusions

This work presents the ability to tune the phase transition pressure in two dimensional layered nanostructures, such as $Bi_2Se_3$, through the intercalation of a metal into the van der Waals gap. In addition to an overall higher phase transition due to the crystallite size, the intercalated metal disrupts the forces between the layers leading to a higher phase transition pressure. Future studies should look at the dependence of the phase transition pressure on the percent intercalation of the metal and if there is a dependence of the metal used.

# Chapter 5

# Ultrafast Observations of Structural Phase Transition Pathways in Nanocrystals Using a X-Ray Probe

## 5.1 Abstract

The ability to perform X-ray diffraction on a femtosecond timescale using the free electron laser at the Linear Coherent Light Source has allowed for the investigation of the mechanism of the wurtzite to rocksalt structural phase transition in cadmium selenide nanocrystals under shock compression. Under shock compression, the phase transition occurs at pressures lower than those under hydrostatic compression due to the presence of shear. At low shock stress, the presence of a *h*-MgO type intermediate was confirmed in accordance with simulation. Higher shock stress experiments showed a direct conversion of the wurtzite phase to the rocksalt phase, completely bypassing the intermediate phase.

## 5.2 Introduction

The study of nanomaterials under high pressure has provided important insight into the interplay of thermodynamics and kinetics of the observed structural phase transitions. Nanocrystals represent a size domain of matter where defects cannot typically be supported and where the surface begins to play an important role.[7,11,36] These factors yield a size dependence of the phase transition pressure and a broadening of the hysteresis curve for the wurtzite to rocksalt phase transition in cadmium selenide nanocrystals.[6-8] It is important to note that these experiments were performed in a hydrostatic environment inside diamond anvil cell.

Little has been done to investigate the phase transition of II-VI nanocrystals under uniaxial pressure conditions, an example of which is a shock wave.[48] A shock wave is a transient uniaxial pressure wave that travels through a material. Previous experiments using shock waves found that cadmium selenide behaves differently under shock compression when compared to experiments performed under hydrostatic experiments. Under shock compression,

cadmium selenide nanocrystals have completely transformed to the rocksalt phase by around 3 GPa.[100] This is significantly lower than the upstroke transformation pressures observed with similar samples in a diamond anvil cell. The transformation rate also increases under shock compression due to the shear stress introduced by the shock wave. The speed of this transformation suggests that multiple nucleation sites can be introduced within a single nanocrystal.[100]

Recent simulations also provide insight into the nature of the wurztite to rocksalt structural phase transition in II-VI semiconductors. By using transition path sampling and molecular dynamics, a possible structure of the transition state was proposed.[101-103] This 5-coordinate *h*-MgO type structure was only found to be prevalent in faceted nanorystals (Figure 5.1).[101] This is a result of compression along the *c*-axis of the wurtzite structure to yield the *h*-MgO phase. The rock salt phase is then achieved from a shear along the *a*-axis.[101] While this transition state is theoretically possible, it had previously not been experimentally observed due to experimental difficulties with measuring the structural properties of a material at the temporal resolution required to observe the transition state.

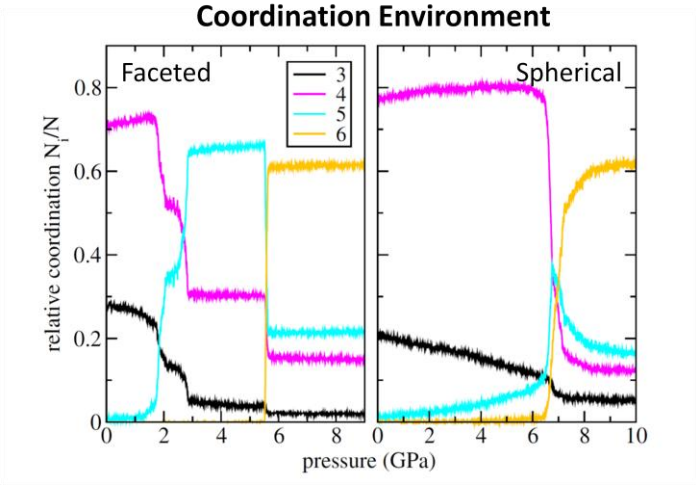


**Figure 5.1:** The theoretical coordination environment in a CdSe nanocrystal under high pressure. The 5-coordinate *h*-MgO is only observed with a high probability in faceted nanocrystals. (Figure from reference 101).

With the advent of free electron lasers, such as the Linear Coherent Lightsource (LCLS), the investigation of the transition state of the wurtzite to rocksalt phase transition can finally be investigated in II-VI nanocrystals under shock compression. Using cadmium sulfide nanospheres and nanorods, the structural phase transition pathway under shock compression was investigated using the ultrafast X-ray pulses of the LCLS as a direct probe of the structure.

## 5.3 Experimental

### *5.3.1 Nanoparticle Synthesis*

Cadmium sulfide nanodots and nanorods were prepared according to Reference 21.

**Reagents:** Trioctylphosphine oxide (TOPO, 98%), trioctylphosphine (TOP, 98%), and tributylphosphine (TBP, 98%) were purchased from STREM. Octadecylphosphonic acid (ODPA) was purchased from PCI Synthesis. Cadmium oxide (99.998%) was obtained from Alfa Aesar. Hexamethyldisilathiane ($(TMS)_2S$) was purchased from Fluka. Solvents including toluene, methanol, acetone, and hexanes were purchased from Sigma-Aldrich. Hexylphosphonic acid (HPA, 95%) and sulfur (S, 99.99%, sublimed) were also purchased from Sigma-Aldrich. Caution: $(TMS)_2S$ is a highly odorous compound and should be handled with care. TBP is slightly pyrophoric and should be handled using proper air free techniques.

**CdS dots:** In a 50 mL 3-neck round bottom flask equipped with a condenser, thermocouple adapter, stir bar, and septum, 3.299 g of TOPO, 0.603 g of ODPA, and 0.1 g of CdO were combined. The flask was placed under vacuum and heated to 150 °C for 1 hour. The flask was then backfilled with argon and heated to 300 °C, until a clear and colorless solution was formed. In a separate vial, 0.170 g of $(TMS)_2S$ and 3 g of TBP were combined inside a glovebox. The reaction mixture was heated to 320 °C and allowed to stabilize. Then, the $(TMS)_2S$ and TBP solution was quickly injected into the reaction mixture using standard air free handling techniques. The temperature was then set at 250 °C and allowed to grow for 7 minutes after the injection. The reaction mixture was cooled to about 70 °C where about 7 mL of toluene was injected. After cooling to room temperature, the solution was transferred to a vial and brought into a glovebox for cleaning. A solution of clean particles in toluene was achieved through repetitive precipitation of the particles with methanol or acetone combined with centrifugation and redissolution in toluene or hexanes.

**CdS seed solution:** The solution concentration was determined through UV-vis, using the equation for the absorption coefficient given in Reference 74. Once the concentration of the resulting CdS nanoparticle solution was determined, a 400 μM solution of CdS dots in TOP was made. The appropriate amount of CdS dots was precipitated with MeOH and centrifuged. The resulting pellet was dissolved in TOP to give a 400 μM solution.

**CdS nanorods:** Several hours before the reaction was performed, 0.120 g S and 1.5 g TOP were combined and allowed to stir in a glovebox to form TOP-S. In a 50 mL 3-neck round bottom flask equipped with a condenser, thermocouple adapter, stir bar, and septum, 3 g of TOPO, 0.290 g ODPA, 0.080 g HPA, and 0.086 g of CdO were combined. The reaction mixture was degassed at 150 °C for 1 hour. The reaction was then back filled with argon and heated to 350 °C. At 350 °C, 1.5 g of TOP was injected quickly, after which the temperature dropped. In a separate vial, the TOP-S solution made earlier and 200 μL of the CdS seed solution were combined. The resulting solution was quickly injected into the reaction mixture once the temperature had recovered to 350 °C. The reaction was allowed to proceed for 7 minutes after the injection. It was then cooled to room temperature. About 7 mL of toluene was added to prevent

solidification. The reaction was cleaned by repeated precipitation with MeOH, centifugation, and redissolution in toluene.

The size of the nanoparticles could be controlled by changing various parameters, including the injection temperature, the amount of cadmium oxide, and the amount of sulfur, as per Reference 21.

Particles were characterized using X-ray diffraction and transmission electron microscopy in addition to absorption and fluorescence. X-ray diffraction was performed on a Bruker AXS D8 Gadds instrument with a Co Kα source. Absorption was collected on a Agilent 8453 UV-vis, while fluorescence was performed on a Horiba Fluorolog. A FEI Tecnai $G^2$ S-Twin transmission electron microscope operating at 200 kV using a $LaB_6$ filament was used to image the nanocrystals. Micrographs of the nanodots and nanorods are shown in Figure 5.2.

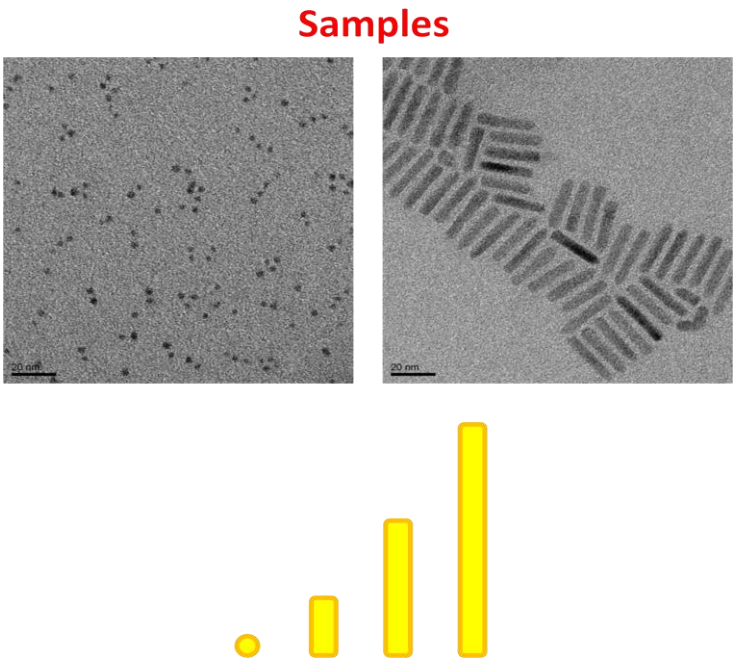


**Figure 5.2:** Transmission electron micrographs of cadmium sulfide dots and rods.

## *5.3.2 Substrate Preparation*

Shock wave generation was performed through the rapid ablation of a thin aluminum layer based on the literature.[51-52] The shock substrate consisted of a silicon wafer with a thin silicon nitride (2 μm thick) window. The silicon was etched to give direct access to the silicon nitride windows. On top of this, a 250 nm layer of aluminum was vapor deposited. Polyvinylalcohol (PVA, 1 μm thick ±5%) was spin cast from an aqueous solution to act as a buffer layer. The polymer was cured at 125 °C for 20 minutes. A toluene solution of nanocrystals was drop cast on top of the polymer to create a 250 nm layer of sample. A back

layer of 2 µm thick PVA was spin-casted on top of the sample to provide confinement of layers. The entire target was cured again at 125 °C for 30 minutes. The final cross section of the sample target is shown in Figure 5.3. Each silicon nitride window was destroyed by the shock inducing laser pulse, requiring the sample to be translated to a new window for each shot.

### *5.3.3 Linac Coherent Light Source (LCLS)*

Experiments were performed at the Linac Coherent Light Source at the SLAC National Accelerator Laboratory in the X-ray Pump Probe (XPP) hutch. Hard X-ray scattering in a collinear, transmission geometry using an X-ray energy of 9.5 keV (1.305 Å) and a 70 fs FWHM pulse width focused to a 50 µm diameter spot size was used. A Mar detector was used to collect the diffraction patterns before and after shock compression. The shock waves were initiated by a laser pulse with a central wavelength of 800 nm, stretched to 1 ps FWHM in time. The laser beam was focused to a 250 µm spot size.

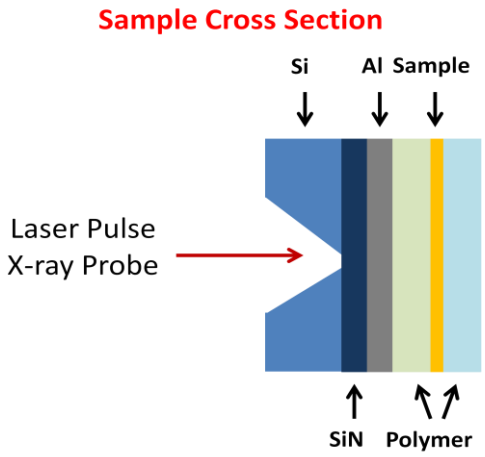


**Figure 5.3:** A schematic of the sample target cross section showing the various layers.

### *5.3.4 Pressure Determination and Analysis*

The shock stress induced by a particular laser power was determined by using the X-ray diffraction pattern from the aluminum and the cadmium sulfide. From the shifts of the diffraction peaks relative to their ambient positions, the shock stress could be determined. The images were integrated and analyzed using Matlab. Diffraction patterns were plotted in Q-space, where Q is defined by:

$$Q = \frac{4\pi \sin\theta}{\lambda} \tag{5.1}$$

Rietveld refinement was performed using Maud.[56]

Time zero for these experiments was determined from the coincident arrival of the laser pulse and the X-ray pulse at a reference sample. It was found to approximately correspond to the appearance of the compression in the aluminum laser.

## 5.4 Results

Shock waves induced by laser ablation of a thin metal foil were used to explore the high pressure behavior of cadmium sulfide nanocrystals. The resulting diffraction images indicate that a transition from the 4-coordinate wurtzite phase to the 6-coordinate rocksalt phase does occur under these conditions (Figure 5.4). Figure 5.4 shows the phase transition for 5 nm by 40 nm nanorods before shock and 300 ps after compression. The (200) peak of rocksalt can be clearly seen to grow in after compression. These images were radially integrated to provide a standard powder pattern, examples of which are seen in Figure 5.5.

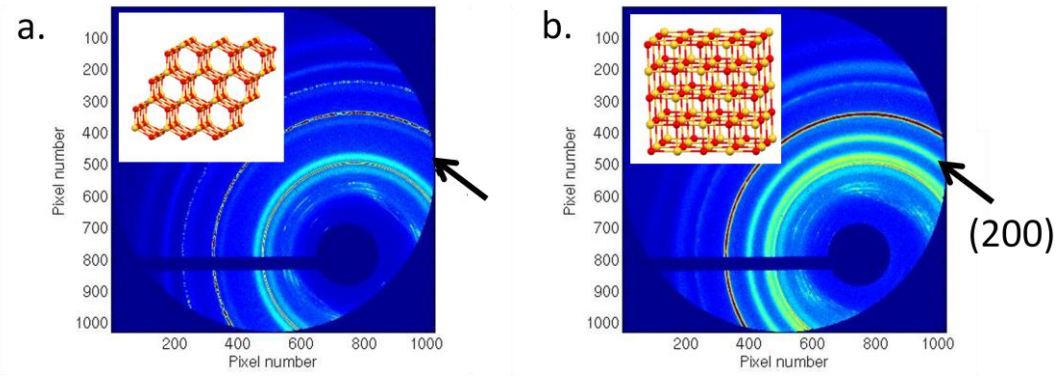


**Figure 5.4:** a.) Image of the X-ray diffraction under ambient conditions indicating that the particles are in the wurtzite phase. b.) Image of the X-ray diffraction 300 ps after shock compression. The position of the rocksalt (200) peak indicated by an arrow. Insets show the crystal structures for each diffraction pattern.

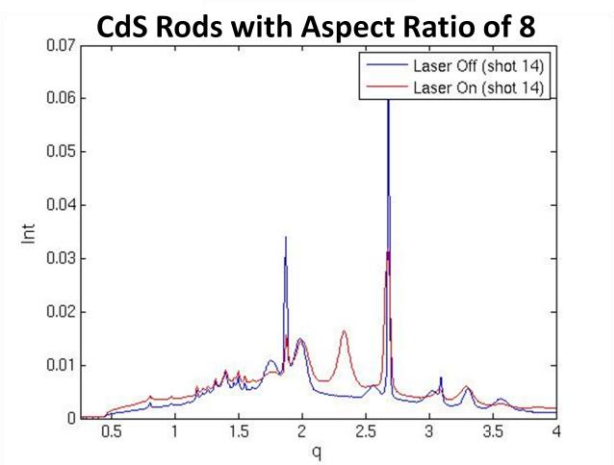


**Figure 5.5:** An example of the radially integrated powder patterns for CdS rods before and after shock compression.

Picosecond time resolution of the structural phase transition was achieved. Because a new sample window must be used for each time point, the diffraction after shock compression was normalized to that before compression to account for window to window variability. The integrated powder patterns of a 5 nm by 40 nm cadmium sulfide nanorod sample with time are shown in Figure 5.6 for two different shock stresses. The intense peak at Q=2.68 $Å^{-1}$ seen in both the 7.9 GPa and 9.1 GPa shock stress time traces is due to the aluminum (111) diffraction peak. The aluminum peak shifts to higher Q for a period between about 150 ps to about 200 ps. This is caused by the compression of the aluminum due to the initiation of the shock wave by the laser. The shock wave then propagates through the layers following the aluminum. After approximately a 50 ps time delay, the (200) peak of the cadmium sulfide rocksalt structure appears at Q=2.3 $Å^{-1}$ and it grows more intense with time. As the rocksalt (200) peak grows in, the wurtzite (100) peak at 1.76 $Å^{-1}$ decreases indicating the transformation from one phase to the next. The wurtzite (101) at Q=1.98 $Å^{-1}$ is replaced with the rocksalt (111) peak at approximately the same position yielding little intensity change in this region. The higher Q peaks (higher scattering angle) of the wurtzite phase corresponding to the (110), (103), and (112) peaks also decrease in intensity with time. Similar behavior was observed for other sample sizes and aspect ratios.

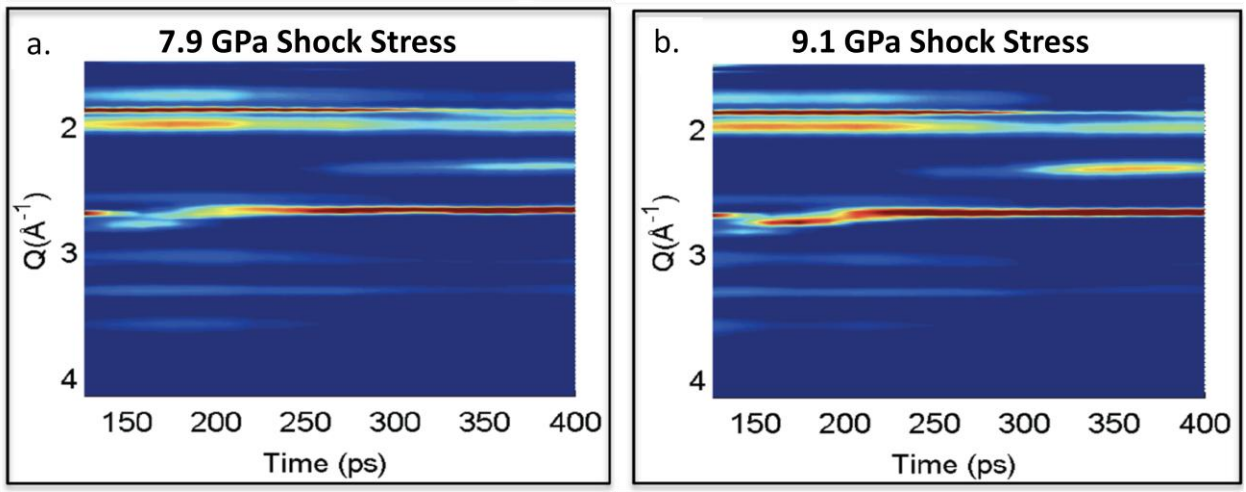


**Figure 5.6:** Q-dependent scattering as a function of the time delay for 5 nm by 40 nm cadmium sulfide nanorods: a.) for a 7.9 GPa shock stress. b.) for a 9.1 GPa shock stress.

The stress induced by a shock wave was measured by the compression of the aluminum layer, as evidenced by the shift of the aluminum (111) peak to higher Q values and from the peak positions of the rock salt phase relative to ambient. An example of the compression of the aluminum layer with time is shown as the black trace in Figure 5.7. Pressure increases sharply around 130 ps and then decreases as the shock propagates away from the aluminum layer and into the polymer and sample layers.

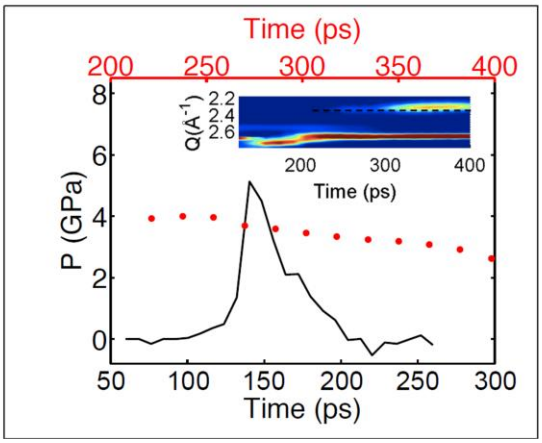


**Figure 5.7:** The compression of the aluminum with the time delay is shown in the black trace. The compression of the cadmium sulfide rocksalt phase is shown in red with the corresponding time axis on the top. The inset shows the corresponding shifts in Q-space with time.

The diffraction patterns also indicate that the rocksalt phase never relaxes to its ambient volume in the time frame investigated (Figure 5.7, red trace). The compression of the rocksalt phase yields a pressure similar to that of the aluminum layer at earlier times, but decays more slowly.

Shock stress dependent saturation of the rocksalt phase is observed (Figure 5.8). At pressures less than 4.1 GPa, no conversion to rocksalt is observed. At pressures 6.6 GPa and higher, the transition to the rock salt phase was observed with the conversion to the new phaseincreasing with shock stress. At stresses 9.1 GPa and higher, the maximum amount extent of transformation is reached and saturation behavior is observed.

The diffraction peak position over time provides important insights into the compression of the material. For instance, at low shock stresses (4.1 GPa), the wurtzite (002) peak shifts to higher Q, but the wurtzite (100) peak does not shift at all (Figure 5.9a). This shift develops first as a higher Q shoulder at early times, whereas a single (002) is observed at later times. The appearance of the shoulder indicates that the shock wave at this time delay is still in the process of traversing through the sample layer. This implies that part of the sample has been subjected to a stress while the other part is still ahead of the shock front. The (101) peak of the wurtzite phase also shifts to higher Q, but to a lesser extent. This indicates aniostopic compression along the *c*-axis. A shock stress of 4.1 GPa was not strong enough to generate the rock salt phase. At higher stresses, different behavior is observed (Figure 5.9b). Higher shock stress induced a decrease in the intensity of the diffraction peaks, but no corresponding shift to higher Q. This decrease corresponds directly to the growth of the rocksalt phase, indicating that the wurtzite phase directly converts to the rocksalt phase.

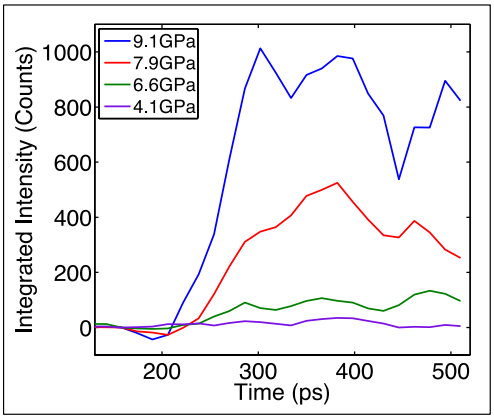


**Figure 5.8:** The integrated intensity of the (200) peak of the rocksalt phase versus the time delay.

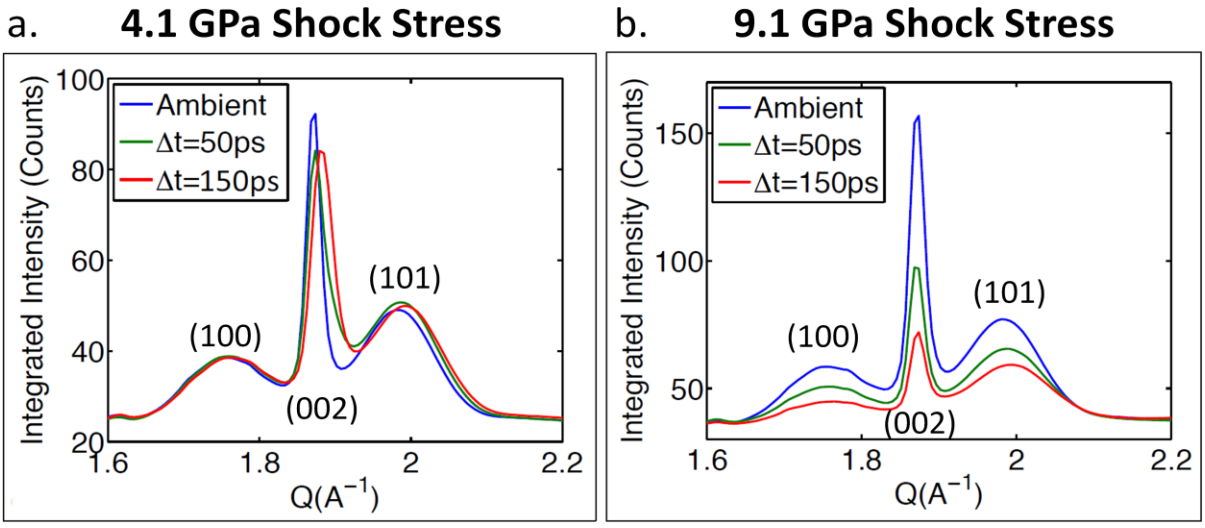


**Figure 5.9:** Change in the peak shapes and positions at different time delays for a.) a relatively low shock stress of 4.1 GPa and b.) a higher shock stress of 9.1 GPa.

X-ray diffraction patterns were collected on an ensemble of nanoparticles. This allows for multiple structural phases to be present in the sample at any one time delay due to the shock wave width in time and the thickness of the sample layer. Rietveld refinement allows for the quantitative determination of the phases present in a diffraction pattern. When Rietveld refinement was performed on the diffractographs, in addition to the aluminum phase and the wurtzite and rocksalt phases of the cadmium sulfide, a second hexagonal component was found to be present. This was found to correspond to the 5-coordinate *h*-MgO structure ($P6_3/mmc$). An example of this at 7.9 GPa is shown in Figure 5.10. At no point in the phase evolution of these particles is the *h*-MgO phase the majority phase present.

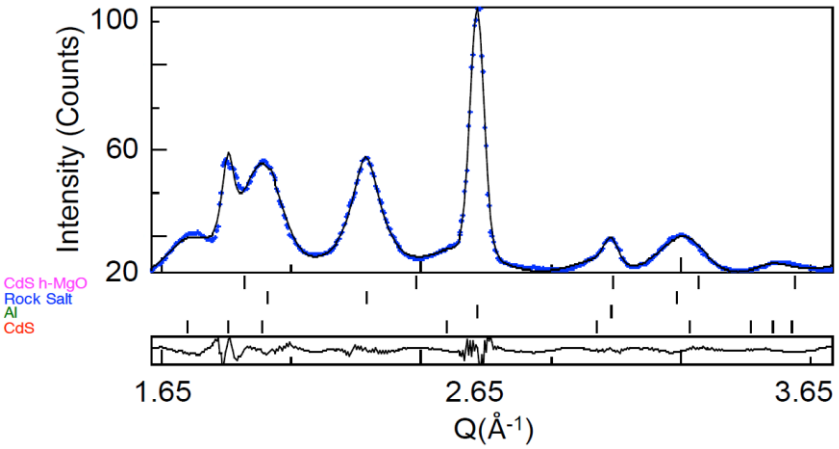


**Figure 5.10:** Rietveld refinement (black) of cadmium sulfide nanorods under a 7.9 GPa shock stress, 60 ps after the shock arrival (blue). Four phases were included in the refinement: wurtzite CdS, rocksalt CdS, *h*-MgO CdS, and cubic aluminum. The bottom plot shows the residuals.

## 5.5 Discussion

The timescale for the transformation of these nanoparticles from the wurtzite to the rocksalt phase is consistent with that predicted by simulations.[61] A 4 nm nanodot should transform in 7-10 ps, while the 5 nm by 40 nm nanorods investigated should transform in 40-80 ps according to simulations. The time range for the transformation of the nanorods depends where nucleation happens along the rod and the number of nucleation events in a single rod. A shock wave travelling at 5 nm/ps should traverse the entire sample layer (250 nm) in about 50 ps. This will convolute the experimentally determined transformation time making an exact timescale for the conversion to rocksalt in an individual particle impossible to calculate, although it can be said that the timescale observed for transformation is consistent with the theory.

The phase transition from wurtzite to rocksalt under shock compression happens at pressures lower than the same transition under hydrostatic pressure conditions (Figure 5.8).[6-8] This is a commonly observed trend in materials and is attributed to shear forces that are present in a shock wave.[50] Interestingly, the rocksalt phase produced by shock compression has a volume smaller than that under ambient conditions, indicating that it is compressed (Figure 5.7). The rocksalt phase also persists for the timeframe of the measurement (8 ns); it does not transform back to the wurtzite phase, but the lattice parameters do relax slowly (Figure 5.11). This is thought to occur due to this phase transition having a very wide hysteresis curve for nanocrystals, making the existence of the rocksalt phase at pressures well below the thermodynamic phase transition pressure possible.[6-8] The rocksalt particles are kinetically trapped until the barrier to the nucleation of the wurtzite phase can be overcome.[33] Larger nanoparticles have been shown to be metastable in the rocksalt phase at ambient pressures.[8]

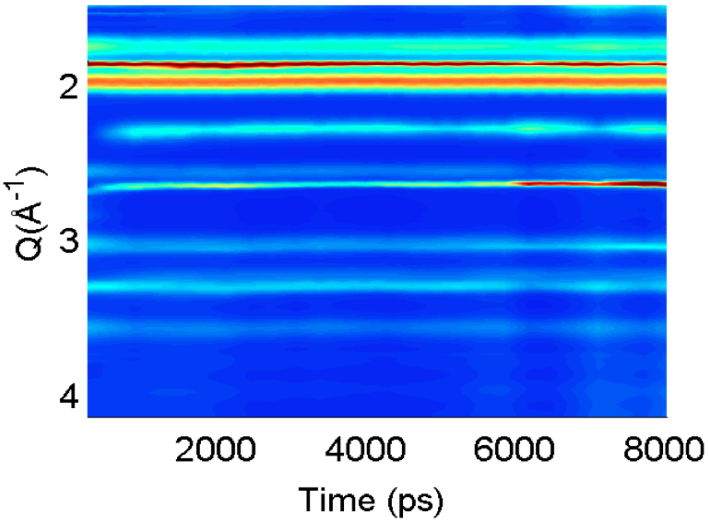


**Figure 5.11:** Time trace of the XRD pattern over long times. Evidence of the rock salt phase is seen even for the longest time measured (8 ns).

The change in the peak shapes and positions under shock compression provides insight into the mechanism of the phase transition. The preferential compression along the *c*-axis that is observed under low shock stress (Figure 5.9a) points towards the transition mechanism proposed by recent simulations.[101] This corresponds to the first step in the transformation of the wurtzite nanoparticles to the *h*-MgO type intermediate crystal structure (Figure 5.12). The 4.1 GPa shock stress shown in Figure 5.9 is too weak to yield the full transformation to rocksalt. Instead, the peaks return to their original shape and positions, indicating that this compression provides a low energy pathway to an unstable intermediate structure. The Rietveld refinement confirms the existence of the *h*-MgO type structure as an intermediate for the wurtzite to rock salt phase transition (Figure 5.10).

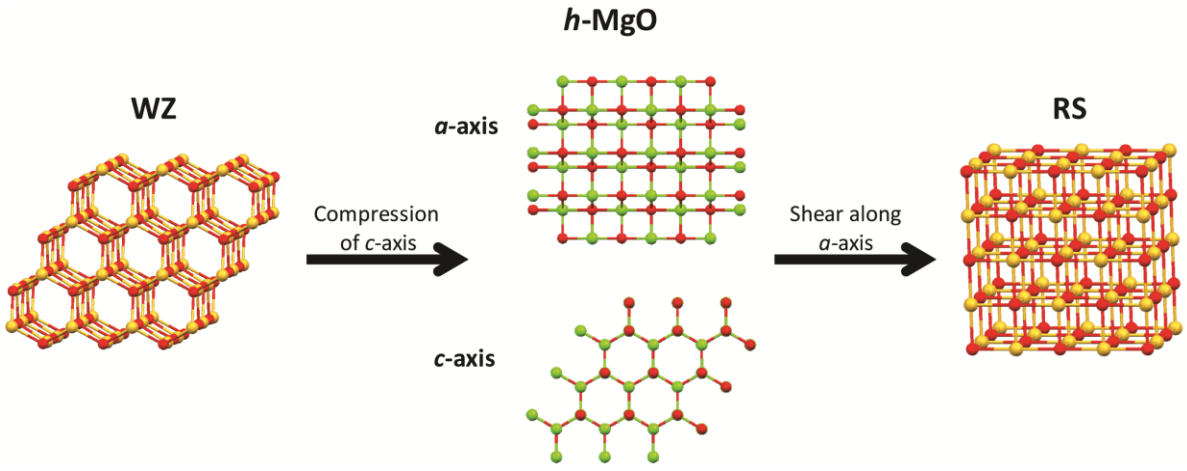


**Figure 5.12:** Schematic of one of the transformation mechanisms available to nanocrystals under shock compression.

Given the speed of the shock wave through the material (approximately 5 nm/ps) and assuming a single nucleation event per nanocrystal, part of the sample should be in the process of transforming while it was still being probed. While the Rietveld refinement confirms that some of the particles in the ensemble have a *h*-MgO structure, it also indicates this phase never becomes the majority constituent. This opens the door for an additional mechanism that occurs concurrently with the *h*-MgO intermediate that directly transforms the wurtzite to the rocksalt phase. This is supported by the absence of the preferred compression along the *c*-axis at higher shock pressures (Figure 5.9b). The absence of the intermediate also indicates that the activation energy for the transformation has been reduced under high shock stress allowing for the direct conversion from one phase to the next at a faster rate than those observed under hydrostatic conditions. This direct pathway has been suggested to occur for particles that have a disordered surface;[101] well faceted particles are thought to undergo the transformation through the intermediate phase.[101] The rapid increase in pressure and the uniaxial nature of the stress in shock waves may cause a disruption of the surface of the nanocrystals, leading to the direct pathway to be preferred at higher shock stress.

## 5.6 Conclusions

For the first time, the *h*-MgO type intermediate structure of the wurtzite to rocksalt phase transition in cadmium sulfide has been observed. This provides the first experimental evidence supporting the theoretical intermediate phase. In addition, while this phase is present, it does not represent the only pathway available for the structural phase transformation under shock compression. A direct pathway from the wurtzite to the rocksalt phase also exists at high shock stress. The shear component of the shock wave catalyzes the phase transition, allowing it to occur at stresses significantly lower than those observed under hydrostatic pressure conditions. The reduction of the over-pressurization needed for the phase transition to occur indicates a decrease in the height of the activation barrier. The rapid nature of shock compression and the introduction of shear into the system open the door for investigating not only the mechanism of these structural phase transitions, but also the possible discovery of new structural phases in nanomaterials.

# Chapter 6

# Towards Single Particle Fluorescence Measurements at High Pressure

## 6.1 Abstract

To date, high pressure experiments involving nanocrystals have only been performed on an ensemble level. Typically, each particle is slightly different from the others, in terms of the exact number of atoms, surface passivation, and faceting. This convolutes what is actually going on in the sample on a particle by particle basis. The ability to investigate the phase transition in II-VI semiconductor nanocrystals on a single particle level would provide important insight into the high pressure behavior of materials before the phase transitions, at the thermodyanamic phase transition pressure, and after the phase transition. The question regarding the number of times a particle attempts to transform before it actually does could be answered, and the kinetics of the phase transition could be determined. Unfortunately, the ability to image single particles within a high pressure apparatus is not yet available. There are several optical challenges that must be overcome before such an experiment can be realized.

## 6.2 Introduction

The investigation of matter at the single molecule or single nanoparticle level has led to a greater understanding of the fundamental processes governing chemistry on a molecule by molecule basis. While the size of single molecules and nanoparticles is well below the diffraction limit, making direct optical imaging impossible, the light given off by the molecule or nanoparticle can be imaged. Recently, single particle experiments have shown that the fluorescence from individual nanoparticles is not constant[105] and that Kasha's rule can be broken.[106] Also, the heterogeneity of various chemical reactions on the surface of the nanocrystals has been shown.[107] If single particle techniques can be applied to nanoparticles under high pressure, a door would be opened to investigate the effect of pressure on a number of different phenomenon, including fluorescence blinking and spectral drift. This could be extended to explain the nature of the fluorescence splitting in core/shell nanocrystals under high

pressure, as it is not known if this is an ensemble effect or if each particle is emitting a number of different states that average to the observe fluorescence spectrum. In addition, the nature of a structural phase transition could be investigated on a particle by particle basis giving insight into the kinetics of the phase transition in II-VI semiconductors. This could include investigating the number of times the phase transition is attempted, the pressure corresponding to the thermodynamic equilibrium, and the rate at which the nanocrystal converts from one phase to the next. These properties are blurred by measurements done on an ensemble level.

To date, the only experiment that makes an attempt to investigate nanoscale single particles is from Mao et al.[108] This study looked at $NbSe_3$ nanobelts at pressures up to 20 GPa. The nanobelts studied are huge compared to the regime where size dependent behavior has been observed.

To achieve the ability to perform single particle optical studies under high pressure, a multitude of obstacles involving the optics of the system, the diamond anvil cell, and the sample must first be overcome.

## 6.3 The Diamond Anvil Cell

### *6.3.1 Optical Problems with the Diamond Anvil Cell*

One of the major problems associated with measuring the fluorescence of single nanoparticles in a diamond anvil cell is the presence of the diamond itself. Diamond has a high index of refraction of 2.42. In addition, the reflection loss through the diamond when the four diamond surfaces present in the diamond anvil cell are taken into account is roughly 50%.[29] If the excitation source and the particle fluorescence is bright enough this loss should not play a limiting role in the optics of the system. The major problem associated with imaging in a diamond anvil cell can most easily be explained through the treatment of the diamond as a plane parallel plate.[29] For a parallel plate in a collimated beam, no aberrations are introduced into the system. However, when the same parallel plate is placed in a converging or diverging beam, a series of aberrations including chromatic, spherical, and astigmatism are introduced. For the purposes of imaging single particles, the spherical aberration shall be discussed in detail.

When a plane parallel plate is inserted into a converging or diverging beam, the beam is displaced longitudinally due to change in index relative to air (Figure 6.1). The longitudinal displacement, $\Delta_p$, can be calculated from the equation:

$$\Delta_p = \frac{(N-1)}{N} t, \tag{6.1}$$

where N is the index of refraction and t is the thickness of the plate.[109] For a diamond with a thickness of 1.8 mm (the thickness of some of the diamonds used here), the longitudinal displacement of the image is 1.06 mm. This equation only applies to the paraxial region. Outside the paraxial region the longitudinal displacement, $\Delta_m$, is:

$$\Delta_m = \left[1 - \sqrt{\frac{1-sin^2 u}{N^2-sin^2 u}}\right] t \cong \left[1 - \sqrt{\frac{4(f/\#)^2-1}{4N^2(f/\#)^2-1}}\right] t, \tag{6.2}$$

where f/# is the f-number.[109] Assuming a 50 x objective with a numerical aperture of 0.55, $\Delta_m$ can be approximated as 1.16 mm for a diamond anvil. From these values, the longitudinal spherical aberration, defined as the difference between $\Delta_m$ and $\Delta_p$, for the diamond anvil is 0.1 mm. The blur diameter for this spherical aberration, defined as:[110]

$$B_{sphere} = \frac{(N^2-1)t}{32N^2(f/\#)^3}. \tag{6.3}$$

For a diamond anvil and the above described objective, the blur diameter of the spherical aberration is 0.026 mm. This is significant given the size of the point source that is being imaged.

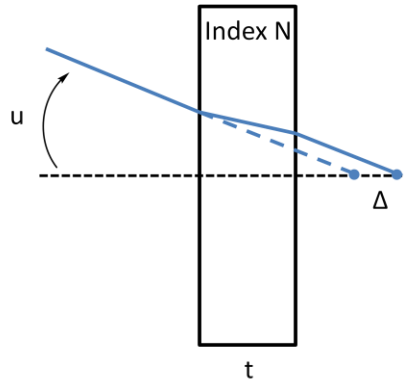


**Figure 6.1:** A plane parallel plate in a converging beam. The beam is displaced by a distance of Δ.

Typically, the spherical aberration can be corrected for through the use a microscope objective with a correction collar. Unfortunately, for the case of the diamond anvil, the spherical aberration is too great to be completely corrected through this method particularly given the constraints placed on the objective by the use of a diamond anvil cell. The working distance required by the use of the diamond anvil cell limits the number of objectives available for this purpose to only a handful, none of which have a correction collar for the correction of spherical aberration.

The spherical aberration and loss of signal due to the presence of the diamonds pose a significant challenge in imaging signal nanoparticle fluorescence and must be overcome for these studies to be successful.

### *6.3.2 Possible Solution: The Mini-Diamond and Diamond Backing Plate Configuration*

By examining the equations defining the spherical aberration above, the simplest way to reduce the aberrations caused by having a thick diamond substrate may be to reduce the amount of diamond through which the light has to travel. One method to achieve this is the use of a perforated diamond anvil as a backing plate (Figure 6.2). In a perforated diamond anvil, the point has been lapped off to a significant extent and a hole has been milled either part way through the diamond or the entirely though the diamond.[111-112] The perforation can be cylindrical or conical. This reduces the amount of diamond through with the excitation source and the resulting image has to pass. For the case of single particle imaging, a partially perforated diamond anvil cannot be used as a backing plate or as an anvil in its own right because the inner surface is not polished.[111] This would lead to the scattering of the light as it passed through this interface and additional blurring of the image.

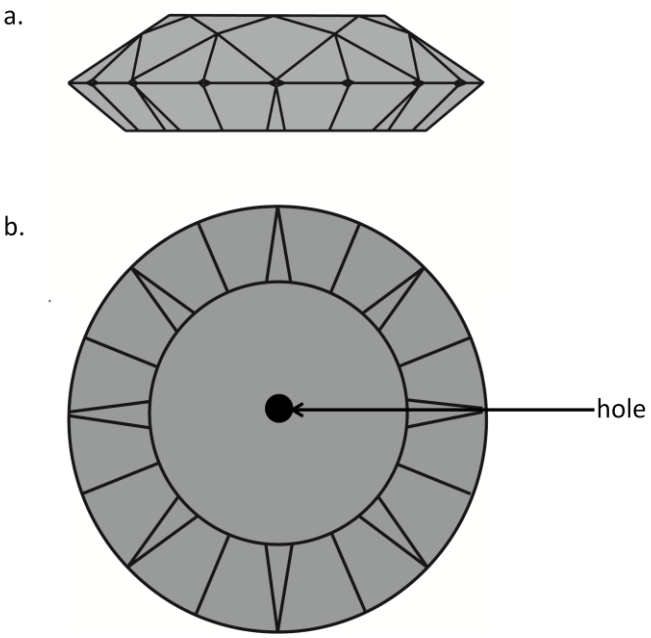


**Figure 6.2:** Schematic of a perforated diamond anvil that can be used as a diamond backing plate: a.) the side view of the anvil b.) the top view showing the hole that has been drilled through the entire diamond.

Because of the imaging issues that would be experienced if a partially perforated diamond anvil was used, a fully drilled anvil must be used for imaging single particle fluorescence. In this case, the fully perforated diamond anvil will actually serve as a backing plate for a miniature diamond anvil to be seated upon (Figure 6.3). Such a configuration has been used to successfully achieve high pressure in the literature.[111-112] For a miniature diamond anvil with a thickness of 0.64 mm, $\Delta_p$=0.38 mm and $\Delta_m$=0.41mm (assuming the 50x, NA=0.55

objective discussed above), giving a longitudinal spherical aberration of only 0.03 mm and a blur diameter of 0.009 mm for the diamond. In comparison, a 1 mm thick glass slide with an index of refraction of 1.52, through which the fluorescence of single nanoparticles can be imaged (albeit they are a bit blurry), has a longitudinal spherical aberration of 0.07 mm with a blur diameter of 0.015 mm. Given this, single particles should be able to be imaged through a miniature anvil. Unfortunately, this rough calculation does not account for defects within the diamond itself, which cause a fluorescent background that is high enough to wash out the fluorescence from the individual particles. Even diamonds that were supposed to possess low fluorescence according to the supplier had too large of a background. Both type I and type II diamonds can be classified as low fuorescence.[29] Ultra-low fuorescence is needed for this application.

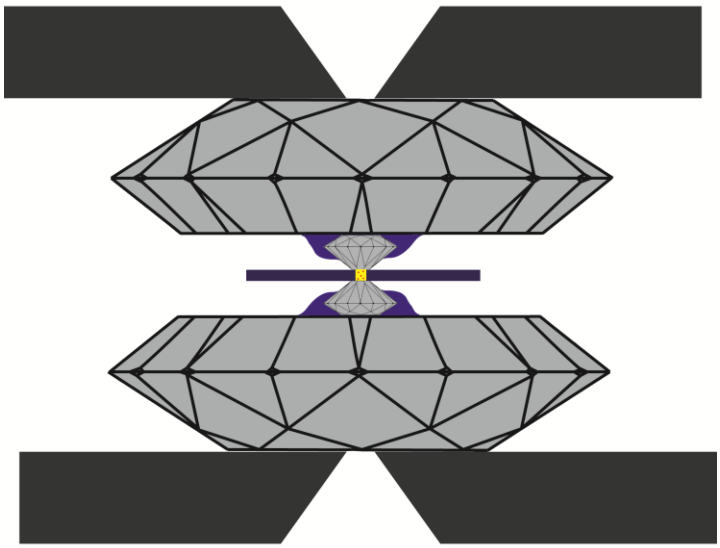

**Figure 6.3:** Diagram showing miniature diamond anvils mounted on diamond backing plate. The diamond backing plates are then secured onto metal backing plates before being put into a diamond anvil cell.

Unless diamond suppliers allow us to screen their diamonds for the ultra-low levels of fluorescence that are required for this experiment, the fluorescence of the diamonds limits the feasibility of this configuration for high pressure single particle imaging.

### *6.3.3 Possible Solution: The Sapphire Cell and the Hybrid Diamond-Sapphire Cell*

From the spherical aberration equations, the reduction of the index of refraction will also result in the reduction of the aberration. Another material that is commonly used for anvil construction in high pressure experiments up to about 10 GPa is sapphire.[113-114] Sapphire has an index of refraction of 1.78. Sapphire is not as hard as diamond, but its mechanical properties are amenable to the lower part of the pressure scale.[113] Because it is not as hard, the machining of sapphire into various shapes, including lenses, is significantly easier. Several geometries of sapphire cells have been used, including one made from truncated ball lenses (Figure 6.4a).[113]

Because sapphire is relatively easy to machine, cells like that shown in Figure 6.4b could theoretically be designed. This configuration, when properly designed, allows for the use of the anvils as solid immersion lenses in addition to pressure exerting apparatuses. A solid immersion lens operates on the same principles that govern oil immersion microscopy.[115] For an oil immersion lens, oil is placed between the lens and the sample. This increases the index of refraction between the two materials, which in turn increases the numerical aperture of the system. A higher numerical aperture implies better optical resolution and collection efficiency. A hemispherical solid immersion lens works on the same principle, but using a high index of refraction solid, such as sapphire, instead of the immersion oil. The hemisphere increases the magnification of the objective lens being utilized and the numerical aperture by a factor of the index of refraction.[116-117] The image passing through the center of the solid immersion lens is free of aberration, but the aberration increases with the angle of the off-axis light.[117] In addition, the hemispherical lens does not possess longitudinal chromatic aberration, only a very small lateral chromatic aberration. Other geometries, such as Weirstrass solid immersion lenses could possibly be used, but they do not provide the same advantages to our application as does a hemispherical solid immersion lens.[117]

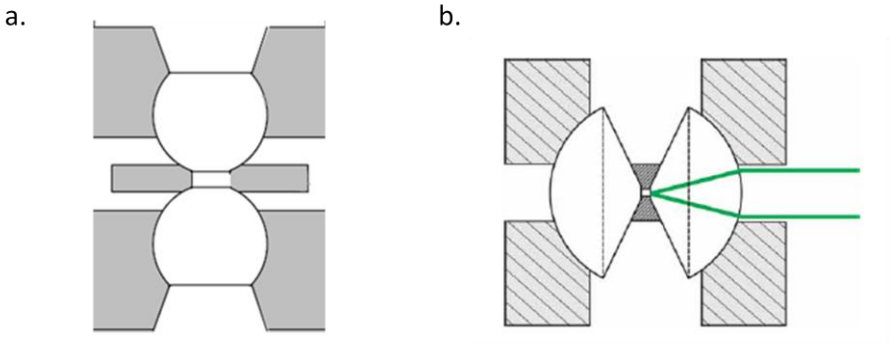


**Figure 6.4:** Diagrams of two sapphire anvil cells. a.) A truncated sapphire ball cell from Reference 113. b.) A theoretical sapphire cell in which the anvil could also be used as a solid immersion lens (from Reference 44).

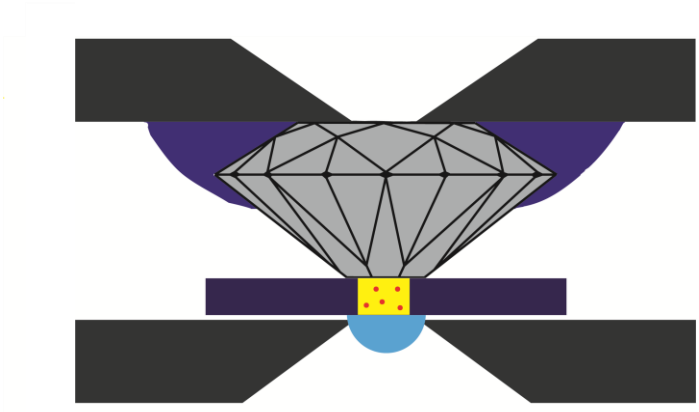

**Figure 6.5:** Schematic of a hybrid sapphire and diamond anvil cell.

Given the increase in collection efficiency and the reduction of the spherical aberration in the center of a hemispherical solid immersion lens, such a lens would be ideal for imaging inside a high pressure cell. Unfortunately, a supplier for the sapphires shown in the configuration shown in Figure 6.4b could not be found. However, sapphire ball lenses and hemispherical lenses are prevalent. A design for a high pressure cell consisting of one diamond anvil and one sapphire hemisphere was proposed (Figure 6.5).[118] This cell would allowed for particles located on the surface of the sapphire hemisphere to be imaged under high pressure, provided that the hemisphere could support the pressures required.

Before the cell could be subjected to pressure, the ability to image single nanoparticle fluorescence on top of the solid immersion lens had to be determined. Unfortunately, the sapphire half ball lenses purchased from several suppliers show similarly high backgrounds and contamination from $Cr^{3+}$ doping and defect states (Figure 6.6).[44,118] This background could be reduced, but not eliminated, from the sapphire by annealing at high temperatures. This high background prevented the observation of single particle fluorescence even if the high intensity higher wavelengths were filtered out through the use of band pass filters.

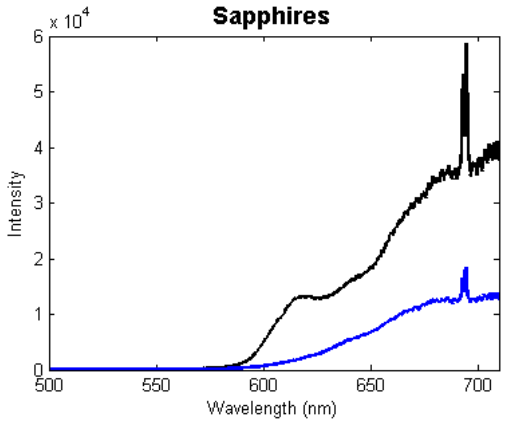


**Figure 6.6:** Fluorescence spectra of two different sapphires from two different suppliers. The ruby peak around 690 nm that is due to $Cr^{3+}$ doping of the sapphire.

## *6.3.4 Possible Solution: Correction Outside of the High Pressure Apparatus*

In many cases, spherical aberration can be corrected for by the simple addition of an optic with a longitudinal displacement in the opposite direction into the image path. For instance, a convex, or converging, lens will have an undercorrected (negative) spherical aberration, opposite of that of a plane parallel plate.[119] A concave, or diverging, lens will have an overcorrected (positive) spherical aberration.[119] A convex or plano-convex lens could therefore be used to correct for the positive spherical aberration introduced by a plane parallel plate. Many types of aberration come into play when trying to calculate the type of lens that needs to be used, making such calculations difficult. For the diamond anvil cell, several commercially available lens combinations were placed between the microscope and the spectrometer in an attempt to correct the spherical aberration. None of the commercially available lenses in the standard lens kit that

were tested corrected for the spherical aberration adequately. A custom made lens or series of lenses could be designed for this purpose in the future.

## 6.4 The Sample

### *6.4.1 Loading Difficulties*

If the optical challenges could be overcome, there would still be several sample difficulties that would need to be surmounted. The first of these difficulties is the convenience of having a planar sample for single particle imaging. A 2-dimersional sample, such as that created by a dilute solution drop casted onto a cover slip, makes finding the individual particles, and subsequently imaging them, a lot easier. A 3-dimensional sample poses challenges stemming from an increase in the background due to out of focus particles and simply being able to find and focus on individual particles. Background from the surrounding medium will also contribute to the signal and pose additional difficulty. This could simply be overcome by drop casting a dilute sample of the particles on the surface of the diamond before loading with a pressure transmitting medium that the particles are not soluble in. Unfortunately, such a technique, while simple, may introduce a non-hydrostatic environment around the particle as it would no longer be completely surrounded by the pressure transmitting medium. An additional method that may overcome these issues, would be to embed the particles in a glass that is not soluble in the pressure transmitting medium. While this would probably cause an increase in the background, reducing the signal to noise, it would provide a hydrostatic environment if the glass was chosen carefully.

### *6.4.2 The Nanocrystals*

The second obstacle to be overcome is the sample itself. It would be ideal to have a sample that undergoes an abrupt shift in emission wavelength from one color in the visible spectrum to another during a phase transition. Unfortunately, when undergoing a structural phase transition from the wurtzite or zinc blende phase to the rocksalt phase, many II-VI semiconductors actually go from a system with bright fluorescence to one that does not fluoresce. This is because the low pressure wurtzite and zinc blende phases are direct band gap semiconductors in which fluorescence is allowed, but the high pressure rocksalt phase is an indirect band gap semiconductor in which fluorescence is forbidden process. This means that the particles would be going from a bright "on" state to a dark "off" state. This process would then be convoluted with the blinking phenomenon that has already been observed for single II-VI nanocrystals. If the II-VI semiconductor system is to be used for these experiments, then the blinking of the particles must be suppressed.

One method of suppressing blinking in II-VI nanoparticles is to deposit a thick epitaxial shell made of cadmium sulfide around a cadmium selenide core.[120-121] This prevents fluorescence loss by reducing the number of surface traps and confining the hole to the cadmium selenide core.[120-121] This reduces the blinking frequency, allowing for particles with long "on" times and high quantum yields to be synthesized. A synthesis of these CdSe/CdS core/giant shell

particles based on Reference 121, with a few changes is described below using the successive ion layer absorption and reaction (SILAR) method.

### 6.4.2.1 Synthesis

**Reagents:** Cadmium oxide (CdO, 99.99%), oleic acid (70% tech grade), selenium powder (-100 mesh), oleylamine (90%), and sulfur (99.5%) were purchased from Sigma-Aldrich. Octadecene (ODE, 90%) was purchased from Lancaster. Trioctylphosphine (TOP, 98%) was purchased from STREM. Tetradecylphosphonic acid was purchased from PCI Synthesis. Common solvents such as methanol, isopropanol, acetone, and hexane were also purchased from Sigma-Aldrich

**CdSe Quantum Dots:** Before the reaction was to be performed a $Cd(oleate)_2$ (0.5 M in oleic acid) was prepared by heating 0.145 g CdO in 2 mL oleic acid to 170 °C under flowing Ar. The precursor solution was then cooled to room temperature and stored under Ar. The TOP-Se precursor was synthesized by stirring 158 mg of Se powder and 2 mL of TOP overnight in the glovebox. In a 25 mL 3-neck round bottom flask equipped with a condenser, thermocouple adapter, septum, and stir bar, 0.2 mL of the $Cd(oleate)_2$ precursor and 3 mL of ODE were combined and heated to 70 °C under vacuum for 1 hour. The flask was then backfilled with argon and heated to 240 °C. In a separate flask (equipped the same as above), 1.5 mL of the TOP-Se precursor, 1.5 mL of oleylamine, and 1 g of TDPA were combined and heated to 110 °C under argon until the solution turned clear. The TOP:Se solution was then injected into the flask containing the cadmium mixture using a glass syringe with a wide bore needle. The temperature was lowered to 200 °C and grown for 50 seconds after the injection. The solution changed colors from colorless to yellow, then orange to red. The solution was cooled to 60 °C and 5 mL of hexane was added before the solution cooled to room temperature. The cleaning of the nanocrystals consisted of a two step process. In the first step, the reaction mixture was layered with MeOH. The top MeOH layer was removed, and the process was repeated once. In step two, isopropanol was added to the colored layer and the solution was centrifuged to yield a pellet of nanocrystals. The pellet was dissolved in hexane. The solution was repeatedly precipitated and re-dissolved until a clear, clean solution of nanoparticles in hexane was obtained. The particle size was characterized by absorption and transmission electron microscopy. The solution concentration was determined from the absorption coefficients in Reference 74.

**SILAR Precursors:** The cadmium precursor was synthesized in a 25 mL 3-neck flask by combining 256 mg of CdO, 4.38 mL oleic acid, and 5.62 mL ODE and heating the mixture to 250 °C under Ar until the CdO was completely reacted. The mixture was then diluted to a 0.1 M concentration in Cd by the addition of ODE. The sulfur precursor was synthesized in a 25 mL 3-neck flask by combining 64 mg of S and 10 mL ODE and heating to 200 °C under Ar under the sulfur was dissolved. The sulfur solution was then diluted to a concentration of 0.1 M in S by dilution with ODE.

**Calculations for the Addition of the Shell Material:** The amount of the cadmium and sulfur precursors was determined by first determining the surface area of the particles. Then, given the thickness of a single monolayer of CdS and its density, the amount of each precursor could be calculated on a per monolayer basis.

**CdSe/CdS Core/Shell Particles:** In a 50 mL 3-neck round bottom flask equipped with a condenser, thermal couple adapter, stir bar, and septum 2 mL oleylamine, 4 mL ODE, and approximately $8.13\times10^{16}$ CdSe nanoparticles (solution in hexane) were combined. The hexane was removed under vacuum. When the majority of the hexane had been removed, the solution was heated to 70 °C and degassed under vacuum for an additional 30 minutes to remove any remaining hexane and air. The reaction mixture was then backfilled with argon. The stock cadmium precursor (enough for a single monolayer) was added dropwise to the reaction mixture. The temperature was then increased to 230 °C. Ten minutes after the desired temperature was achieved, the same volume of the sulfur precursor was added dropwise. The temperature was then increased to 240 °C. The dropwise injections of the cadmium and sulfur were alternated every 10 minutes until the desired shell thickness was achieved, ending on cadmium. Twenty minutes after the final injection, the reaction was cooled to room temperature. Afterwards, ~5 mL of hexane was added and the reaction mixture was transferred to the glovebox. Particles were cleaned using the same process as that of the CdSe dots. Self-nucleated CdS particles were removed through additional layering with methanol and centrifugation. The amount of CdS was monitored through fluorescence.

**Characterization:** Particles were characterized using transmission electron microscopy in addition to absorption and fluorescence. Absorption was collected on an Agilent 8453 UV-vis, while fluorescence was performed on a Horiba Fluorolog. A FEI Tecnai $G^2$ S-Twin transmission electron microscope operating at 200 kV using a $LaB_6$ filament was used to image the nanocrystals.

## 6.5 The Fluorescence Microscope

The configuration of the fluorescence microscope for performing single particle experiments at high pressure is perhaps the easiest challenge to overcome. Single particle experiments are now common place and adapting a microscope to accommodate a diamond anvil cell, while maintaining the ability to image the emission from a single particle, is not terribly difficult (Figure 6.7). In this case, a Lexel 95 $Ar^+$ Ion laser set to emit at 488nm was used as an excitation source. It was passed through a spatial filter to clean up the beam shape and a laser line filter to exclude any other wavelengths that may have escaped from the laser. A focusing lens before the back of the microscope can be used to control the beam size. For single particle imaging inside a diamond anvil cell, a 50× Zeiss LD EC Epiplan-Neofluar objective with a NA=0.55 and a working distance of 9 mm was chosen. This objective provides the working distance required to accommodate a small diamond anvil cell, in addition to the magnification and numerical aperture required to image single particle fluorescence with good signal to noise. A Zeiss Axiovert inverted microscope was chosen as it provided plenty of space on the stage to accommodate the diamond anvil cell. The fluorescence spectrum was dispersed by an Acton SpectroPro 300i and collected by a Princeton Instruments Spec-10 liquid nitrogen cooled camera. This configuration has proven to be adequate for the imaging and spectroscopy of single nanocrystals.

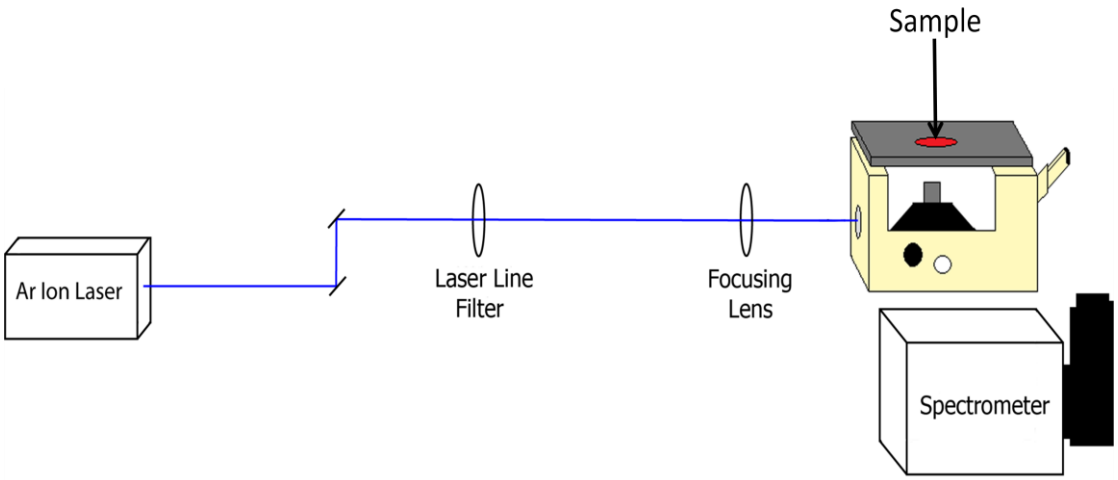


**Figure 6.7:** Diagram of the laser setup used for measuring fluorescence from single nanocrystals.

## 6.6 Conclusions

Performing single particle fluorescence experiments under high pressure poses multiple challenges that are difficult to overcome. The microscope geometry and the sample issues are fairly easy to overcome, but the optical aberration introduced by the presence of the thick substrate is more difficult to overcome. Several possible solutions were explored, each yielding small improvements in the spherical aberration, but the aberration was still a problem. If these difficulties were overcome, a better understanding of the behavior of nanoparticles under high pressure could be achieved.

# Chapter 7

# Detection of Cellular Forces Using a Nanocrystal Sensor

## 7.1 Abstract

The photoluminescence of cadmium selenide/cadmium sulfide core/shell nanocrystal tetrapods has proven to be extremely sensitive to minute forces. Once calibrated, these particles have been shown to be able to correctly map out forces in polymer fibers under tensile stress. In this work, tetrapod nanocrystals were shown to provide a viable route towards imaging forces in biological systems. The nanocrystals provide the system with spatial and temporal resolution. By covalently linking hydrophilically modified tetrapods to a glass substrate, the tetrapod fluorescence can be used to monitor forces in biological systems. An acousto-optic tunable filter was necessary on the detection side of the microscope to impart the measurement with the temporal, spatial, and spectral resolution needed to map out the forces exerted on a substrate by the cultured cells. HL-1 rat cardiomyocytes were used as a trial system, as they exert a dynamic force on their surroundings as they beat. From the fluorescence of the tetrapod substrate, the force exerted by the HL-1 cardiomyocytes was determined to be 0.7 nN, which agrees with values determined through other experimental methods.

## 7.2 Introduction

### *7.2.1 Tetrapod Nanocrystals*

The colloidal synthesis of nanocrystals has evolved such that shaped controlled heterostructures can be easily achieved.[22] The cadmium selenide- cadmium sulfide (CdSe/CdS) system is a perfect example of this control. CdSe/CdS heterostructure nanocrystals can be synthesized as core-shell dots, rods, or tetrapods.[22,121] Tetrapods are a branched nanostructure consisting of four wurtzite CdS arms grown epitaxially from the (111) facet of a zinc blende CdSe dot (Figure 7.1).

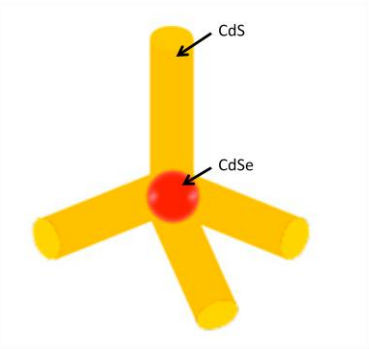


**Figure 7.1:** Drawing of a CdSe/CdS core/shell tetrapod.

In these structures the hole is confined to the CdSe dot, but the electron is delocalized across the entire structure due to the band alignment of the two materials.[106,122] This electronic structure, in addition to the geometry of the nanocrystal, leads to unique mechano-optical properties observed when these particles are subjected to high pressure. In a diamond anvil cell (DAC), the fluorescence of CdSe/CdS tetrapods under high pressure was investigated and compared to that of dots and rods of the same composition.[123] It was determined that the emission wavelength of these particles is extremely sensitive to force, showing a detectible change in emission energy with a change on the order of nanonewtons of force.[123] In addition, when incorporated into various polymers, the Young's modulus of the polymer could be determined from a tensile test based solely from the observation of the shift in the fluorescence wavelength.[124] The fluorescence of these particles in polymers could also be used to map out strain heterogeneities in the polymer fiber.[124]

Given the sensitivity of these particles to miniscule forces and their ability to map out local heterogeneities, it was thought that these CdSe/CdS tetrapods could be used as a force sensor in biological systems.

### *7.2.2 Forces in Biology*

Cells generate a force on their surroundings. Cells are capable of generating forces in a biology system through actin assembly and other mechanisms.[125] These forces can be transmitted between cells or to the extracellular matrix. The interactions between the cell-generated forces, the extracellular matrix, and other cells play a significant role in biological processes including stem cell differentiation, cancer metastasis, cell survival and growth, and cell communication.[125-129] Forces in these biological systems are dynamic and can be changed through an assortment of biological pathways depending on the system under investigation.[7] They also act over various length scales. Sometimes, a force localized in one region can be transmitted through the extracellular matrix to a region far away.[125] Various methods have been used to measure these forces, each with its own set of advantages and disadvantages. Microfabricated arrays of fluorescent particles allow the position and direction of the force to be deduced to some extent, but not the magnitude of the force.[130] Elastomeric vertical cantilevers allow for the determination of the magnitude and direction of the force, but the spatial resolution is poor.[131] Atomic force microscopy measurements of the cellular forces are difficult and time consuming.[132] These techniques have provided important insight into biological forces and the

mechanical properties of cells and tissues, but these forces occur with a spatial resolution much smaller than the current state of the art resolution allows.

By using the fluorescence of tetrapod nanocrystals as a force sensor, it is possible to monitor the periodic forces generated by HL-1 rat cardiomyocytes with simultaneous spatial, temporal, and spectral resolution. This is an important step towards monitoring cell-generated forces with submicron resolution.

## 7.3 Experimental

### *7.3.1 Synthesis*

#### 7.3.1.1 Synthesis of CdSe/CdS Tetrapod Nanocrystals

CdSe/CdS tetrapod nanocrystals were synthesized from a two part literature preparation as follows.[22]

**Reagents:** Cadmium oxide (CdO, 99.999%) and 1-octadecence (ODE, 90%) were purchased from Alfa Aesar. Myristic acid (99%), selenium powder (-100 mesh, 99.99%), oleic acid (90%), oleylamine (70%), propylphosphonic acid (PPA, 95%), diaminohexane (98%), (1-ethyl-3-(3-dimethylaminopropyl)carbodiimide hydrochloride (EDC), N-hydroxysulfosuccinide (sulfo-NHS), hydroxylamine (50 wt%), poly(maleic anhydride alt-1-tetradecene) (polyMAAT) and sulfur (S, 99%) were purchased from Sigma-Aldrich. ACS grade methanol, acetone, hexane, chloroform, and toluene were also purchased from Sigma-Aldrich. Trioctylphosphine oxide (TOPO, 99%) and trioctylphosphine (TOP, 98%) were purchased from STREM. Octadecylphosphonic acid (ODPA) was purchased from PCI Synthesis. Dulbecco's phosphate buffered saline (DPBS, 1×) with no cadmium chloride and no magnesium chloride was purchased from Gibco. Amine coated glass coverslips were purchased as a special order from ArrayIt. All chemicals were used as received with no purification.

**Zinc Blende CdSe Dots:** In a 100 mL 3-neck roundbottom flask equipped with a condenser, thermocouple adapter, septum, and magnetic stir bar, 0.077 g of CdO, 0.29 g of myristic acid, and 5 mL of ODE were combined and heated to 250 °C under argon. When the solution was golden in color it was immediately cool down to approximately 40 °C, at which point 32 mL of ODE was added to the reaction vessel. The solution was heated to 80 °C under vacuum for 1 hour. In a separate vial, 0.1 mL oleic acid, 1 mL oleylamine, and 4 mL ODE were combined and degassed under vacuum. After 1 hour, the cadmium solution was backfilled with argon and cooled to room temperature. Selenium powder (0.024g) was added to the reaction mixture which was promptly heated to 50°C and degassed under vacuum for 10 minutes. The reaction was once again backfilled with argon and heated to 240 °C. During the heating, the reaction mixture changed colors from colorless to yellow to orange to red. The oleic acid, oleylamine, and ODE mixture was added dropwise to the reaction about 3 minutes after the reaction mixture had reached temperature. The nanocrystals were allowed to grow at 240 °C for 1 hour before they were cooled to room temperature. Cleaning was performed through successive centrifugation after precipitation by an anti-solvent (methanol or acetone) and redissolution in

hexane or toluene. The resulting nanocrystal solid was weighed and then dissolved in enough TOP to a create 4 mg/ mL solution.

**TOP-S:** A stock solution of TOP-S was made by combining 670 mg of S and 8.31 g of TOP in a vial and stirring overnight under air free conditions.

**Seeded Growth of Tetrapods:** In a 25 mL 3-neck roundbottom flask equipped with a condenser, thermocouple adapter, septum, and magnetic stir bar, 0.207 g of CdO, 1.08 g of ODPA, 0.015 g PPA, and 3.35 g of TOPO were combined and heated to 120 °C for 30 minutes under vacuum. The reaction was then backfilled with argon and heated to 320 °C until the solution was optically clear and colorless. The resulting solution was cooled to 120 °C and degassed under vacuum for 2 hours. It was then backfilled again and heated to 300 °C under argon. TOP (1.5 g) was injected into the reaction mixture at 300 °C. After the reaction had returned to 300 °C, 0.65 g of the TOP-S stock solution was injected into the flask. After about 40 seconds, 0.5 mL of a 4 mg/mL solution of zinc blende CdSe dots in TOP was injected. The temperature was slowly increased to 315 °C at about a rate of 1 °C/minute. The particles were allowed to grow for 20 minutes before the reaction was cooled to room temperature. The resulting nanocrystals were cleaned using successive precipitation with acetone followed by centrifugation, and redissolution in hexane. Once free of excess ligand, the particles were subjected to a size selective precipitation procedure whereby the rods and dots were separated from the tetrapods in solution. This was achieved through the repetitive centrifugation of the particles in solution (no anti-solvent) at 12,000 rpm for about 30 minutes. This yielded a bottom layer that contained a majority of tetrapods, as observed by TEM (see Figure 7.2).

**Characterization:** Particles were characterized using X-ray diffraction and transmission electron microscope in addition to absorption and fluorescence. X-ray diffraction was performed on a Bruker AXS D8 Gadds instrument with a Co Kα source. Absorption was collected on a Agilent 8453 UV-vis, while fluorescence was performed on a Horiba Fluorolog. A FEI Tecnai $G^2$ S-Twin transmission electron microscope operating at 200 kV using a $LaB_6$ filament was used to image the nanodots and nanotetrapods.

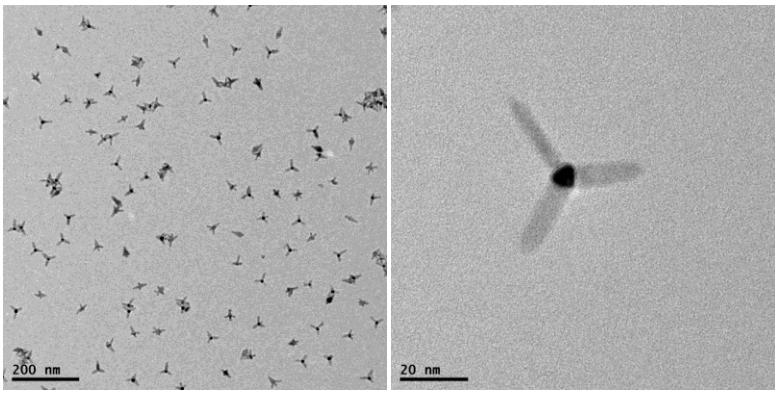


**Figure 7.2:** Transmission electron micrographs of CdSe/CdS tetrapod nanocrystals. The fourth arm for most of the particles is pointing out of the plane.

**Polymer Wrapping:** The native ligands of the tetrapods are hydrophobic, but to be incorporated into a biologically relevant system the particles need to be hydrophilic. In order for this to be achieved, a simple polymer wrapping technique was employed.[133] Briefly, 1 mL of a 1 μM solution of tetrapods in chloroform was prepared. Then, a second solution of 105 mg of diaminohexane in 6.3 mL of chloroform was also prepared. A third solution of 27 mg of poly(MAAT) in 1 mL of chloroform was prepared. The tetrapod solution was combined with the poly(MAAT) solution and stirred overnight at room temperature. Seventy microliters of the diaminohexane solution was added to the tetrapod solution. The solution was allowed to stir for 90 minutes before the chloroform was evaporated off. The tetrapods were dissolved in 1x PBS until the solution was clear. Then, the particles were concentrated using Amicon Ultra 100K centrifuge filters. The resulting carboxylic acid terminated particles were stable in 1× DPBS over a period of weeks.

### 7.3.1.2 Synthesis of Covalently Linked Tetrapod Monolayers on a Glass Substrate

**Chemistry:** The terminal carboxylic acid group on the outside of the ligand shell lends itself to the possibility of doing chemistry with other species in solution and on substrates. This functional group was utilized as part of a zero-length crosslinking reaction to link the hydrophilic tetrapods to the surface of a glass slide. The commonly used EDC/sulfo-NHS coupling lends itself nicely to this application, as seen in Figure 7.3.[134]

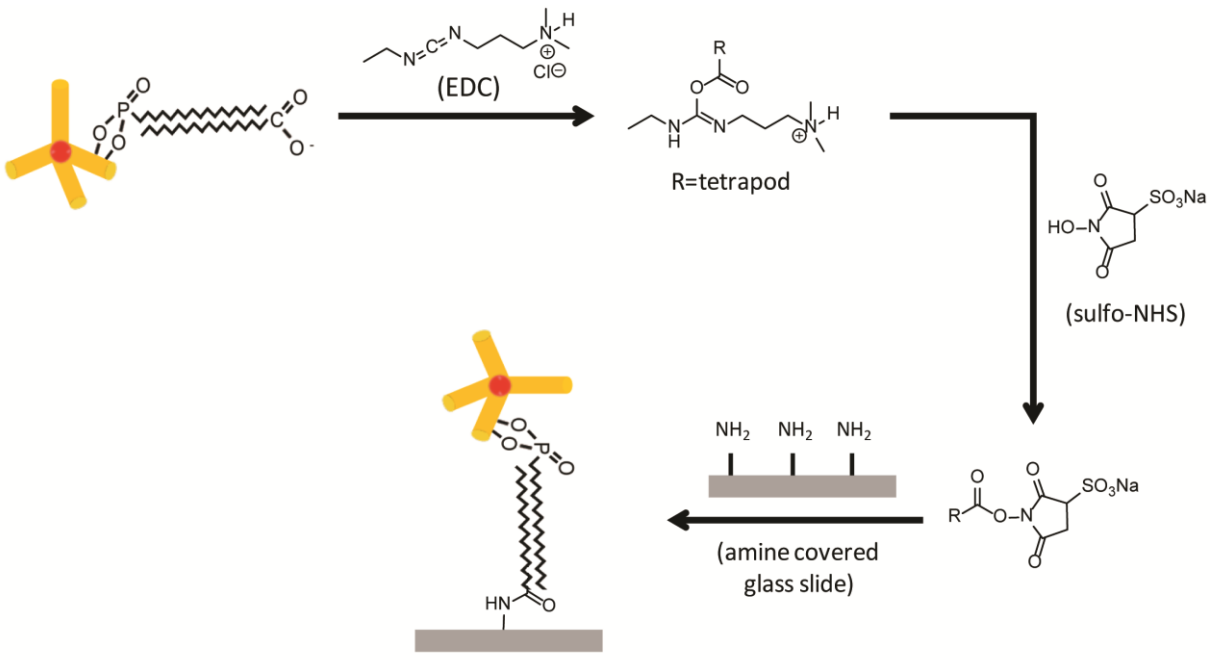


**Figure 7.3:** Reaction scheme for covalently linking the carboxylic acid terminated ligand shell of the tetrapod nanocrystals to an amine coated class slide.

**Procedure:** The conjugation reaction was performed in TabTek well chamber slides. An ArrayIt amine coated cover slip was placed in one of the wells with the amine side facing up. In an Eppendorff tube, 0.24 mg of EDC, 0.66 mg of sulfo-NHS, and 600 µL of a 100 nM solution of polymer wrapped tetrapods in PBS were combined and allowed to react together for 20 minutes on an auto-vortex. The reaction mixture was carefully added to the chamber slide well and then placed on a rocker for several hours to overnight. In order to achieve a good monolayer of tetrapods covalently linked to the slide, this procedure had to be repeated 3-4 times. The tetapod solution could easily be regenerated between each reaction. The tetrapod solution was carefully removed from the well and the slide was covered in 1× PBS. Hydroxylamine (2.5 µL) was added to the tetrapod solution and placed on the auto-vortex for 15 minutes. The particles were then concentrated using an Amicon Ultra 100K centrifuge filter. While in the filter, the particles were rinsed 3 times with additional 1× PBS to remove any unreacted reagents before being redissolved in 600 µL of 1× PBS. The procedure was then repeated as many times as necessary to create a bright uniform monolayer of particles. Slides were stored with 1 mL of 1× PBS on top of them until they were needed for cell culture.

### *7.3.2 HL-1 Cell Culture*

Cell culture was performed offsite at the University of California at San Francisco by Jonathan Chou according to the protocol of Claycomb.[135] The cells cultured on top of the tetrapod coated slides were similar in all ways to those without the tetrapods, indicating that the presence of the tetrapod monolayer did not interfere with the culture of the cells. Before cell culture, the slides were covered with a thin layer of fibernectin.

### *7.3.3 Detection of Spectral Shifts: AOTF Microscope*

In order to detect the small spectral changes that were observed with spatial, temporal, and spectral resolution, an AOTF was incorporated into the detection side of a fluorescence microscope (Figure 7.4). This microscope consisted of a Lexel 95 $Ar^+$ Ion Laser emitting 488 nm. The beam was passed through a spatial filter, laser line filter, and 2× beam expander before being directed through the back port of a Zeiss Axiovert inverted microscope. Data was collected with a Zeiss 40x LD Plan-Neofluar objective with a numerical aperture of 0.6, a working distance between 0-1.5 mm, and a correction collar.

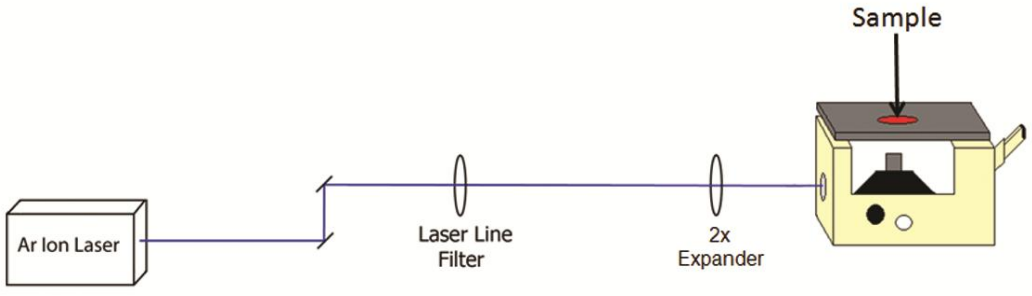


**Figure 7.4:** Diagram of the beam path for the fluorescence microscope.

Typically, the light from this microscope is directed to a spectrometer and a CCD camera, but such a configuration does not give the simultaneous spatial, temporal, and spectral resolution that is needed to map out the forces in a dynamic system. In order to achieve all three at once, an acousto-optical tunable filter (AOTF, Crystal Technologiy PCAOM VIS No. 97-02838-01) was incorporated after one of the side ports of the microscope. The configuration of this detection scheme is shown in Figure 7.5. The AOTF allows for the rapid collection of an image at each wavelength of interest.[136-138] A series of images at individual wavelengths can then be stacked together to give a 2-dimensional image with a spectrum at each pixel. By synchronizing the AOTF with an Andor X-ion EMCCD, each 2-dimensional spectral image was achieved in a 350 ms timeframe by imaging 100 different wavelengths at 3.5 ms per wavelength. The synchronization was achieved through the use of TTL pulses directed through a custom printed circuit board made by Dale Giffords (Figure 7.6). The spectrum at each pixel was fit to a Gaussian, the center wavelength of which was used to plot spatial differences across the image.

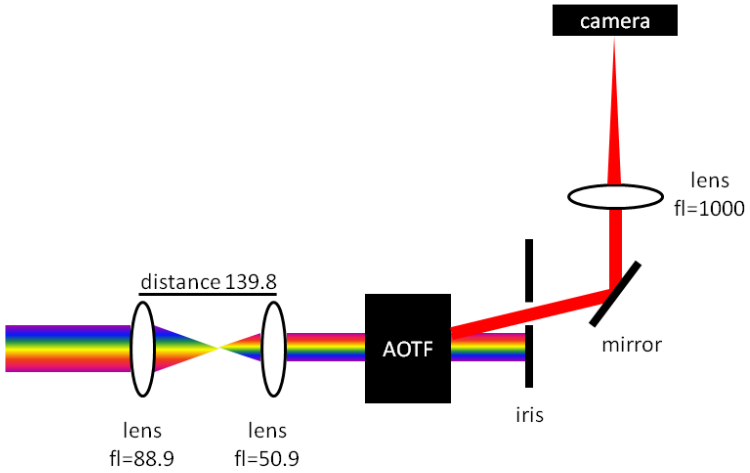


**Figure 7.5:** Beam path after the microscope directing the light through the AOTF. The first pair of lenses acts as a beam reducer and collimates the beam. The iris serves to block the undiffracted beam. The final lens focuses the image onto the camera.

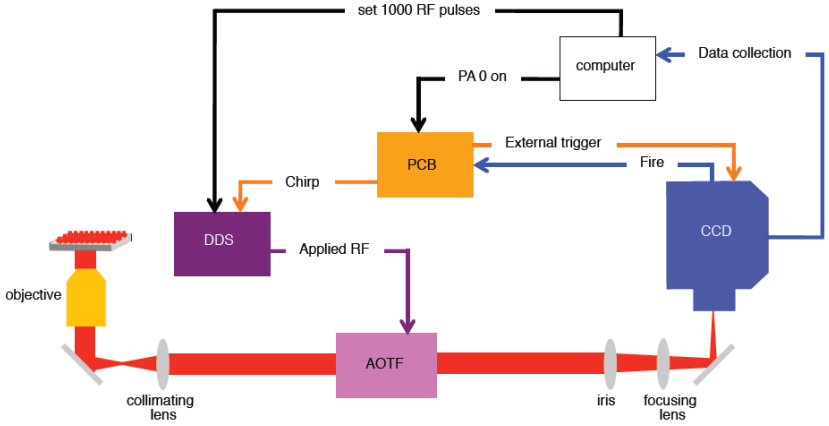


**Figure 7.6:** Diagram showing the method of synchronization between the AOTF, the computer, and the CCD (image from Reference 139).

A detailed description of the AOTF used in these experiments, its synchronization, and its use is provided in Appendix B of this dissertation.

## 7.4 Results and Discussion

A single monolayer of tetrapods was covalently linked to an amine coated glass slide. The fluorescence from the monolayer was bright and uniform across the size of the laser beam. While some defects in the monolayer could be observed from the fluorescence image, there were always large areas of uniform fluorescence available for imaging. A 2-dimensional spectral image could easily be obtained from the monolayer of tetrapods.

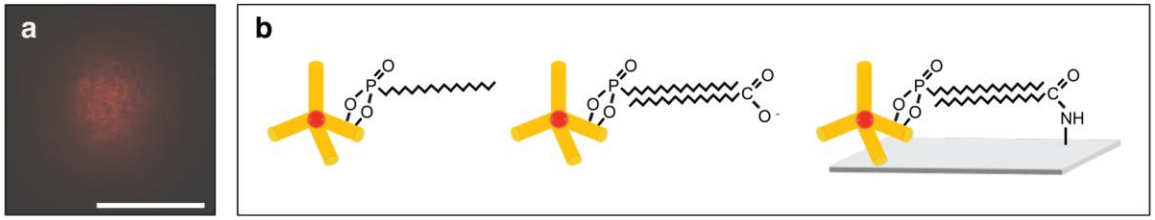


**Figure 7.7:** a.) A fluorescence image of the tetrapod monolayer showing the uniform fluorescence of the tetrapods. The scale bar is 100 µm. b.) A schematic showing the covalent linking of the tetrapods to the substrate. (Figure from Reference 139)

HL-1 cardiomyocytes cultured on top of these fluorescent substrates showed the spontaneous contratractile behavior characteristic of this particular cell line (Figure 7.8).[135] Because of the atmospheric environment under which these measurements were obtained, the cells did not beat regularly as they would have in an environment with a controlled $CO_2$ concentration.

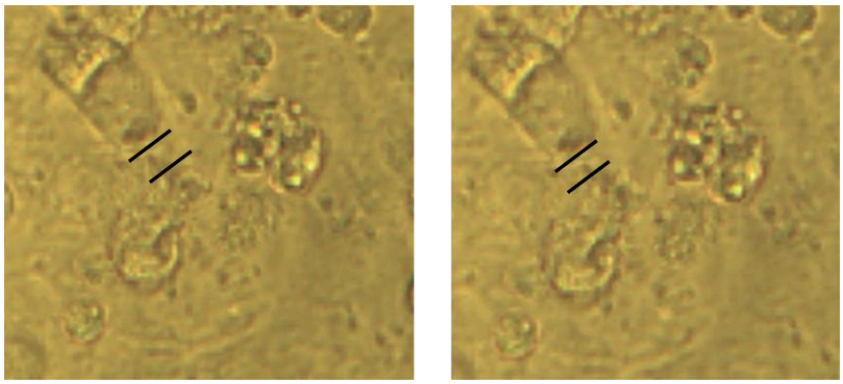

**Figure 7.8:** Brightfield image of HL-1 cardiomyocytes. The black lines indicate an area of the culture that was beating. The lines get closer together as the cells contract. The yellow color is due to a laser line filter.

As the HL-1 cardiomyocytes contracted, they exerted a force on their surroundings, including the tetrapod-covered slide on top of which the cells were cultured. When the fluorescence spectrum of the illuminated tetrapods was measured as the cells beat, a spectral shift was observed. This was not uniform across the illuminated area, but was instead heterogeneous as one would expect from a cell (Figure 7.9). In Figure 7.9, each frame takes 350 ms to collect. Each pixel had a spatial resolution of 5.1 $\mu m^2$. Twenty consecutive spectra were taken at each point, providing the change in the force over a fairly long period of time. The saturation of the red in each pixel in Figure 7.9 indicates the magnitude of the spectral shift in millielectronvolts. When cells are present, there is a definite spectral shift that changes in time and space. But when no cells were present, or when the cells on top of the monolayers were not beating, no spectral shift was observed from the tetrapod monolayer (Figure 7.9c).

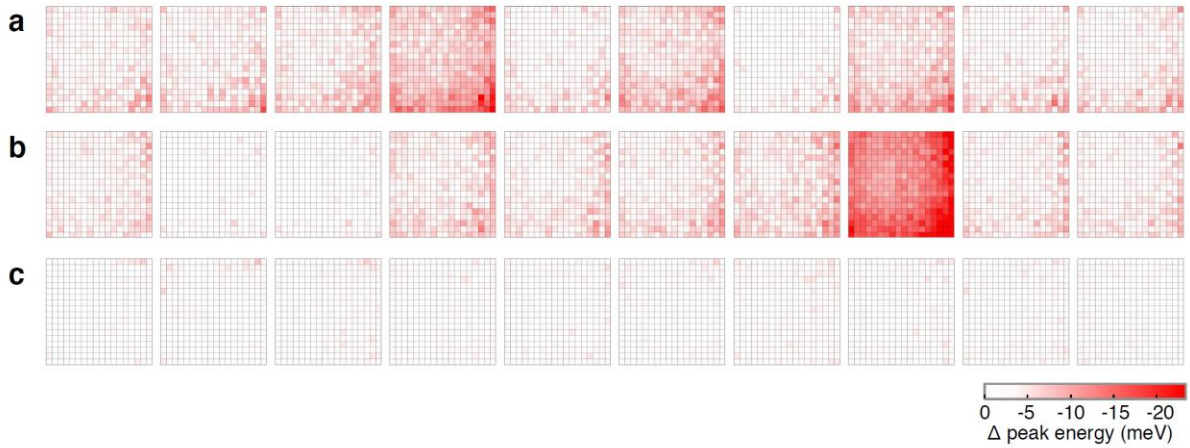


**Figure 7.9:** a and b). The spectral shift of the tetrapods with spatial and temporal resolution at two different sections of the cell culture. Each frame was 350 ms after the previous one. c.) A control sample with no beating cells. No significant spectral shifts were observed in the control.

The force due to the cell contraction was extracted from the spectral shift relying on theoretical calculations of the spectral shift due to an uniaxial force on one of the arms of the tetrapod.[122] The force was found to be 0.7 ± 0.4 nN per tetrapod. This is the same order of magnitude found in previous experiments using more complicated methods for force measurement.[130] It should be noted that the force exerted by the cell can be altered by its environment.[129] In this case the substrate is glass, which is relatively hard compared to the tissues that this cell line would be surrounded by in a biological system. This experiment proves that these tetrapod nanocrystals are capable of measuring forces on the same order of magnitude as those exerted by cells.

## 7.5 Future Work and Conclusions

The use of the fluorescence properties of tetrapod nanocrystals as a probe of cell-generated forces with spatial and temporal resolution has been shown to be viable experimental method. The correct order of magnitude for the force exerted on a glass substrate by HL-1 rat

cardiomyocytes was determined solely by the shift in the fluorescence spectrum of the tetrapod nanocrystals. More work is necessary to expand the systems that this technology can be applied to.

As was previously mentioned, the force exerted on a substrate by a cell is affected by the stiffness of the substrate that the cell is cultured on. The colloidal nature of the tetrapods allow for the possibility of their incorporation into a variety of biologically relevant substrates, including collagen. Collagen is a common extracellular material that is found in various forms in the majority of animals. Bone and tendon are just two examples of tissues that consist of collagen. Collagen consists of three amino acid chains that form a triple helix as shown in Figure 7.10 a and b.[140] The collagen molecules then form a hierarchical structure that ranges in its size scale from nanometers to micrometers (Figure 7.10 c-e).[140] In addition, the mechanical properties of collagen are fairly well studied, making it an ideal system into which tetrapods could be incorporated.[140] Collagen has free amino groups on its molecules, allowing for the same EDC/sulfo-NHS chemistry to be performed to covalently link the tetrapods to a collagen substrate.

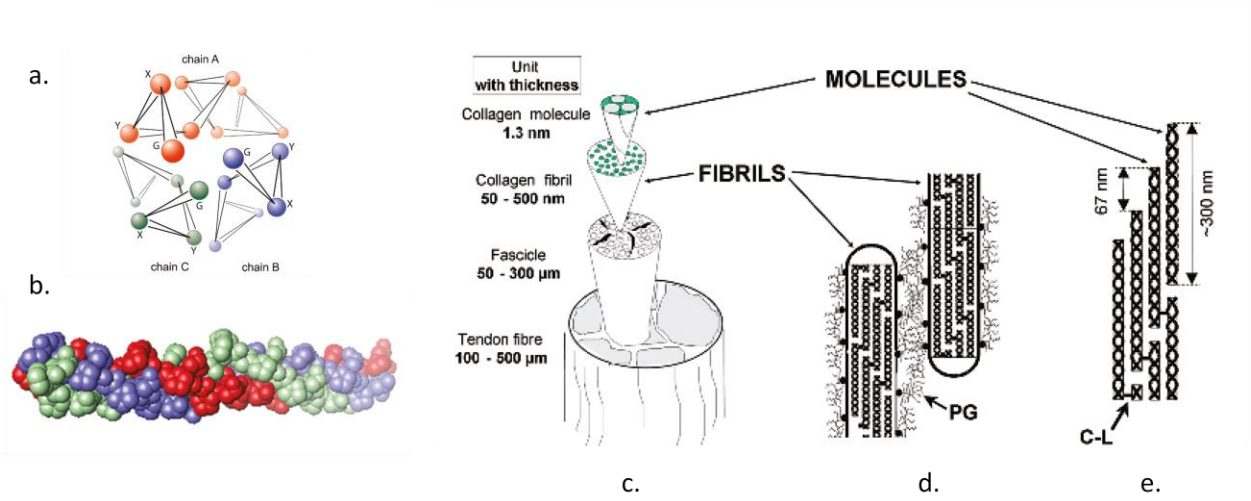


**Figure 7.10:** a and b). A schematic from reference 158 showing the molecular structure of a single collagen molecule. c, d, and e). The hierarchical structure of collagen in a tendon. (image from reference 140).

Once the tetrapods are incorporated uniformly into a collagen sample, mechanical testing with simultaneous measurement of the fluorescence shift could be performed to acquire a better calibration curve for the shift with force. In order to do this, a homebuilt tensile test capable of maintaining an aqueous environment around the collagen sample, while providing a window by which the excitation and the collection of the emitted light can still occur was built (Figure 7.11). The stretching of the sample is performed by a small motor of the type typically used to move around optics on a laser table. Combining the tensile test with the fluorescence measurement will provide a calibration of the spectral shift of the tetrapods with force in a biologically relevant system. This can be then be use as a force sensitive substrate for cell culture in the future.

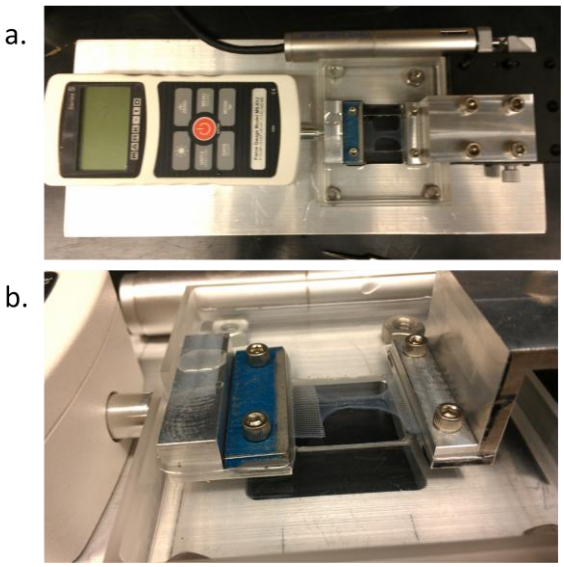


**Figure 7.11:** a.) Photograph of a homemade tensile tester. b.) A collagen sample being stretched by the tensile tester. The window below the sample allows for laser excitation and the collection of the emitted light.

In the future, a better understanding of the interface between the tetrapod, its substrate, and the cell is needed to understand the intricate interplay that plays a role in response of the tetrapod nanocrystal sensor.

# Chapter 8
# Conclusions and Future Work

## 8.1 Conclusions

In conclusion, this work has demonstrated that small changes to the structure of a nanomaterial can affect the phase transition pressure. For the CdSe/ZnS core/shell system, it was found that for shell thicknesses below the critical thickness, the upstroke phase transition pressure is reduced. The presence of the shell changed not only the thermodynamics of the system, but also the optical properties of the nanocrystals under high pressure. The fluorescence peak goes from a single Gaussian in pure CdSe nanocrystals to multiple peaks for the core/shell system under high pressure. From this, it can be hypothesized that in the case of the CdSe/ZnS core/shell system, a material combination with smaller lattice mismatch would yield a smaller change initially, but a better trend could be developed, as the critical thickness would be much greater. In the case of $Bi_2Se_3$ intercalated with copper, the phase transition pressure was increased relative to the same nanoribbons with no copper. These systems provide a unique insight into the interplay of material strain and thermodynamics through the manipulation of the phase transition conditions.

Furthermore, a better idea of the mechanism of the phase transition in cadmium sulfide nanocrystals has been elucidated from ultrafast shock wave experiments performed with an X-ray probe. The *h*-MgO intermediate was observed for the first time, in accordance with its prediction from theory.[100-103] Because the *h*-MgO intermediate was found only at low shock stress and it was never the majority phase, it was determined that multiple transformation pathways are followed.

The possibility of performing single nanoparticle optical experiments under high pressure was also explored. While steps were taken towards correcting the spherical aberration, no one method proved sufficient to correct the aberration in a functional manner. Additional problems with the sample and sample loading were revealed.

In addition, the optical properties of tetrapod nanocrystals under pressure were used to observe and quantify the force exerted by a HL-1 cardiomyocytes. While not the first time such a force has been quantified, tetrapod nanocrystals provide a sensor that allows for data collection

with both spatial and temporal resolution. An AOTF on the detection side of a fluorescence microscope allowed for the collection of the data with spatial, temporal, and spectral resolution. This technique also allows for the future quantification of forces in biology on the size scale that they are actually exerted (the nanoscale). This technique can be extended to biologically relevant systems, such as collagen.

There are many outstanding questions with regards to phase transitions in nanocrystals. While steps towards addressing some of them have been addressed in this work, more experiments are needed.

## 8.2 Future Work

### *8.2.1 Introduction*

There remains a large body of work that has yet to be performed regarding phase transitions in nanocrystals. This section is meant to provide a brief overview of several outstanding questions in the fields of high pressure and high temperature structural phase transitions and melting phenomena in nanocrystals and the experiments that would provide some insight into these important questions.

### *8.2.2 High Pressure Behavior of Doped Nanocrystals*

It is well known that phase transitions in bulk crystals nucleate at defects in the lattice.[2] Crystal defects include grain boundaries, twin boundaries, substitutional defects, and interstitial defects. An example of a substitutional defect is shown in Figure 8.1. An interstitial defect sits between lattice points instead of replacing one of the atoms. In a perfect crystal, even the surface can be considered a defect, as the atomic/molecular environment at the surface is different than the bulk of the crystal. A defect can introduce a site in the crystal where the energy barrier that must be overcome to nucleate the new phase is less than in the perfect lattice, thus nucleation of the new phase at a defect site is preferred.[37] The effect of these defects on the phase transition in nanocrystals is unknown.

Doped semiconductor nanocrystals can now be synthesized with a number of different dopants[141-146] and would provide an ideal case study for investigating the effect of substitutional and interstitial defects on the phase transitions. For substitutional dopants, the dopant is never the same as size as the cation or anion that is supposed to occupy that position in the lattice; they will be either larger or smaller. This will cause a strain field to be present around the dopant. Dopants located in the interstitial sites will also induce a strain field around the impurity, as they occupy a site that is not typically populated and the surrounding atoms must change their positions to accommodate this. There are several examples of synthetic routes that yield $Mn^{2+}$ and $Cu^{2+}$ doped CdSe nanocrystals with the dopant in the bulk of the crystal instead of on the surface.[141,145] One paper even cites the ability to controllably synthesize CdSe nanocrystals with exactly four copper atoms per particle.[141] This is an important advance in synthetic techniques, as nanocrystals are naturally self purifying and usually impurities are pushed to the surface

during growth.[36] Other dopants in CdSe nanocrystals include $Ag^{2+}$, $Mg^{2+}$, and $Co^{2+}$, but the lattice position of the dopant in these systems is not as well characterized.[143,144,146]

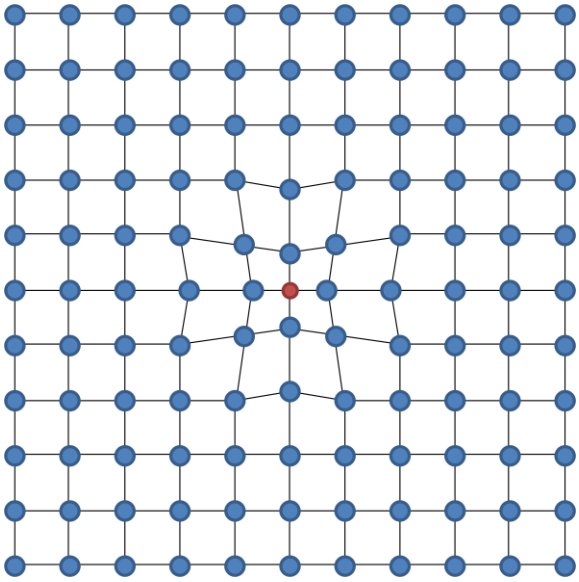

**Figure 8.1:** An example of a substitutional defect. The red atom represents the defect. In this case, the atoms around the defect move to accommodate the smaller size of the defect.

In nanocrystals, the effect of defects (besides the surface) on the high pressure phase transition behavior has yet to be investigated. In doped nanocrystals, the dopant site and surrounding strain field introduces a defect into the once "perfect" nanocrystal. Given that the high pressure phase transition in bulk crystals nucleates at the defect sites present in the crystal, it follows that the dopant sites should provide lower energy nucleation sites in the nanocrystal. While this would probably have a minimal effect on the thermodynamics of the system, the kinetics of the system should be affected to a greater extent. For instance, the increased width of the hysteresis curves for CdSe nanocrystals relative to the bulk has been attributed to the lack of nucleation sites. If nucleation sites are introduced in the nanocrystal through doping, then the overpressurization needed to induce the nucleation and growth of the new phase should decrease due to a lowered activation energy. A similar process should be in effect for the pressure downstroke, where the underpressing necessary to induce the reverse transition should be less. This would yield a narrowing of the hysteresis curve when dopants are present.

Since recent synthetic procedures have shown the ability to dope CdSe nanocrystals with different ions,[141,143-146] it can be imagined that the effect of the dopant on the phase transition could be tuned by changing from one dopant to another. A greater change in the phase transition conditions could be observed when there exists a larger difference in the size or oxidation state between the dopant ion and those in the host lattice.

In addition, it is easily imagined that the number of dopants per nanocrystal could also play a role in the high pressure phase transition behavior. More dopants would yield more

available nucleation sites. This could yield faster transformations and the possibility for multiple nucleation steps per particle. Multiple nucleations in a single particle would yield fractured or multi-domain particles.

Given the possibility that dopants change the phase transition such that the upstroke phase transition is reduced for nanoparticle, a more accessible method for the synthesis of the high pressure structural phases of semiconductor nanocrystals could be achieved.

### *8.2.3 Cobalt Phase Transitions at High Temperature*

Nanoparticles of cobalt have been found to exist in a phase that had not been previously found in bulk.[147] Bulk cobalt can be found as two different structures: face-centered cubic (fcc) and hexagonal close-packed (hcp). The fcc phase is preferred at higher temperatures, while a mixture of hcp and fcc can be found under ambient conditions.[147] The two structures differ only by their stacking along the 111 direction (hcp exhibits ABAB stacking, while fcc exhibits ABCABC stacking). Stacking faults are thus common in crystals of cobalt because the energy between the two structures is low.[147] For nanoscale cobalt, an additional crystal structure was discovered: ε-cobalt (ε-Co).[147] The unit cell of ε-Co is cubic with $a$=6.097 Å and is similar to that of β-manganese with Z=20.[147] Nanoparticles are easily synthesized in the hcp phase and the ε-Co phase (Figure 8.2).[148-150] It has been found that the hcp nanoparticles of Co transform to the ε-Co phase when heated to about 200 °C.[148] The ε-Co then transforms to fcc when heated about around 500 °C.[148]

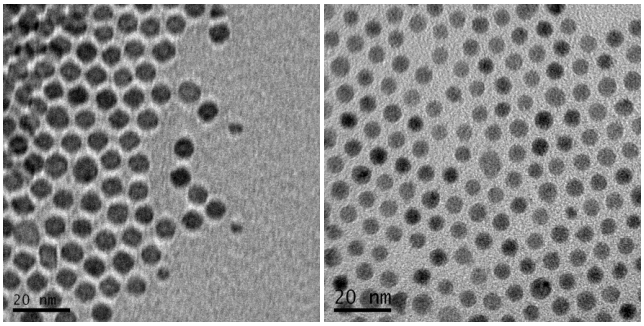


**Figure 8.2:** Transmission electron micrographs of spherical ε-Co nanoparticles synthesized through the decomposition of $Co_2(CO)_8$.

These phase transitions have not been well characterized. Simple differential scanning caloritmetry (DSC) would provide an idea of the relative energies of the structures. Preliminary experiments (taken by Simone Raoux at Brookhaven National Lab on particles synthesized in the Alivisatos group by Mark Polking and the author) using temperature dependent X-ray diffraction confirm the phase transition from ε-Co to the fcc structure (Figure 8.3). It also seems to indicate a low scattering, or amorphous phase at higher temperatures. During experiments such as this, extreme care must be taken in order to avoid coalescence and sintering of the nanoparticles. This yields larger particles that will lead to a biasing of the size dependent results.

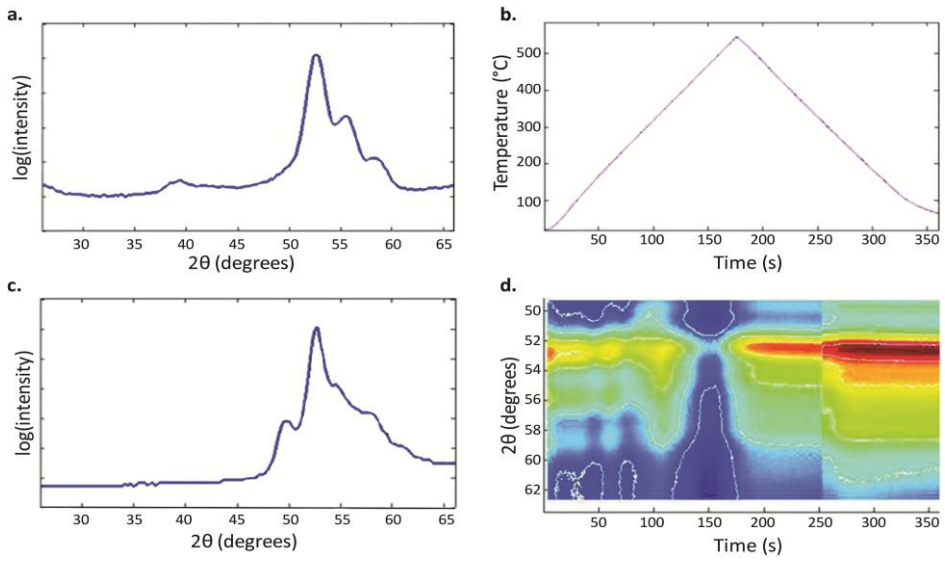


**Figure 8.3:** a.) XRD pattern of 6.9 nm diameter ε-Co nanoparticles before heating. b.) The temperature ramp profile for the experiment. c.) XRD pattern for the recovered fcc phase of Co. d.) The diffraction pattern of the Co nanoparticles with time during the temperature ramp in b.

It is conceivable that single particle experiments investigating the phase transition in Co nanoparticles could be achieved with an ultra-stable heating stage in an electron microscope (see below).

## *8.2.4 Single Particle Phase Transition Behavior*

While Chapter 6 of this dissertation outlines some of the steps that have been taken towards optically probing the high pressure phase transition in semiconductor nanocrystals at the single particle level, more must be done in order to understand the behavior of single nanoparticles as they undergo a structural phase transition. This applies not only to phase transitions that occur under pressure, but also those that occur with temperature. Examples of nanocrystal systems with structural phase transitions that take place with changes in temperature include cobalt,[148] germanium telluride,[151] and copper sulfide.[152] Cobalt nanocrystals will transform from its ε-Co structure (unique in that this phase is only seen in nanocrystals) to a face centered cubic modification with increased temperature.[148] Germanium telluride shows a size dependent phase transition with temperature from a rhombohedral structure (*R3m*) to a rocksalt temperature.[151] The low chalcocite to high chalcocite phase transition in copper sulfide nanoparticles is size dependent and can be induced by an electron beam in a transmission electron microscope.[152-153]

Experimentally, it is much easier to change the temperature of a sample than to apply the type of pressures that are needed for the observation of the phase transitions previously discussed. The most straightforward method to observe single particles and molecules that is commonly used is to observe their fluorescence. Unlike the II-VI semiconductor nanocrystals discussed in Chapter 6, the samples mentioned above are not photoluminescent, thus

fluorescence cannot be used in these cases. With the advent of ultra-stable transmission electron microscope holders capable of heating the sample in a controlled manner while maintaining good image resolution and stability, electron microscopy seems to be uniquely positioned to offer the structural characterization needed for high temperature phase transitions on a nanoparticle by nanoparticle basis. Studies of this sort could investigate the size, shape, and faceting dependence of the structural phase transitions. High resolution electron microscopy would offer insights into the phase transition mechanism, while ultrafast electron microscopy techniques would provide the necessary kinetics data. The downside of electron microscopy is that the electron beam itself has the ability to do chemistry and thus must be accounted for in each and every experiment. Also, electron microscopy techniques are not as high throughput as single particle fluorescence imaging.

In addition to electron micrscopy techniques, there are several beamlines at synchrotron sources that have managed to achieve an extremely small beam size. If the sample being observed possessed a high scattering coefficient and the beam size was made small enough such that only one particle was exposed to the beam at as time, then the observation of diffraction from a single particle should theoretically be observable. Unfortunately, given the limits of current detectors, the exposure time for a diffraction pattern of from an individual nanoparticle may be extremely long. This would only allow for steady state measurements without the possibility of observing any short lived intermediate states. Free electron lasers, such as the LCLS at SLAC, may be able to achieve the necessary beam intensity in a short period of time to allow for the structural characterization of a single nanocrystals while still allowing for temporal resolution.

### *8.2.5 Ultrafast Measurements of Laser Induced Nanocrystal Melting*

When a semiconductor is heated, eventually the material undergoes a solid to liquid phase transition at its melting point. This process occurs in a similar method to the solid-solid phase transitions discussed earlier; the nucleation of the liquid phase inside the solid occurs at defects in the crystal including the surface of the crystal.[154] Under normal heating conditions the rate of change of the material from a solid to a liquid depends on the extent of superheating and is limited by the speed of sound in the crystal.[155] When laser irradiation is used to heat the sample, nonthermal melting becomes possible at high laser fluences.[154-156] Nonthermal melting results from the generation of a large number of electron-hole pairs, which create an extremely dense *e-h* plasma.[154] This makes the lattice unstable and it begins to lose its crystallinity, thus starting the melting process. It relies on the transfer of the absorbed energy from the laser to phonon modes.[154] Nonthermal melting takes place on a time scale much faster than that observed for thermal melting (~100 ps) because the energy transfer to the phonons is extremely fast (~200 fs).[18]

In semiconductor nanocrystals, the melting point is highly size dependent.[149] In addition, nanocrystals are also expected to have a phonon bottleneck, where the number of phonons that can be supported by a single nanocrystal is limited.[157-158] This could yield very different melting phenomena when the crystals are subjected to high laser fluences. Nanocrystals have a high surface to volume ratio which will also play a role in the melting process. Preliminary experiments performed at the LCLS at SLAC, provide X-ray diffraction patterns of cadmium

sulfide nanocrystals at picosecond time delays after exposure to various laser fluences (Figure 8.4). The diffraction from nanocrystals is usually weak, thus in order for a thin enough sample to be investigated without heat transfer concerns, a high intensity, pulsed X-ray source, such as the LCLS was necessary. From experiments such as these, the facet dependence of melting and the size dependence could be extracted from the diffraction data. It is also possible that a size dependence of the transition from thermal to nonthermal melting could be observed.

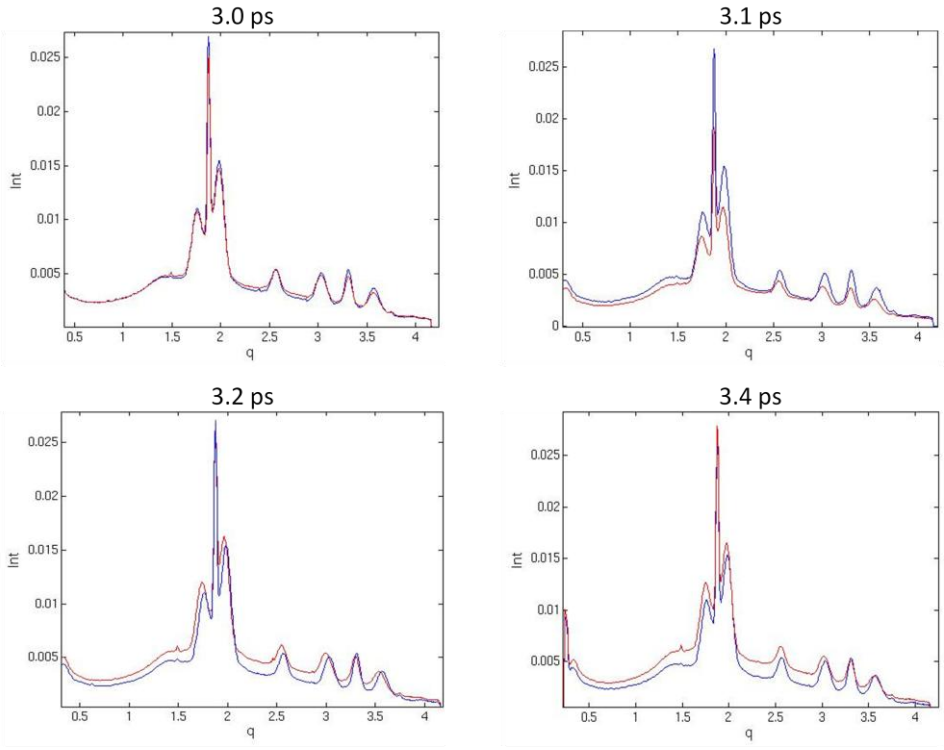


**Figure 8.4:** X-ray diffraction patterns of a 4.4 nm by 18.4 nm CdS nanorod sample at different time delays after being irradiated with a 540 μJ pulse. The blue trace in each plot is a scan of the sample before irradiation, while the red is a scan at the given time delay.

# Appendix A
# Diamond Anvil Cell Basics

## A.1 Introduction

In general, a diamond anvil cell consists of two metal plates opposing each one another. A diamond is placed on each plate in a geometry such that as the metal plates are brought closer and closer together, the diamonds exert more and more pressure on the sample between them. Given that a sample needs to be placed between the diamonds, the diamonds are specially cut to possess a flat culet instead of the pointed culet that is typically used in jewelry (Figure A.1). Other diamond geometries are used in addition to the brilliant cut shown in Figure A.1, but were not used in the course of this work.

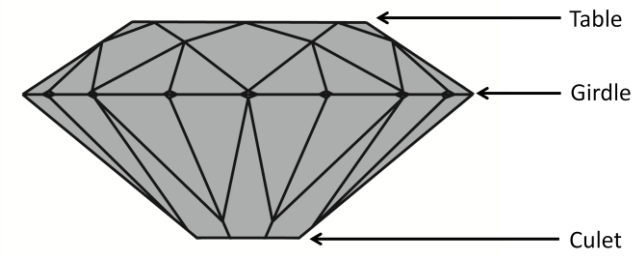


**Figure A.1:** An example of the diamonds used in a diamond anvil cell.

Typically, the sample is contained within a pre-indented and drilled gasket that this held between the two diamonds. Included with the sample are a pressure gauge (such as ruby) and a pressure transmitted medium (Figure A.2). The preparation of the gasket and the loading of the sample will be discussed later.

Before use, the diamonds in the diamond anvil cell (DAC) must be aligned relative to each other to avoid the fracture and chipping of the diamonds. Care must be taken during this process so that the diamonds never touch one another, which will cause damage. The process for alignment varies for each DAC type. Three different, but similar methods, are discussed here for different cell types.

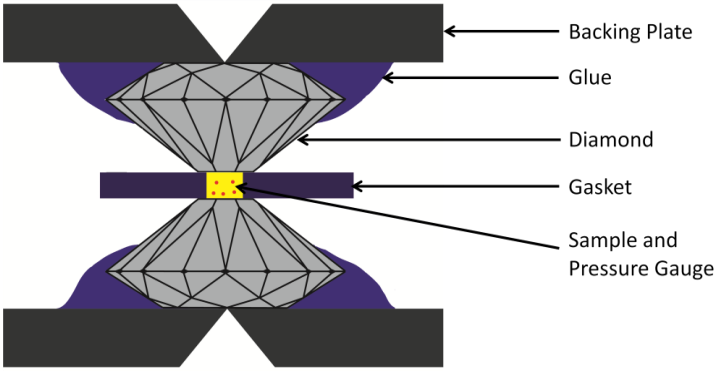


**Figure A.2:** Diamond anvil cell schematic indicating the different parts of the cell.

## A.2 Diamond Mounting and Alignment

### *A.2.1 Merrill Bassett DAC*

A Merrill Bassett DAC (Figure A.3) is a convenient cell as it is small, allowing for easy optical measurements of the sample without requiring a super long working distance objective.

**Figure A.3:** A Merrill Bassett cell from High Pressure Diamond Optics in Tucson, Arizona.

#### A.2.1.1 Instructions for Mounting the Diamonds

1. It is important to use backing plates of a material and configuration compatible with the experiment. Tungsten carbide and inconel are fine for optical experiments, but beryllium

should be used for X-ray experiments. The available collection angle can also be changed as deemed appropriate for the experiment being performed.

2. The selected backing plate is placed in a diamond jig. A diamond jig consists of a base with 3 set screws to hold the backing plate in place and a vertical screw or column with a hole drilled through the middle for visualization of the diamond. The diamond is then placed on top of the backing plate and held in place by the vertical screw. A stereoscope can then be used to align the diamond culet over the center of the backing plate hole by adjusting the position of the backing plate relative to the diamond through the use of the set screws. Once centered, the vertical screw is secured so that the diamond and backing plate cannot move.

3. The diamond is now ready to be glued down. For most applications Stycast 2850 FT with Catalyst 23LV is an appropriate adhesive. It is fairly impervious to the solvents used in the work presented here. If heating is required, a different adhesive may be more appropriate. After mixing the resin and the catalyst, the glue can easily be applied by using a syringe needle or a small broken drill bit. It is important that the glue is not applied too close to the culet or allowed to touch the screw holding the diamond in place. This can cause problems later when removing the backing plate and diamond from the jig.

4. Once the glue is dry (24 hours for Stycast), the backing plate with the attached diamond can be removed from the diamond jig. It can then be secured in the Merrill-Bassett cell through the use of the three set screws present on each half of the cell. The backing plate should be held flat against the cell and not at an angle, in order for the diamonds to be parallel to each other.

### A.2.1.2 Instructions for Aligning the Diamonds

1. Before assembling the two halves of the cell, cover one of the untapped screw holes with a piece of metal (this can be leftover gasket if the metal piece is large enough to cover the hole) held in place with a piece of molding clay on the same side of the cell as the diamond. It is important to clean the culet surfaces with cotton swabs and solvent to make sure no dust, excess glue, or other particulates are present. Then align the red dots on the side of the cell, and carefully push the two sides together without letting the two diamonds touch.

2. The cell can then be turned upside down such that the tapped screw holes are on top. Using the tapped hole above the covered hole on the bottom, thread a screw through the hole until it is touching the metal piece. By adjusting this screw, the distance between the diamonds can be changed accordingly. The diamonds should initially be at least a culet width apart.

3. By using the set screws on half of the cell that is now on the bottom, the position of the bottom diamond can be adjusted so that it sits directly below the top diamond. It is not recommended that the top diamond be adjusted, as loosening the set screws can cause the backing plate to become unseated and susceptible to gravity. Not only should the bottom diamond be directly below the top diamond, but the facets should be aligned to the best of the user's ability. Not all diamonds are perfectly cut, so the user's judgment is generally required as to the when the diamonds are aligned.

4. A Merrill-Bassett cell does not possess any tilt alignment for the diamonds. As long as the cell and the backing plates are machined to a high degree of tolerance in terms of flatness, the tilt alignment does not usually pose a problem. It can be checked by carefully by placing the two diamonds in contact with each other and counting the number of rainbows visible across the cell. The fewer colors present the better the parallelism.

## *A.2.2 Diacell Piston Cylinder DAC*

The Diacell piston cylinder DAC is unique in that it can be pressurized through two methods: through the use of screws or through the use of an inflatable bellow. The bellow pushes down on the cylinder as it is inflated, thus generating the pressure.

**Figure A.4:** Diacell piston cylinder DAC.

### A.2.2.1 Instructions for Mounting the Diamonds

1. It is important to once again choose the appropriate backing plates for the experiment that is to be performed. In addition, the diamonds chosen should have metal rings fitted to them of an appropriate metal such that it does not interfere with the characterization method chosen.

2. To mount the diamonds, carefully unscrew the metal pieces that hold the diamonds and backing plates in place. Then, simply place the metal-ringed diamonds on top of the backing plate and replace the metal pieces to hold the diamonds in place. No glue is necessary for this type of diamond anvil cell.

### A.2.2.2. Instructions for Aligning the Diamonds

1. The alignment procedure is similar to the method to that used for a Merrill Bassett cell. The main exception is that there is enough friction between the two cell halves that there is no need to use a screw to hold the diamonds apart.

2. The major difference for this alignment procedure is the tilt alignment. Once the translational alignment is completed through the adjustment of the four set screws, the tilt must be adjusted. Using a microscope, first check the tilt the alignment with the diamonds lightly touching. This can be done, as previously discussed, by counting the interference rainbows across the culet. It can also be checked by looking at the diamonds from the side and looking for a gap between the diamonds on one side of the culet.

3. Before adjusting the tilt, the diamonds should be separated so that they are no longer touching one another. Then, the three set screws on the back of the piston can be carefully adjusted to adjust the tilt. This should be done in small steps while constantly checking that the diamonds are separated. Sometimes if a large adjustment is made, one of the diamonds can gouge the other. Care should be taken so that this does not happen. When the alignment is complete, no rainbows should be present across the culets when they are in contact with one another.

### *A.2.3 Symmetric DAC*

A symmetric cell (Figure A.5) is fairly similar to a piston cylinder type cell, with the exception that a bellow cannot be used. The configuration of the four screws that are used to pressurize the cell is unique. Two of the screws are reversed threaded, while the other two are threaded normally (righty tighty lefty loosey). This allows for pressurization of the cell without having to turn the cell as much as a standard screw configuration.

The diamond mounting and alignment procedures for the symmetric cell are very similar to those of the Merrill Bassett cell and thus will not be discussed further.


**Figure A.5:** Symmetric diamond anvil cell. The screws labeled "Left" are those that are reverse threaded.

### *A.2.4 Diamond Anvil Cell Conditioning*

Before the alignment can be considered complete, the cell should be conditioned. This is done by compressing a piece of metal (can be the gasket material) between the diamonds. First,

compress the metal only slightly. Then, disassemble the cell and check the diamond alignment. Then, repeat with progressively higher pressures until the diamonds no longer need to be adjusted. If there is a large change in the alignment, start over from low pressures.

## A.3 Gaskets

A gasket between the diamonds serves as a sample chamber and an easy method for keeping the diamonds from coming into contact with one another. The gasket plays a crucial role in what pressures are achievable by the DAC.[28-29] It can also determine what geometry the sample can be observed from. In an axial geometry (probing and collecting through the diamonds) metal gaskets, such as stainless steel, spring steel, and rhenium are typically used. Typically, the harder metals are used for experiments that reach higher pressures. In a radial geometry (probing and collecting between the diamonds), beryllium and boron epoxy gaskets can be used.[43] Because of its toxicity, the use of beryllium is usually avoided. A gasket also supports the sample material under pressure, which increases the maximum pressure that is achievable.[28-29]

A gasket is usually pre-indented before drilling. This prevents the flow of metal from filling in the hole as the pressure is increased and helps the mechanical stability of the gasket.[28-29]

### *A.3.1 Instructions for Gasket Indentation*

1. It is important to choose the gasket material most appropriate for the pressures that are to be achieved in the experiment. This should be cut into small enough pieces such that they easily fit into the cell. It should be recalled that these will sometimes have sharp edges so appropriate care should be taken.

2. To save time later, it is important to carefully measure the distance from the table of one diamond to the table of the other. This is easily achieved through the use of a micrometer with probes small enough to rest within the aperture of the backing plate while the diamonds are in contact with one another.

3. The gasket metal and the diamonds should be cleaned with solvent and a cotton swab to make sure that they are free of dirt and fibers before the gasket metal is secured in place over one of the diamonds using a small piece of molding clay on the edge. A mark should be scratched into the surface of the gasket with a diamond tipped pen pointing to some reference point on the cell so that the gasket can be replaced later in the same position.

4. The cell can then be assembled with the gasket metal between the diamonds. Pressure can then be carefully exerted on the metal by carefully and slowly turning the DAC screws. Care should be taken to make sure the screws are replaced in the same positions from which they were removed every time the cell is used. The best method to go up slowly in a controlled fashion is to turn each screw about one sixth of a full turn (Figure A.6). It is sometimes helpful, especially when learning, to draw out this diagram to help with the consistency of each turn.

5. In order to check the thickness of the gasket as it is being indented, the distance between the tables of the diamonds can be periodically measured. When a distance between the tables without the gasket (Step 2) plus 70-90 μm is achieved, then the gasket between the diamonds is thin enough.

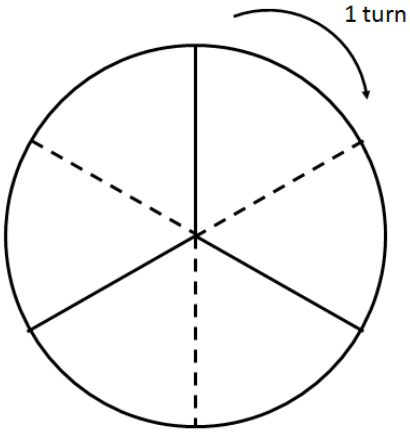


**Figure A.6:** Diagram showing a single turn. This picture is helpful when pressurizing the DAC using the screws.

6. The pressure can then be released slowly. It is important to use the same one sixth turns defined in Figure A.6 and to reverse the order in which the screws are turned. If you tightened the screws in a clockwise direction around the circumference of the cell, then loosen the screws in a counterclockwise order.

7. The final thickness of the indent can then be measured using a micrometer with thin points.

### *A.3.2 Gasket Drilling*

Once pre-indented, the gasket can then be drilled. There are several methods available in order to drill a small enough hole. As a generally excepted rule, the hole should be about one third to one half of the culet size.[28] This can be achieved through a mechanical drill, spark erosion, or a laser miller. A laser miller gives the best shaped hole that is free of metal burrs. All of these methods were used in the work presented here.

## A.4 Samples and Loading

### *A.4.1 Pressure Gauges*

There are several pressure gauges that can be used within the DAC. One of the most commonly used manometers is the fluorescence of ruby ($Cr^{3+}$ doped $Al_2O_3$). The fluorescence of the $R_1$ and $R_2$ lines are been thoroughly characterized and found to shift 0.365 nm/GPa.[44] The splitting and broadening of these peaks can also be used to help determine the nature of the

pressure within the cell (hydrostatic or nonhydrostatic).[44] Other optical sensors include $Sm^{2+}$ doped $SrB_4O_7$, BaFCl, and SrFCl and $Eu^{3+}$ doped LaOCl and $Y_3Al_5O_{12}$.[28] These have a range of sensitivities and can in some cases also be used to determine temperature. Some of the common non-optical pressure calibrants are those that are diffraction standards. These include NaCl, $CaF_2$ (fluorite), $SiO_2$ (quartz), CsCl, Al, Au, Pd, Pt, and Ag.[28,44]

### *A.4.2 Pressure Transmitting Medium*

The medium that surrounds the sample in the gasket chamber is extremely important. The medium can be a gas, solid, or a liquid. The easiest to load are pressure transmitting media that are liquids under ambient conditions. An important consideration when choosing a pressure transmitting medium is whether or not it has been shown to exert hydrostatic pressure on the sample in the chamber. In addition, for nanoparticles, it is important that the particles are soluble in the medium for ease of loading and in order to avoid coupling between particles. A more complete list of pressure transmitting media can be found elsewhere,[1] but those relevant to the studies shown here are ethylcyclohexane and a 1:1 mixture of pentane: isopentane.

### *A.4.3 Sample Loading and DAC Use*

There are several methods by which a sample can be loaded, differing mostly by sample type and personal preference. The method described below seems to work fairly well for loading nanoparticles into the diamond anvil cell.

1. The easiest way to prepare the sample is to dry off the solvent that the nanoparticles are dissolved in and then re-dissolve it in the chosen pressure transmitting medium.

2. Before beginning, the diamonds must be clean and free of any fibers and dirt. It is important to secure the drilled gasket on top of the bottom diamond. This can be done by aligning the mark on the gasket to the reference point on the DAC body and gently pushing down so that the gasket locks into place on the culet. It is helpful to make sure that the gasket surface is clean in addition to the diamonds so that the gasket does not get the culet dirty while it is being secured. A small piece of molding clay can be used to hold the gasket in place.

3. Using an acupuncture needle or similarly thin probe, a small amount of ruby (or a thin piece of gold) can be carefully transferred to the inside of the gasket hole. It is important that this is not thicker than the gasket. Bridging the diamonds can cause errors in the pressure measurement and sometimes damage to the diamonds.

4. The sample can then be added to the gasket hole. Very carefully using a syringe, a single drop of the sample in the pressure transmitting medium can be added on top of the gasket hole. If the concentration of the sample is not high enough another drop can be added, or in the case of a single component pressure transmitting medium, the sample can be allowed to concentrate before closing the cell. This cannot be done with multi-component pressure transmitting media, as the components will evaporate at different rates.

5. The DAC can then be closed and sealed by turning the screws several times. The number of turns (defined in Figure A.6) necessary to seal the cell depends greatly on the DAC being used and the gasket material. A microscope can then be used to check for air bubbles in the gasket hole. Sometimes air bubbles can be gotten rid of by further pressuring the cell, but the majority of the time the cell needs to be reloaded.

6. The pressure can then be increased between measurements by turning the screws by the one-sixth turn described above. At low pressures several one-sixth turns may be necessary to increase the pressure, while at higher pressures less than one-sixth of a turn may be used. Consistently turning all of the screws to the same extent is necessary in order to maintain a hydrostatic environment and prevent a large pressure gradient across the culet.

# Appendix B

# AOTF Synchronization and Use

## B.1 Introduction

The acousto-optic tunable filter, or AOTF, is a useful tool in optics for dynamically controlling the wavelength of light allowed through the filter. It can be placed before a fluorescence microscope to serve as an excitation filter or on the detection side of the microscope to provide spatial, temporal, and spectral resolution.[18-20] It works through the use of a birefringent crystal and an applied radio frequency. The applied radio frequency sets up a type of grating across the crystal which diffracts a single wavelength of light at a different angle from the remaining wavelengths (Figure B.1). The two polarizations of the selected wavelength end up on opposite sides of the undiffracted beam.[18] As the radio frequency is changed, the diffracted wavelength changes. The image is maintained throughout this process, allowing for spatial resolution to be acquired. When the AOTF is placed on the detection side of a fluorescence microscope setup, one can collect an image at a series of wavelengths and combine the images such that each pixel of the resulting image has a spectrum associated with it, providing spectral resolution.[19] Because changing the radio frequency quickly can be achieved with relative ease, temporal resolution can also be obtained, being only limited by the collection times of the camera.

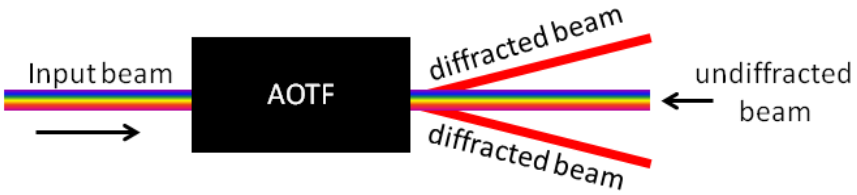


**Figure B.1:** Diagram of the input and output of an AOTF when a radio frequency is applied across the crystal.

## B.2 Instrument and Synchronization

Many AOTF's only accept collimated light; off axis light is rejected by the instrument. As such, the light directed out of the microscope must be recollimated and shrunk in order to pass through the AOTF input aperture. Our Zeiss Axiovert microscope require the use of 2 doublet lenses of focal lengths 88.9 mm and 50.9 mm to collimate and reduce the output light size. These lenses were configured as shown in the Figure B.2. It is important to note that the lenses must be adjusted for the wavelength range to be used. For example, if the red light is to be collected, the lenses should be aligned such that red light is collimated. The chromatic aberration introduced by the lenses is significant enough that when the lenses are aligned to collimate red light, blue light will not be collimated.

Once the light passes through the AOTF, a convenient method to block the undiffracted beam is through the use of an iris or diaphragm (Figure B.2). The diffracted beam can simply be directed through the aperture of the iris and then focused onto the camera using an additional doublet lens.

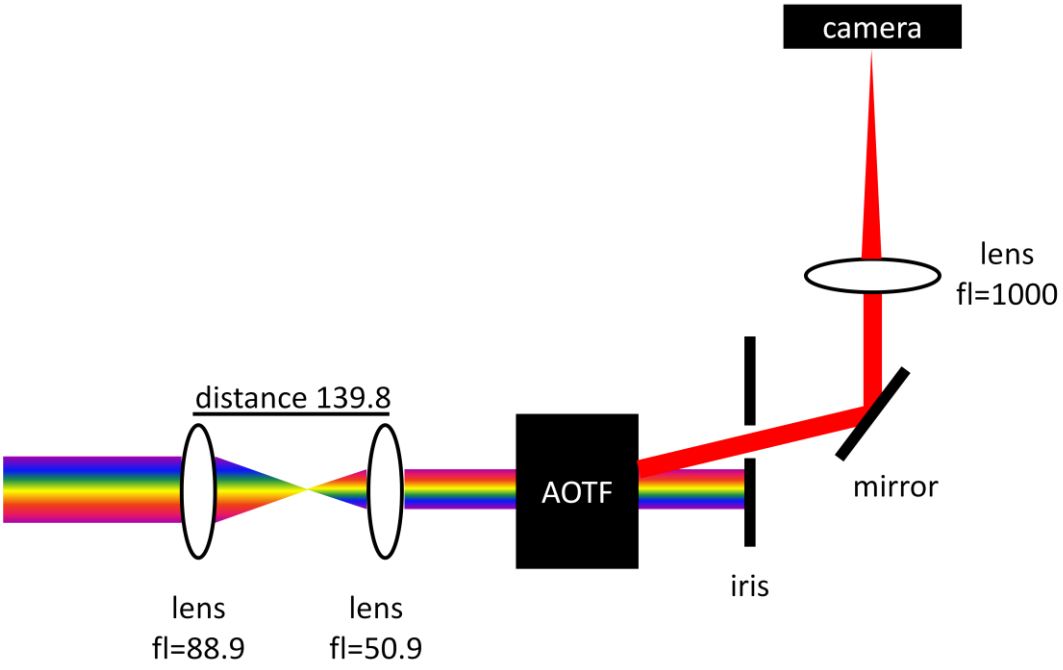


**Figure B.2:** The beam path after the microscope directing the light through the AOTF. The first pair of lenses act as a beam reducer and collimates the beam. The iris serves to block the undiffracted beam. The final lens focuses the image onto the camera.

In order for the AOTF to be used for spatially and temporally resolved spectroscopy in a meaningful way, it must be synchronized with the camera. In our experiments, an AOTF from Crystal Technology (PCAOM VIS No. 97-02838-01) with a DDS controller (Crystal Technology No. 20160) was used in combination with an Andor iXon 897 EMCCD. The synchronization of

these two instruments was achieved through the use of a National Instruments data acquisition (DAQ) PCI card (NI PCI-6503 NI-DAC MX) and a custom printed circuit board made by Dale Giffords. The DAQ was connected to the printed circuit board through the use of a ribbon cable (see Figure B.3). The printed circuit board was then connected to the DDS AOTF controller through the use of another ribbon cable. In order for the AOTF controller and the camera to communicate, two additional connections were made from the printed circuit board to the Andor camera. These cables, which have a BNC connection on one end and a special interface specific to Andor cameras on the other, connected the printed circuit board to the external trigger and fire port of the camera (Figure B.3). With these connections, the AOTF and the camera can communicate with one another.

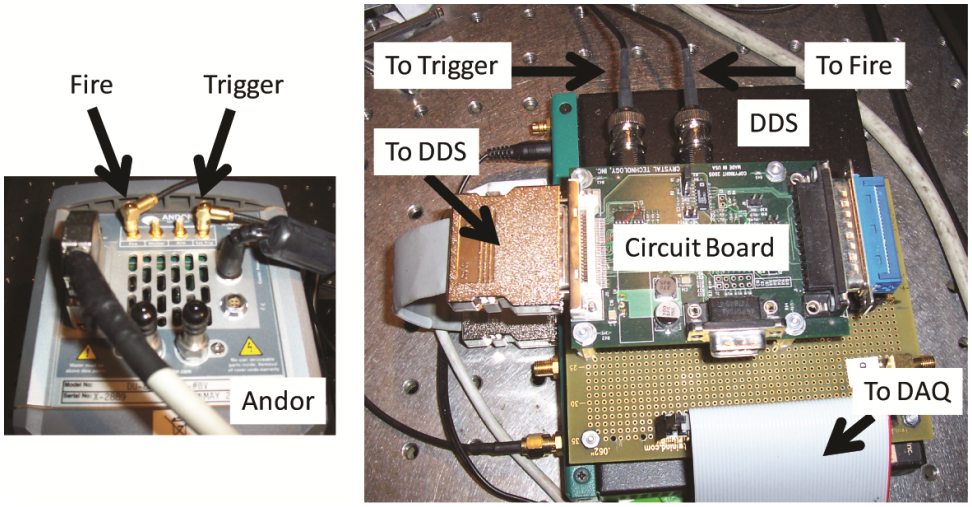


**Figure B.3:** Connections between the AOTF controller, the Andor iXon, and the computer (through the DAQ). The instruments must be connected in this manner in order to communicate with each other

In order to optimize the AOTF, the graphical user interface for the instrument was used to change the frequency and the intensity of the diffracted beam after the AOTF was monitored using the video mode of the camera. The angle and position of the AOTF was adjusted until the highest intensity on the camera was achieved. Once the maximum intensity was achieved, the setup was programmed to collect spectra.

The AOTF has 1024 memory slots that can be used to program different frequencies. The amount of time that each frequency in each slot is delivered to the AOTF crystal can be adjusted by changing the rate of the instrument. Each increment of the rate corresponds to 4 cycles of the controller's internal clock, making the rate increment 10 ns. It was found that a rate of 34928 corresponds to about 35 µs for each programmed frequency. By programming 10 slots with a single frequency, the time at a single frequency was 3.5 ms, which is within the temporal restraints of the Andor camera.

Before a spectrum can be obtained, a program filling the desired number of memory slots with the desired frequencies had to be generated. The AOTF controller has its own coding language that must be used. The programs typically used for our experiments first defined the number of memory slots to be filled and then programed the rate discussed above. Following these two lines were the commands that defined the frequency in each slot. An example is shown below:

```
chirp alloc     -p0   0          1000
chirp rate      -p0   0          34928
chirp freq      -p0   0     0    75.20
```

The first part of each line tells the AOTF controller what to do: allocate memory, define the rate, or fill in the frequency. The second part of the line, -p0, tells the controller to use Profile 0. The numerical value following this, is the channel number. The AOTF controller used is only capable of using a single channel, making this number was always zero. The "chirp freq" command has an additional numerical entry which can possess values from 0 to 1023. This is the slot number. Each slot to be filled needs its own line of code. The last part of each line is the actual input value for that command. The code can be saved a MS-DOS text file and imported to the controller using the command line.

In addition to the AOTF GUI, communication with the AOTF controller can also be established through the use of a command line style interface called AOTF Cmd Interactive. This program allows the user to program the controller using code such as that listed above and query the instrument as to its current state. A list of common commands and queries is given in Table B.1.

**Table B.1**. Useful AOTF Cmd Interactive Commands and Queries

| **Command** | **Purpose** |
|---|---|
| chirp mode -m 0 4 | puts the controller in the correct mode |
| mod ana -m 0 | sets the instrument up to receive signal from the printed circuit board |
| dds a 0 0 | sets the radio frequency amplitude to 0 |
| dds a 0 14000 | sets the radio frequency amplitude to 14000 |
| dds a 0 | asks what the radio frequency is |
| dds f 0 | asks what the frequency in the first slot of memory is |
| chirp alloc -p0 0 | asks how many memory slots are used |
| chirp mode -p0 0 | asks what mode is programmed |

Once the program had been written, several pieces of software had to be used to collect each spectral series. The Andor Solis software, LabView, AOTF Cmd Interactive, and the computer's command line each had to be used in turn. It is useful to note that the AOTF Cmd Interactive software cannot be used to control the AOTF if the command line is already open and controlling the AOTF.

Once the AOTF had been properly aligned and optimized the following instructions were followed in order to collect a spectral series.

## B.3 Instructions for Use

1. Open the Andor Solis program and wait for the camera to cool down. Use the following as the acquisition settings:

    Acquisition mode: Kinetic
    Triggering: External Start
    Readout Mode: Image
    Exposure Time: 0.00260 s
    Number of Accumulations: 1
    Kinetic Series Length: Number of images needed
    Kinetic Cycle Time: 0.00350 s
    Shift Speed: 1.7
    Gain: 5×
    EM: 300
    Chip Size: 64 × 64
    Binning: 2 × 2
    Frame Transfer: On
    Background Corrected Mode

2. Make sure that the AOTF GUI is closed.

3. In the command line of the computer, load the program defining the rate and frequencies to be used in the experiment.

    aotfcmd -t 100 -f filename.txt

    It is important to wait for the program to load completely before closing the window.

4. On the desktop open "AOTF Cmd (Interactive)." To make sure that the AOTF is in the correct mode and waiting for a pulse from the printed circuit board, 2 lines of code need to input:

    chirp mode -m 0 4
    mod ana -m 0

5. Now the LabView program can be opened: AOTF Control (03-04-2011).vis. Upon running the program, a pulse is then sent to the printed circuit board which then synchronizes the AOTF and Andor.

6. In the AOTF Cmd type: dds a 0 0

7. Take the background in the Andor Solis software by clicking "Take Background" and then clicking the run arrow in LabView.

8. In the AOTF Cmd type: dds a 0 14000 or use whatever amplitude is to be used for the data set. Do not use values about 14000 because of the risk to the crystal.

9. Click the camera button in the Andor Solis software followed immediately by the run arrow in LabView. A series of images should be collected, with each image corresponding to a different radio frequency/wavelength.

10. The data can be saved as a .tif file and analyzed using Matlab.

An example of the data collected with the AOTF compared to that collected through the spectrometer is shown in Figure B.4.

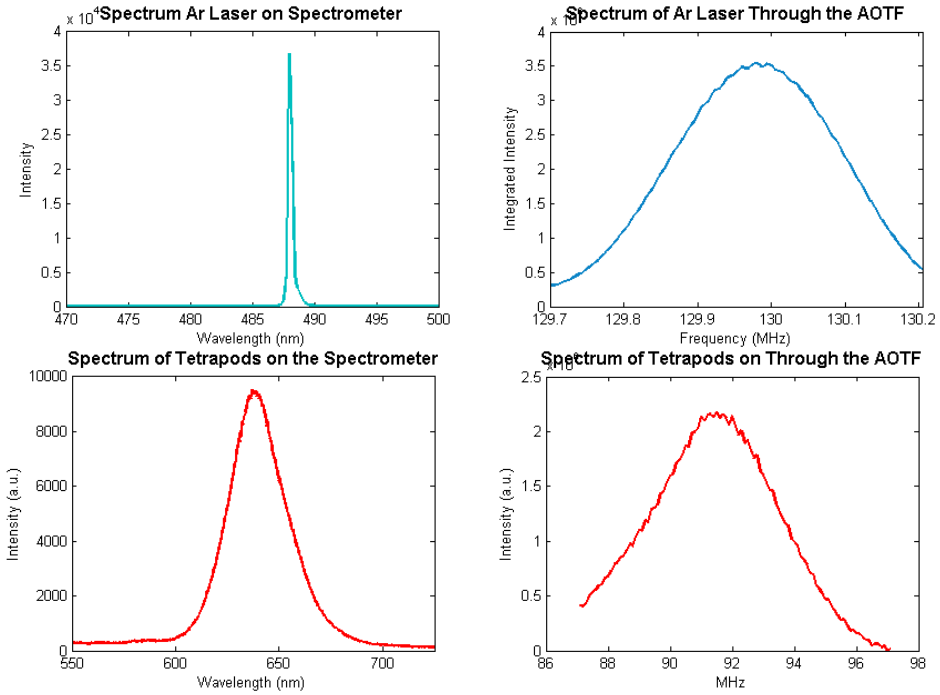


**Figure B.4:** Example of the spectra of the laser beam and a tetrapod sample collected through a spectrometer and through the AOTF.

# References


1. Alivisatos, A. P. Perspectives on the Physical Chemistry of Semiconductor Nanocrystals. *J. Phys. Chem.* **1996**, *100*, 13226-13239.

2. Choi, C. L.; Alivisatos, A. P. From Artificial Atoms to Nanocrystal Molecules: Preparation of More Complex Nanostructures. *Annu. Rev. Phys. Chem.* **2010**, *61*, 369-389.

3. Alivisatos, A. P. Semiconductor Cluster, Nanocrystals, and Quantum Dots. *Science* **1996**, *271*, 933-937.

4. Michalet, X.; Pinaud, F.; Lacoste, T. D.; Dahan, M.; Bruchez, M. P.; Alivisatos, A. P.; Weiss, S. Properties of fluorescent semiconductor nanocrystals and their application to biological labeling. Single Molecules **2001,** 2, 261-276.

5. Kamat, P. V. Quantum Dot Solar Cells: Semiconductor Nanocrystals as Light Harvesters. *J. Phys. Chem. C* **2008,** *112*, 18737-18753.

6. Tolbert, S. H.; Alivisatos, A. P. Size Dependence of a First Order Solid-Solid Phase Transition: The Wurtzite to Rock Salt Transformation in CdSe Nanocrystals. *Science* **1994**, *265*, 373-376.

7. Tolbert, S. H.; Alivisatos, A. P. The wurtzite to rock salt structural transformation in CdSe nanocrystals under high pressure. *J. Chem. Phys.* **1995**, *102*, 4642-4656.

8. Chen, C.-C.; Herhold, A. B.; Johnson, C. S.; Alivisatos, A. P. Size Dependence of Structural Metastability in Semiconductor Nanocrystals. *Science* **1997**, *276*, 398-401.

9. Clark, S. M.; Prilliman, S. G.; Erdonmez, C. K.; Alivisatos, A. P. Size dependence of the pressure-induced gamma to alpha structural phase transition in iron oxide nanocrystals. *Nanotechnology* **2005,** 16, 2813-2818.

10. Prilliman, S. G.; Clark, S. M.; Alivisatos, A. P.; Karvankova, P.; Vepřek, S. Strain and deformation in ultra-hard nanocomposites nc-TiN/a-BN under hydrostatic pressure. *Mat. Sci. and Engin. A* **2006**, *437*, 379-387.

11. Goldstein, A. N.; Echer, C. M.; Alivisatos, A. P. Melting in Semiconductor Nanocrystals. *Science* **1992**, *256*, 1425-1427.

12. Greenspan, J. E.; Campbell, S.; Shih, I. A multiple quantum well integrated with a selectively grown quaternary layer. *Semicond. Sci. Technol.* **2006**, *21*, 866-869.

13. Tolbert, S. H.; Alivisatos, A. P. Size dependence of the solid-solid phase transition in CdSe nanocrystals. *Z. Phys. D* **1993**, *26*, 56-58.

14. Tolbert, S. H.; Herhold, A. B.; Johnson, C. S.; Alivisatos, A. P. Comparison of Quantum Confinement Effects on the Electronic Absorption Spectra of Direct and Indirect Gap Semiconductor Nanocrystals. *Phys. Rev. Lett.* **1994**, *73*, 3266-3269.

15. Drickamer, H. G.; Edwards, A. L. Effect of Pressure on the Absorption Edges of Some III-V, II-VI, and I-VII Compounds. *Phys Rev.* **1961**, *122*, 1149-1157.

16. Onodera, A. High Pressure Transition in Cadmium Selenide. *Rev. of Phys Chem. Japan* **1969**, *39*, 65-77.

17. Yu, W. C.; Gielisse, P. J. High Pressure Polymorphism in CdS, CdSe, and CdTe. *Mat. Res. Bull.* **1971**, *6*, 621-638.

18. Colvin, V. L.; Schlamp, M. C.; Alivisatos, A. P. Light-emitting diodes made from cadmium selenide nanocrystals and a semiconducting polymer. *Nature* **1994**, *370*, 354-357.

19. Peng, X.; Schlamp, M. C.; Kadavanich, A. V.; Alivisatos, A. P. Epitaxial Growth of Highly Luminescent CdSe/CdS Core/Shell Nanocrystals with Photostability and Electronic Accessibility. *J. Am. Chem. Soc.* **1997**, *119*, 7019-7029.

20. Dabbousi, B. O.; Rodriguez-Viejo, J.; Mikulec, F. V.; Heine, J. R.; Mattoussi, H.; Ober, R.; Jensen, K. F.; Bawendi, M. G. (CdSe)ZnS Core-Shell Quantum Dots: Synthesis and Characterization of a Size Series of Highly Luminescent Nanocrystallites. *J. Phys. Chem. B* **1997**, *101*, 9463-9475.

21. Carbone, L.; Nobile, C.; De Giorgi, M.; Sala, F. D.; Morello, G.; Pompa, P.; Hytch, M.; Snoeck, E.; Fiore, A.; Franchini, I. R.; Nadasan, M.; Silvestre, A. F.; Chiodo, L.; Kudera, S.; Cingolani, R.; Krahne, R.; Manna, L. Synthesis and Micrometer-Scale Assembly of Colloidal CdSe/CdS Nanorods Prepared by a Seeded Growth Approach. *Nano Lett.* **2007**, *7*, 2942-2950.

22. Talapin, D. V.; Nelson, J. H.; Shevchenko, E. V.; Aloni, S.; Sadtler, B.; Alivisatos, A. P. Seeded Growth of Highly Luminescent CdSe/CdS Nanoheterostructures with Rod and Tetrapod Morphologies. *Nano Lett.* **2007**, *7*, 2951-2959.

23. Smith, A. M.; Mohs, A. M.; Nie, S. Tuning the optical and electronic properties of colloidal nanocrystals by lattice strain. *Nature Nanotech.* **2009**, *4*, 56-63.

24. Sadtler, B.; Demchenko, D. O.; Zheng, H.; Hughes, S. M.; Merkle, M. G.; Dahmen, U.; Wang, L.-W.; Alivisatos, A. P. Selective Facet Reactivity during Cation Exchange in Cadmium Sulfide Nanorods. *J. Am. Chem. Soc.* **2009,** 131, 5285-5293.

25. Deka, S.; Miszta, K.;. Dorfs, D.; Genovese, A.; Bertoni, G.; Manna, L. Octapod-Shaped Colloidal Nanocrystals of Cadmium Chalcogenides via "One-Pot" Cation Exchange and Seeded Growth. *Nano Lett.* **2010**, *10*, 3770-3776.

26. McWhan, D. B. The Pressure Variable in Materials Research. *Science* **1972**, *176*, 751-758.

27. Yu. P. Y. High pressure semiconductor physics: Looking toward the future on the shoulder of the past. *Phys. Status Solidi B* **2011**, *248*, 1077-1082.

28. Miletich, R.; Allan, D. R.; Kuhs, W. F. High-Pressure Single-Crystal Techniques. In *High-Temperature and High-Pressure Crystal Chemistry*; Hazen, R. M., Downs, R. T., Eds.; Reviews in Mineralogy and Geochemistry; Mineralogical Society of America: Washington D.C., 2000; Vol. 41, 445-520.

29. Eremets, M. *High Pressure Experimental Methods*. Oxford University Press: Oxford, 1996.

30. Hemley, R. J.; Bell, P. M.; Mao, H. K. Laser Techniques in High-Pressure Geophysics. *Science* **1987**, *237*, 605-6112.

31. Zhou, Y.; Campbell, A. J.; Heinz, D. L. Equations of State and Optical Properties of the High Pressure Phase of Zinc Sulfide. *J. Phys. Chem. Solids* **1991**, *52*, 821-825.

32. Wickham, J. N.; Herhold, A. B.; Alivisatos, A. P. Shape Change as an Indicator of Mechanism in the High-Pressure Structural Transformations of CdSe Nanocrystals. *Phys. Rev. Lett.* **2000**, *84*, 923-926.

33. Jacobs, K.; Zaziski, D.; Scher, E. C.; Herhold, A. B.; Alivisatos, A. P. Activation Volumes for Solid-Solid Transformations in Nanocrystals. *Science* **2001**, *293*, 1803-1806.

34. Zaziski, D.; Prilliman, S.; Scher, E. C.; Casula, M.; Wickham, J.; Clark, S. M.; Alivisatos, A. P. Critical Size for Fracture during Solid-Solid Phase Transformations. *Nano Lett.* **2004**, *4*, 943-946.

35. Herhold, A. B.; Chen, C.-C.; Johnson, C. S.; Tolbert, S. H.; Alivisatos, A. P. Structural Transformations and Metastability in Semiconductor Nanocrystals. *Phase Transitions* **1999**, *68*, 1-25.

36. Dalpian, G. M.; Chelikowsky, J. R. Self-Purification in Semiconductor Nanocrystals. *Phys. Rev. Lett.* **2006**, *96*, 226802.

37. Turnbull, D. Phase Changes. *Solid State Phys.* **1956**, *3*, 225-306.

38. Phillips, J. C.; Lucovsky, G. *Bonds and Bands in Semiconductors*, 2nd ed.; Momentum Press: New York, 2010.

39. Jayaraman, A. Diamond anvil cell and high-pressure physical investigations. *Rev. of Mod. Phys.* **1983**, *56*, 65-108.

40. Soignard, E.; McMillan, P. F. An Introduction to Diamond Anvil Cells and Loading Techniques. In *High-Pressure Crystallography;* Katrusiak, A., McMillan, P., Eds.; Proceedings of the NATO Advanced Study Institute; Springer: Netherlands, 2004, 81-100.

41. Letoullec, R.; Pinceaux, J. P.; Loubeyre, P. The membrane diamond anvil cell: A new device for generating continuous pressure and temperature variations. *High Pressure Research*, **1988**, *1*, 77-90.

42. Merrill, L.; Bassett, W. A. Miniature diamond anvil cell for single crystal x-ray diffraction studies. *Rev. Sci. Instrum.* **1974**, *45*, 290-294.

43. Merkel, S.; Yagi, T. X-ray transparent gasket for diamond anvil cell high pressure experiments. *Rev. Sci. Instrum.***2005**, *76*, 046109.

44. Syassen, K. Ruby under pressure. *High Pressure Research* **2008**, *28*, 75-126.

45. Carter, W. J.; Marsh, S. P.; Fritz, J. N.; McQueen, R. G. The Equation of State of Selected Materials for High Pressure References. In *Accurate Characterization of the High-Pressure Environment*; Proceedings of a Symposium held at the National Bureau of Standards; NBS: Washington, D. C. Special Publication, 1971; 326, 147.

46. Heinz, D. L.; Jeanloz, R. The equation of state of the gold calibration standard. *J. Appl. Phys.* **1984**, *55*, 885-893.

47. Kunz, M.; MacDowell, A. A.; Caldwell, W. A.; Cambie, D.; Celestre, R. S.; Domning, E. E.; Duarte, R. M.; Gleason, A. E.; Glossinger, J. M.; Kelez, N.; Plate, D. W.; Yu, T.; Zaug, J. M.; Padmore, H. A.; Jeanloz, R.; Alivisatos, A. P.; Clark, S. M. A beamline for high-pressure studies at the Advanced Light Source with a superconducting bend magnet as the source. *J. Synchrotron Rad.* **2005**, *12*, 650-658.

48. Forbes, J. W. *Shock Wave Compression of Condensed Matter: A Primer.* Springer: New York, 2012.

49. Zel'dovich, Y. B.; Raizer, Y. P. *Physics of Shock Waves and High-Temperature Hydrodynamic Phenomena.* Dover: Mineola, 2002.

50. Duvall, G. E.; Graham, R. A. Phase transitions under shock-wave loading. *Rev. Mod. Phys.* **1977**, *49*, 523-579.

51. Patterson, J.; Lagutchev, A.; Dlott, D. Shock Compression of Molecules with 1.5 Angstrom Resolution. In *Shock Compression of Condensed Matter-2003*. Furnish, M. D., Gupta, Y. M., Forbes, J.W., Eds.; American Institute of Physics, 2004; pp 1299-1302.

52. Lee, I.-Y. S.; Hill, J. R.; Dlott, D. D. Ultrafast microscopy of shock waves using a shock target array with an optical nanogauge. *J. Appl. Phys.* **1994**, *75*, 4975-4983.

53. Lee, I.-Y. S.; Hill, J. R.; Suzuki, H.; Dlott, D. D.; Baer, B. J.; Chronister, E. L. Molecular dynamics observed 60 ps behind a solid-state shock front. *J. Chem. Phys.* **1995**, *103*, 8313-8321.

54. Friedli, C.; Ashcroft, N. W. Aluminum under high pressure. I. Equation of state. *Phys. Rev. B* **1975**, *12*, 5552-5559.

55. McCusker, L. B.; Von Dreele, R. B.; Cox, D. E.; Louër, D.; Scardi, P. Rietveld refinement guidelines. *J. Appl. Cryst.* **1999**, *32*, 36-50.

56. Rietveld, H. M. A Profile Refinement Method for Nuclear and Magnetic Structures. *J. Appl. Cryst.* **1969**, *2*, 65-71.

57. Hill, R. J. Expanded Use of the Rietveld method in Studies of Phase Abundance in Multiphase Mixtures. *Powder Diffraction* **1991**, *6*, 74-77.

58. Lutterotti, L.; Matthies, S.; Wenk, H.-R. MAUD: a friendly Java program for material analysis using diffraction. *IUCr: Newsletter of the CPD* **1999**, *21*, 14-15.

59. Wojdyr, M. Fityk: a general-purpose peak fitting program. *J. Appl. Cryst.* **2010**, *43*, 1126-1128.

60. Grünwald, M.; Dellago, C. Nucleation and Growth in Structural Transformations of Nanocrystals. *Nano Lett.* **2009**, *9*, 2099-2102.

61. Morgan, B. J.; Madden, P. A. Simulations of the pressure-driven wurtzite to rock salt phase transition in nanocrystals. *Phys. Chem. Chem. Phys.* **2006**, *8*, 3304-3313.

62. Weinstein, B. A.; Hark, S. K.; Burnham, R. D.; Martin, R. M. Phase Transitions in AlAs/GaAs Superlattices under High Pressure. *Phys. Rev. Lett.* **1987**, *58*, 781-784.

63. Weinstein, B. A. Phase transitions in 2D semiconductor systems. *Semicond. Sci. Technol.* **1989**, *4*, 283-285.

64. Cui, L. J.; Venkateswaran, U. D.; Weinstein, B. A.; Chambers, F. A. Polymorphic stability of AlAs/GaAs superlattices at high pressure. *Phys. Rev. B* **1992**, *45*, 9248-9265.

65. Mathieu, H.; Allegre, J.; Chatt, A.; Lefebvre, P.; Faurie, J. P. Band offsets and lattice-mismatch effects in strained-layer CdTe/ZnTe superlattices. *Phys. Rev. B* **1988**, *38*, 7740-7748.

66. Dunstan, D. J.; Gil, B. Tellurium-based II-VI compound semiconductors and heterostructures under strain. *Semicond. Sci. Technol.* **1991**, *6*, 428-438.

67. Dunstan, D. J.; Prins, A. D.; Gil, B.; Faurie, J. P. Phase transitions in CdTe/ZnTe strained-layer superlattices. *Phys. Rev. B* **1991**, *44*, 4017-4020.

68. Fan, H. M.; Ni, Z. H.; Feng, Y. P.; Fan, X. F.; Kuo, J. L.; Shen, Z. X.; Zou, B. S. High pressure photoluminescence and Raman investigrations of CdSe/ZnS core/shell quantum dots. *Appl. Phys. Lett.* **2007**, *90*, 021921.

69. Li, Z.; Wang, L.; Liu, B.; Wang, J.; Liu, B.; Li, Q.;Zou, B.; Cui, T.; Meng, Y.; Mao, H.-K.; Liu, Z.; Liu, J. The structural transition behavior of CdSe/ZnS core/shell quantum dots under high pressure. *Phys. Status Solidi B* **2011**, *248*, 1149-1153.

70. Grünwald, M.; Lutker, K.; Alivisatos, A. P.; Rabani, E.; Geissler, P. L. Metastability in Pressure-Induced Structural Transformations of CdSe/ZnS Core/Shell Nanocrystals. *Nano Lett.* **2013,** *13*, 1367-1372.

71. Li, J. J.; Wang, Y. A.; Guo, W.; Keay, J. C.; Mishima, T. D.; Johnson, M. B.; Peng, X. Large-Scale Synthesis of Nearly Monodisperse CdSe/CdS Core/Shell Nanocrystals Using Air-Stable Reagents via Successive Ion Layer Adsorption and Reaction. *J. Amer. Chem. Soc.* **2003**, *125*, 12567-12575.

72. Xie, R.; Kolb, U.; Li, J.; Basché, T.; Mews, A. Synthesis and Characterization of Highly Luminescent CdSe-Core CdS/$Zn_{0.5}Cd_{0.5}$S/ZnS Multishell Nanocrystals. *J. Amer. Chem. Soc.* **2005**, *127*, 7480-7488.

73. Shen, H.; Wang, H.; Tang, Z.; Niu, J. Z.; Lou, S.; Du, Z.; Li, L. S. High quality synthesis of monodiserse zinc-blende CdSe and CdSe/ZnS nanocrystals with a phosphine-free method. *Cryst. Eng. Comm.* **2009**, *11*, 1733-1738.

74. Yu, W. W.; Qu, L.; Guo, W.; Peng, X. Experimental Determination of the Extinction Coefficient of CdTe, CdSe, and CdS Nanocrystals. *Chem. Mater.* **2003**, *15*, 2854-2860.

75. Hammersley, A. P. *FIT2D V10.3 Reference Manual V4.0*; ESRF Internal Report ESRF98HA01T; European Synchrotron Radiation Facility: Grenoble, August 1998.

76. Wojdyr, M. Fityk: a general-purpose peak fitting program. *J. Appl. Cryst.* **2010**, *43*, 1126-1128.

77. Akimoto, O.; Hasegawa, H. Strain-Induced Splitting and Polarization of Excitons Due to Exchange Interaction. *Phys. Rev. Lett.* **1968**, *20*, 916-918.

78. Langer, D. W.; Euwena, R. N.; Era, K.; Koda, T. Spin Exchange in Excitons, the Quasicubic Model and Deformation Potentials in II-VI Compounds. *Phys. Rev. B* **1970**, *2*, 4005-4022.

79. Qi, X.-L.; Zhang, S.-C. Topological insulators and superconductors. *Rev. of Mod. Phys.* **2011**, *83*, 1057-1110.

80. Hasan, M. Z.; Kane, C. L. Topological insulators. *Rev. of Mod. Phys.* **2010**, *82*, 3045-3067.

81. Moore, J. E. The birth of topological insulators. *Nature* **2010**, *464*, 194-198.

82. Koski, K. J.; Cha, J. J.; Reed, B. W.; Wessells, C. D.; Kong, D.; Cui, Y. High-Density Chemical Intercalation of Zero-Valent Copper into $Bi_2Se_3$ Nanoribbons. *J. Am. Chem. Soc.* **2012**, 134, 7584-7587.

83. Koski, K. J.; Wessells, C. D.; Redd, B. W.; Cha, J. J.; Kong, D.; Cui, Y. Chemical Intercalation of Zerovalent Metals into 2D Layered $Bi_2Se_3$ Nanoribbons. *J. Am. Chem. Soc.* **2012**, *134*, 13773-13779.

84. Jor, Y. S.; Williams, A. J.; Checkelsky, J. G.; Roushan, P.; Seo, J.; Xu, Q.; Zandbergen, H. W.; Yazdani, A.; Ong, N. P.; Cava, R. J. Superconductivity in $Cu_xBi_2Se_3$ and its Implications for Pairing in the Undoped Topological Insulator. *Phys. Rev. Lett.* **2010**, *104*, 057001.

85. Kriener, M.; Segawa, K.; Ren, Z.; Sasaki, S.; Ando, Y. Bulk Superconducting Phase with a Full Energy Gap in the Doped Topological Insulator $Cu_xBi_2Se_3$. *Phys. Rev. Lett.* **2011**, *106*, 127004.

86. Wray, L. A.; Xu, S.-Y.; Xia, Y.; Hor, Y. S.; Qian, D.; Fedorov, A. V.; Lin, H.; Bansil, A.; Cava, R. J.; Hasan, M. Z. Observation of topological order in a superconducting doped topological insulator. *Nature Phys.* **2010**, *6*, 855-859.

87. Vilaplana, R.; Santamaría-Pérez, D.; Gomis, O.; Manjón, F. J.; González, J.; Segura, A.; Muñoz, A.; Rodríguez-Hernández, E.; Marín-Borrás, V.; Muñoz-Sanjose, V.; Drasar, C.; Kucek, V.; Structural and vibrational study of $Bi_2Se_3$ under high pressure. *Phys. Rev. B* **2011**, *84*, 184110.

88. Hamlin, J. J.; Jeffries, J. R.; Butch, N. P.; Syers, P.; Zocco, D. A.; Weir, S. T.; Vohra, Y. K.; Paglione, J.; Maple, M. B. High pressure transport properties of the topological insulator $Bi_2Se_3$. *J. Phys.: Condens. Matter* **2012**, *24*, 035602.

89. Tolbert, S. H.; Alivisatos, A. P. High-Pressure Structural Transformations in Semiconudctor Nanocrystals. *Annu. Rev. Phys. Chem.* **1995**, *46*, 595-625.

90. Manjón, F. J.; Vilaplana, R.; Gomis, O.; Pérez-González, E.; Santamaría-Pérez, D.; Marín-Borrás, V.; Segura, A.; González, J.; Rodríguez-Hernández, P.; Muñoz, A.; Drasar, C.; Kucek, V.; Muñoz-Sanjosé, V. High-pressure studies of topological insulators $Bi_2Se_3$, $Bi_2Te_3$, and $Sb_2Te_3$. *Phys. Status Solidi B* **2013**, *250*, 669-676.

91. Segura, A.; Panchal, V.; Sánchez-Royo, J. F.; Marín-Borrás, V.; Muñoz-Sanjosé, V.; Rodríguez-Hernández, P.; Muñoz, A.; Pérez-González, E.; Manjón, F. J.; González, J. Trapping of three-dimensional electrons and transition to two-dimensional transport in the three-dimensional topological insulator $Bi_2Se_3$ under high pressure. *Phys. Rev. B* **2012**, *85*, 195139.

92. Nakayama, A.; Einaga, M.; Tanabe, Y.; Nakano, S.; Ishikawa, F.; Yamada, Y. Structural phase transition in $Bi_2Te_3$ under high pressure. *High Press. Res.* **2009**, *29*, 245-249.

93. Jacobsen, M. K.; Kumar, R. S.; Cornelius, A. L.; Sinogeiken, S. V.; Nicol, M. F. High Pressure X-ray Diffraction Studies of $Bi_{2-x}Sb_xTe_3$ (x=0,1,2). In *Shock Compression of Condensed Matter*, Proceedings of the American Institute of Physics, 2007; Elert, M, Furnish, M. D., Chau, R., Holmes, N., Nguyen, J. Eds.; CP955, 171-174.

94. Polian, A.; Gauthier, M.; Souza, S. M.; Trichês, D. M.; de Lima, J. C.; Grandi, T. A. Two-dimensional pressure-induced electronic topological transition in $Bi_2Te_3$. *Phys. Rev. B* **2011**, *83*, 113106.

95. Zhao, J.; Liu, H.; Ehm, L.; Dong, D.; Chen, Z.; Gu, G. High-pressure phase transitions, amorphization, and crystallization behaviors in $Bi_2Se_3$. *J. Phys: Condens. Matter* **2013**, *25*, 125602.

96. Kong, D.; Dang, W.; Cha, J. J.; Li, H.; Meister, S.; Peng, H.; Liu, Z.; Cui, Y. Few-Layer Nanoplates of $Bi_2Se_3$ and $Bi_2Te_3$ with Highly Tunable Chemical Potential. *Nano Lett.* **2010**, *10*, 2245-2250.

97. Angel, R. J. Equations of state. In *High-Temperature and High-Pressure Crystal Chemistry;* Hazen, R. M., Down, R. T., Eds.; Reviews in Mineralogy and Geochemistry; Mineralogical Society of America: Washington D. C., 2000; Vol. 41, 35-60.

98. Jmol: an open-source Java viewer for chemical structures in 3D. http://www.jmol.org/

99. Birch, F. Finite Elastic Strain of Cubic Crystals. *Phys. Rev.* **1947**, *71*, 809-824.

100. Wittenberg, J. S.; Merkle, M. G.; Alivisatos, A. P. Wurtzite to Rocksalt Phase Transformation of Cadmium Selenide Nanocrystals via Laser-Induced Shock Waves: Transition from Single to Multiple Nucleation. *Phys. Rev. Lett.* **2009**, *103*, 125701.

101. Grünwald, M.; Rabani, E.; Dellago, C. Mechanisms o the Wurtzite to Rocksalt Transformation in CdSe Nanocrystals. *Phys. Rev. Lett.* **2006**, *96*, 255701.

102. Grünwald, M.; Dellago, C. Ideal gas presure bath: a method for applying hydrostatic pressure in the computer simulation of nanoparticles. *Mol. Phys.* **2006**, *104*, 3709-3715.

103. Grünwald, M.; Dellago, C. Transition state analysis of solid-solid transformation in nanocrystals. *J. Chem. Phys.* **2009**, *131*, 164116.

104. Kim, H.; Hambir, S.; Dlott, D. Shock Compression of Organic Polymers and Proteins: Ultrafast Structural Relaxation Dynamics and Energy Landscapes. *J. Phys. Chem. B* **2000**, *104*, 4239-4252.

105. Nirmal, M.; Dabbousi, B. O.; Bawendi, M. G.; Macklin, J. J.; Trautman, J. K.; Harris, T. D.; Brus, L. E. Fluorescence intermittency in single cadmium selenide nanocrystals. *Nature* **1996**, *383*, 802-804.

106. Choi, C. L.; Lu, H.; Olson, A. C. K.; Jain, P. K.; Sivasankar, S.; Alivisatos, A. P. Spatially Indirect Emission in a Luminescent Nanocrystal Molecule. *Nano Lett.* **2011**, *11*, 2358-2362.

107. Zhou, X.; Andoy, N. M.; Liu, G.; Choudhary, E.; Han, K.-S.; Shen, H.; Chen, P. Quantitative super-resolution imaging uncovers reactivity patterns on single nanocrystals. *Nature Nanotech.* **2012**, *7*, 237-241.

108. Wang, L.; Ding, Y.; Patel, U.; Yang, W.; Xiao, Z.; Cai, Z.; Mao, W. L.; Mao, H.-K. Studying single nanocrystals under high pressure using an x-ray nanoprobe. *Rev. Sci. Instum.* **2011**, *82*, 043903.

109. Riedl, M. J. *Optical Design Fundamentals for Infrared Systems*, 2nd Ed.; SPIE Press: Bellingham, WA, 2001.

110. Riedl, M. J. *Optical Design: Applying the Fundamentals*; SPIE Press: Bellingham, WA, 2009.

111. Dadashev, A.; Pasternak, M. P.; Rozenberg, G. Kh.; Taylor, R. D. Applications of perforated diamond anvils for very high-pressure research. *Rev. Sci. Instrum.* **2001**, *72*, 2633-2637.

112. Soignard, E.; Benmore, C. J.; Yarger, J. L. A perforated diamond anvil cell for high-energy x-ray diffraction of liquids and amorphous solids at high pressure. *Rev. Sci. Instrum.* **2010**, *81*, 035110.

113. Takano, K. J.; Makatsuki, M. An optical high pressure cell with spherical sapphire anvils. *Rev. Sci. Instrum.* **1991**, *62*, 1576-1580.

114. Furuno, K.; Onodera, A.; Kume, S. Sapphire-Anvil Cell for High Pressure Research. *Japanese J. of Appl. Phys.* **1986**, *25*, L646-L647.

115. Vamivakas, A. N.; Younger, R. D.; Goldberg, B. B.; Swan, A. K.; Ünlü, M. S.; Behringer, E. R. A case study for optics: The solid immersion microscope. *Am. J. Phys.* **2008**, *76*, 758-768.

116. Baba, M.; Saski, T.; Yoshita, M.; Akiyama, H. Aberrations and allowances for errors in a hemisphere solid immersion lens for submicron-resolution photoluminescence microscopy. *J. Appl. Phys.* **1999**, *85*, 6923-6925.

117. Wu, Q.; Ghislain, L. P.; Elings, V. B. Imaging with Solid Immersion Lenses, Spatial Resolution, and Applications. *Proceedings of the IEEE* **2000**, *88*, 1491-1498.

118. Dobrovinskaya, E. R.; Lytvynov, L. A.; Pishchik, V. *Sapphire: Material, Manufacturing, Applications.* Springer, 2009.

119. Smith, W. J. *Modern Optical Engineering*, 4th Ed.; McGraw Hill: New York, 2008.

120. Chen, Y.; Vela, J.; Htoon, H.; Casson, J. L.; Werder, D. J.; Bussian, D. A.; Klimov, V. I.; Hollingworth, J. A. "Giant" Multishell CdSe Nanocrystal Quantum Dots with Suppressed Blinking. *J. Amer. Chem.* **2008**, *130*, 5026-5027.

121. Mahler, B.; Spinicelli, P.; Buil, S.; Quelin, X.; Hermier, J. P.; Dubertret, B. Towards non-blinking colloidal quantum dots. *Nature Mat.* **2008**, *7*, 659-664.

122. Schrier, J.; Lee, B.; Wang, L.-W. Mechanical and electronic-structure properties of compressed CdSe tetrapod nanocrystals. *J. Nanosci. Nanotechn.* **2008**, *8*, 1994-1998.

123. Choi, C. L.; Koski, K. J.; Sivasankar, S.; Alivisatos, A. P. Strain-Dependent Photoluminescence Behavior of CdSe/CdS Nanocrystals with Spherical, Linear, and Branched Topologies. *Nano Lett.* **2009**, *9*, 3544-3549.

124. Choi, C. L.; Koski, K. J.; Olson, A. C. K.; Alivisatos, A. P. Luminescent nanocrystal stress gauge. *Proc. Natl. Acad. Sci. USA* **2010**, *107*, 21306-21310.

125. DuFont, C. C.; Paszek, M. J.; Weaver, V. M. Balancing forces: architectural, control of mechanotransduction. *Nat. Rev. Mol. Cell Biol.* **2011**, *12*, 308-319.

126. Yu, H.; Mouw, J. K.; Weaver, V. M. Forcing form and function: biomechanical regulation of tumor evolution. *Trends in Cell Biol.* **2011**, *21*, 47-56.

127. Vogel, V.; Sheetz, M. P. Cell fate regulation by coupling mechanical cycles to biochemical signaling pathways. *Curr. Opin. Cell Biol.* **2009**, *21*, 38-46.

128. Butcher, D. T.; Alliston, T.; Weaver, V. M. A tense situation: forcing tumour progression. *Nat. Rev. Cancer* **2009**, *9*, 108-122.

129. Engler, A. J.; Griffin, M. A.; Sen, S.; Bönnemann, C. G.; Sweeney, H. L.; Discher, D. E. Myotubes differentiate optimally on substrates with tissue-like stiffness: pathological implications for soft or stiff microenvironments. *J. Cell Biol.* **2004**, *166*, 877-887.

130. Balaban, N. Q.; Schwarz, U. S.; Riveline, D.; Goichberg, P.; Tzur, G.; Sabanay, I.; Mahalu, D.; Safran, S.; Bershadsky, A.; Addadi, L.; Geiger, B. Force and focal adhesion assembly: a close relationship studied using elastic micropatterned substrates. *Nat. Cell Biol.* **2001**, *3*, 466-472.

131. Tan, J. L.; Tien, J.; Pirone, D. M.; Gray, D. S.; Bhadriraju, K.; Chen, C. S.; Cells lying on a bed of microneedles: An approach to isolate mechanical force. *Proc. Acad. Sci. USA* **2003**, *100*, 1484-1489.

132. Domke, J.; Parak, W. J.; George, M.; Gaub, H. E.; Radmacher, M. Mapping the mechanical pulse of single cardiomyocytes with the atomic force microscope. *Eur. Biophys. J.* **1999**, *28*, 179-186.

133. Pellegrino, T.; Manna, L.; Kudera, S.; Liedl, T.; Koktysh, D.; Rogach, A. L.; Keller, S.; Rädler, J.; Natile, F.; Parak, W. J. Hydrophobic Nanocrystals Coated with an Amphiphilic Polymer Shell: A General Route to Water Soluble Nanocrystals. *Nano Lett.* **2004**, *4*, 703-707.

134. Hermanson, G. T. *Bioconjugate Techniques*, 2nd Ed.; Academic Press: Amsterdam, 2008.

135. Claycomb, W. C.; Lanson, N. A.; Stallworth, B. S.; Egeland, D. B.; Delcarpio, J. B.; Bahinski, A.; Izzo, N. J. HL-1 cells: A cardiac muscle cell line that contracts and retains phenotypic characteristics of the adult cardiomyocyte. *Proc. Natl. Acad. Sci. USA* **1998**, *95*, 2979-2984.

136. Gupta, N. Biosensors Technologies: Acousto-Optic Tunable Filter-Based Hyperspectral and Polarization Imagers for Fluorescence and Spectroscopic Imaging. In *Methods in Molecular Biology: Biosensors and Biodetection*; Rasooly, A.; Herold, K. E., Eds.; Humana Press, 2009; Vol. 503, pp 293-305.

137. Wachman, E. S.; Niu, W.-h.; Farkas, D. L. AOTF Microscope for Imaging with Increased Speed and Spectral Versatility. *Biophysical Journal* **1997**, *73*, 1215-1222.

138. Bucher, E. G.; Carnahan, J. W. Characterization of an Acousto-optic Tunable Filter and Use in Visible Spectrophotometry. *Appl. Spect.* **1999**, *53*, 603-611.

139. Choi, C. L. Nanocrystal Molecules as Unique Systems for Structural, Mechanical, and

Optoelectronic Studies. Ph.D. Dissertation, University of California- Berkeley, Berkeley, CA, 2011.

140. *Collagen: Structure and Mechanics.* Fratzl, P., Ed.; Springer: New York, 2008.

141. Jawaid, A. M.; Cattopadhyay, S.; Wink, D. J.; Page, L. E.; Shee, P. T. Cluster-Seeded Synthesis of Doped CdSe:$Cu_4$ Quantum Dots. *ACS Nano* **2013**, *7*,l 3190-3197.

142. Mocatta, D.; Cohen, G.; Schattner, J.; MMillo, O.; Rabani, E.; Banin, U. Heavily Doped Semiconductor Nanocrystal Quantum Dots. *Science* **2011**, *332*, 77-81.

143. Sahu, A.; Kang, M. S.; Kompch, A.; Notthoff, C.; Wills, A. W.; Deng, D.; Winterer, M.; Frisbie, D.; Norris, D. J. Electronic Impurity Doping in CdSe Nanocrystals. *Nano Lett.* **2012**, *12*, 2587-2594.

144. Kwak, W. -C.; Kim, T. G.; Chae, W.-S.; Sung, Y.-M. Tuning the energy bandgap of CdSe nanocrystals via Mg doping. *Nanotechnology* **2007**, *18*, 205702.

145. Beaulac, R.; Archer, P. I.; Ochsenbein, S. T.; Gamelin, D. R. $Mn^{2+}$-Doped CdSe Quantum Dots: New Inorganic Materials for Spin-Electronics and Spin Photonics. *Adv. Funct. Mater.* **2008**, *118*, 3873-3891.

146. Santangelo, S. A.; Hinds, E. A.; Vlaskin, C. A.; Archer, P. I.; Gamelin, D. R. Bimodal Bond-Length Distributions in Cobalt-Doped CdSe, ZnSe, and $Cd_{1-x}Zn_xSe$ Quantum Dots. *J. Am. Chem. Soc.* **2007**, *129*, 3973-3978.

147. Dinega, D. P.; Bawendi, M. G. A Solution-Phase Chemical Approach to a New Crystal Structure of Cobalt. *Angew. Chem. Int. Ed.* **1999**, *38*, 1788-1791.

148. Puntes, V. F.; Krishnan, D. M.; Alivisatos, A. P. Colloidal Nanocrystal Shape and Size Control: The Case of Cobalt. *Science* **2001**, *291*, 2115-2117.

149. Puntes, V. F.; Krishnan, K.; Alivisatos, A. P. Synthesis of colloidal cobalt nanoparticles with controlled size and shapes. *Topics in Catalysis* **2002**, *19*, 145-148.

150. Puntes, V. F.; Zanchet, D.; Erdonmez, C. K.; Alivisatos, A. P. Synthesis of hcp-Co Nanodisks. *J. Amer. Chem. Soc.* **2002**, *124*, 12874-12880.

151. Polking, M. J.; Urban, J. J.; Milliron, D. J.; Zheng, H.; Chan, E.; Caldwell, M. A.; Raoux, S.; Kisielowski, C. F.; Ager, J. W.; Ramesh, R; Alivisatos, A. P. Size-Dependent Polar Ordering in Colloidal GeTe Nanocrystals**.** *Nano Lett,* **2011,** *11,* 1147-1152.

152. Rivest, J. B.; Fong, L. K.; Jain, P. K.; Toney, M. F.; Alivisatos, A. P. Size Dependence of a Temperature-Induced Solid-Solid Phase Transition in Copper(I) Sulfide. *J. Phys. Chem. Lett.* **2011**, *2*, 2402-2406.

153. Zheng, H.; Rivest, J. B.; Miller, T. A.; Sadtler, B.; Lindenberg, A.; Toney, M. F.; Wang, L.; Kisielowski, C.; Alivisatos, A. P. Observation of Transient Structural-Transformation Dynamics in a $Cu_2S$ Nanorod *Science* **2011**, *333*, 206-209.

154. Rousse, A.; Rischel, C.; Fourmaux, S.; Uschmann, I.; Sebban, S.; Grillon, G.; Balcou, P.; Förster, E.; Geindre, J. P.; Audebert, P.; Gauthier, J. C.; Hulin, D. Non-thermal melting in semiconductors measured at femtosecond resolution. *Nature* **2001**, *410*, 65-68.

155. Siders, C. W.; Cavalleri, A.; Sokolowski-Tinten, K.; Tóth, C.; Guo, T.; Kammler, M.; Horn von Hoegen, M.; Wilson, K. R.; von der Linde, D.; Barty, C. P. J. Detection of Nonthermal Melting by Ultrafast X-ray Diffraction. *Science* **1999**, *286*, 1340-1342.

156. Sokolowski-Tinten, K.; Bialkowski, J.; Boin, M.; Cavalleri, A.; von der Linde, D. Thermal and nonthermal melting of gallium arsenide after femtosecond laser excitation. *Phys. Rev. B* **1998**, *58*, 805-808.

157. Benisty, H.; Sotomayor-Torrès, C. M.; Weisbuch, C. Instrinsic mechanism for the poor luminescence properties of quantum-box systems, *Phys. Rev. B* **1991**, *44*, 10945-10948.

158. Heitz, R.; Born, H.; Guffarth, F.; Stier, O.; Schliqa, A.; Hoffmann, A.; Bumberg, D. Existence of a phonon bottleneck for excitons in quantum dots. *Phys. Rev. B* **2001**, *64*, 241305.